

CONNECTING MICROBURST PRECIPITATION TO ITS SCATTERING  
MECHANISM

by

Mykhaylo Sergeevich Shumko

A dissertation submitted in partial fulfillment  
of the requirements for the degree

of

Doctor of Philosophy

in

Physics

MONTANA STATE UNIVERSITY  
Bozeman, Montana

November 2019

©COPYRIGHT

by

Mykhaylo Sergeevich Shumko

2019

All Rights Reserved

## ACKNOWLEDGEMENTS

I would like acknowledge the countless engineers, technicians, and scientists who made the FIREBIRD, AC-6, and RBSP missions a success. This work was supported by Montana State University and by NASA Headquarters under the NASA Earth and Space Science Fellowship Program - Grant 80NSSC18K1204.

## TABLE OF CONTENTS

1. INTRODUCTION .....	1
Particle Populations and Their Interractions in the Magnetosphere .....	3
Populations in the Inner Magnetosphere .....	5
Plasmasphere.....	7
Ring Current .....	9
Radiation Belts.....	9
Charged Particle Motion in Electric and Magnetic Fields .....	13
Radiation Belt Particle Sources and Sinks .....	18
Adiabatic Heating .....	20
Wave Resonance Heating .....	20
Particle Losses .....	23
Microbursts .....	25
Scope of Reserach .....	31
2. EVIDENCE OF MICROBURSTS OBSERVED NEAR THE EQUATORIAL PLANE IN THE OUTER VAN ALLEN RADIATION BELT .....	33
Contribution of Authors and Co-Authors .....	33
Manuscript Information .....	35
Key Points .....	36
Abstract .....	36
Introduction .....	36
Spacecraft Instrumentation .....	39
Observations .....	40
Analysis .....	43
Microburst and Source PSD .....	43
Motion of resonant electrons in phase space .....	46
Comparing the microburst PSD to diffusion theory .....	49
Discussion and Conclusions .....	51
Acknowledgments .....	52
3. MICROBURST SCALE SIZE DERIVED FROM MULTIPLE BOUNCES OF A MICROBURST SIMULTANEOUSLY OBSERVED WITH THE FIREBIRD-II CUBESATS .....	54
Contribution of Authors and Co-Authors .....	54
Manuscript Information .....	55
Key Points .....	56

## TABLE OF CONTENTS – CONTINUED

Abstract .....	56
Introduction .....	57
Spacecraft and Observation .....	59
Analysis .....	62
Electron Bounce Period .....	63
Microburst Energy Spectra .....	65
Microburst Scale Sizes .....	65
Discussion and Conclusions .....	68
Acknowledgments .....	70
 4. MICROBURST SIZE DISTRIBUTION DERIVED WITH AEROCUBE-6.....	71
Contribution of Authors and Co-Authors .....	71
Manuscript Information .....	72
Key Points .....	73
Abstract .....	73
Introduction .....	74
Instrumentation .....	77
Methodology .....	78
Microburst Detection .....	78
Microburst Size Distribution in LEO and Magnetic Equator .....	80
Modeling the Distribution of Microburst Sizes .....	86
Monte Carlo and Analytic Models to Calculate $\bar{F}(s)$ .....	86
Methods for estimating optimal $\theta$ parameters .....	87
Estimating optimal parameters for various microburst size models .....	90
Discussion .....	92
Conclusions .....	97
Acknowledgments .....	98
 5. CONCLUSIONS AND FUTURE WORK .....	99
Future work .....	100
Future missions .....	102
 REFERENCES CITED .....	105

## TABLE OF CONTENTS – CONTINUED

APPENDICES .....	115
APPENDIX A : Wave properties observed by EMFISIS and pitch angle extent of microburst .....	116
APPENDIX B : Appendix B.....	120
APPENDIX C : Appendix C.....	128

## LIST OF TABLES

Table	Page
C.1 Range of log-normal model parameters consistent with the observed AC6 $\bar{F}(s)$ .....	132
C.2 Range of Weibull model parameters consistent with the observed AC6 $\bar{F}(s)$ .....	132

## LIST OF FIGURES

Figure	Page
1.1 A few macroscopic structures in the magnetosphere. The magnetosphere boundary with the solar wind is the magnetopause. The magnetotail consists of two lobes that contain Earth's magnetic flux with the plasma sheet separating the two lobes. The inner magnetosphere contains the plasmasphere, the ring current, and the radiation belts which are co-located. Figure from Baumjohann and Treumann (1997).....	4
1.2 The dipole coordinate system. The magnetic latitude of $\mathbf{r}$ is $\lambda$ . The radial distance to a magnetic field line in the equatorial plane is typically given by $L = r_{eq}/R_e$ . Figure from Baumjohann and Treumann (1997). .....	6
1.3 Equipotential lines and electric field arrows due to the superposition of the co-rotation and convection electric fields. Electrons in the shaded region execute closed orbits. Outside of the shaded regions the electrons are not trapped and will escape. The region separating the two regimes is called the Alfvén layer. Figure from Baumjohann and Treumann (1997).....	8

## LIST OF FIGURES – CONTINUED

Figure	Page
1.4 The DST index during the St. Patrick's Day 2015 storm. This storm was caused by a coronal mass ejection on March 15th, 2015. The storm phases are: initial phase, main phase, and recovery phase. The initial phase occurred when the Dst peaked at +50 nT on March 17th during which the ring current was eroded by the coronal mass ejection during the interval shown by the red bar shown at the bottom. Then the following rapid decrease to $\approx -200$ nT was during the main phase where many injections from the magnetotail enhanced the ring current, which reduced Earth's magnetic field strength at the ground, and is shown with the green bar. Lastly, the recovery phase lasted from March 18th to approximately March 29th during which the ring current particles were lost and the ring current returned to its equilibrium state. The recovery phase is shown with the blue bar. ....	10
1.5 The two radiation belts with a the locations of various satellites and orbits. Figure from (Horne et al., 2013). ....	11
1.6 The dynamics of the outer radiation belt in 1997 from the POLAR satellite. Top panel shows the 1.2-2.4 MeV electron flux as a function of L and 1997 day of year. The middle panel shows the DST index, and bottom panel shows the solar wind velocity. Figure from (Reeves et al., 2003). ....	12
1.7 The three periodic motions of charged particles in Earth's dipole magnetic field. These motions are: gyration about the magnetic field line, bounce motion between the magnetic poles, and azimuthal drift around the Earth. Figure from (Baumjohann and Treumann, 1997). ....	14

## LIST OF FIGURES – CONTINUED

Figure	Page
1.8 Charged particle motion in a uniform magnetic field $\vec{B}$ . Panel (A) shows the geometry defining the pitch angle, $\alpha$ . Panel (B) and (C) show two helical electron trajectories with dashed lines assuming a large and small $\alpha$ (corresponding to a small and large parallel velocity $v_{  }$ ), respectively. ....	17
1.9 Contours of constant gyration, bounce, and drift frequencies for electrons and protons in a dipole field. Figure from Schulz and Lanzerotti (1974). ....	19
1.10 The trajectories of an electron and a right-hand circularly polarized wave during a cyclotron resonance. The electron's $v_{  }$ and the wave's $k_{  }$ are in opposite directions such that the wave's frequency is Doppler shifted to a integer multiple of the electron cyclotron frequency. Figure from (Tsurutani and Lakhina, 1997). ....	22
1.11 Various wave modes in the magnetosphere. Ultra low frequency waves occur through the magnetosphere. Chorus waves are typically observed in the 0-12 midnight-dawn region. EMIC waves are typically observed in the dusk MLT sector. Hiss waves are observed inside the plasmasphere. Figure from Millan and Thorne (2007). ....	24
1.12 An example train of microbursts observed by FIREBIRD-II unit 4 on February 2nd, 2015. The colored curves show the differential energy channel count rates in five channels from $\approx 200$ keV to 1 MeV and a sixth integral energy channel with a 1 MeV threshold. The x-axis labels show auxiliary information such as time of observation and the spacecraft position in L, MLT, latitude and longitude coordinates.....	27

## LIST OF FIGURES – CONTINUED

Figure	Page
1.13 Distribution of $> 1$ MeV microburst occurrence rates as a function of L and MLT. The three panels show the microburst occurrence rate dependence on geomagnetic activity, parameterized by the auroral electrojet (AE) index for (a) $AE < 100$ nT, (b) $100 < AE < 300$ nT and (c) $AE > 300$ nT. Figure from Douma et al. (2017). .....	28
1.14 Three snapshots of a temporal microburst observed simultaneously by a pair of polar-orbiting spacecraft. The spacecraft are identified by labels "A" and "B" and are traveling upwards on the blue dashed orbital track. At $T_1$ the spacecraft are traveling upwards and no microburst is observed. Then at $T_2$ both spacecraft simultaneously observe a microburst shown by the red circle and the microburst size must be greater than the spacecraft separation. In the last snapshot, $T_3$ , the microburst has precipitated and no longer observed by the spacecraft.....	31

## LIST OF FIGURES – CONTINUED

Figure	Page
2.1 Electron and wave conditions from the MagEIS-A and EMFISIS WFR sensors for the microburst time interval. Panels (a), (b), and (c) are from RBSP-A with its position information annotated in panel (a). Panels (d), (e), and (f) are from RBSP-B with its position information annotated in panel (d). Panel (a) is the MagEIS-A high rate timeseries. Panels (b) and (e) show the evolution of the MagEIS-A $J$ as a function of $\alpha_L$ from the $\sim 40$ to $\sim 60$ keV channel. Every 10th point is shown in panel (b). The solid black line in panels (a) and (b) mark the end of the time period used for the PSD fit extrapolation analysis explained in section 3. The dashed black lines in panels (a) and (b) show the time interval used for the observed microburst PSD. Panels (c) and (f) show the EMFISIS WFR spectra, with the available burst data superposed. The red, green, and cyan traces are equatorial $f_{ce0}$ , $f_{ce0}/2$ , and $f_{ce0}/10$ , respectively. ....	42
2.2 Panel (a) shows the MagEIS-A high rate timeseries. Panel (b) shows the RBSPICE EBR count rate timeseries for $> 19$ keV electrons. The microbursts were observed between 11:17:10 - 11:17:12 UT and are indicated with the vertical black arrows in panels (a) and (b) for MagEIS-A times. Panel (c) shows the RBSPICE EBR (family of relatively sparse sampled curves) and MagEIS-A $J$ from the 29-41 keV energy channel (single curve) as a function of $\alpha_L$ . The vertical dashed lines show the time interval for the PSD analysis.....	44

## LIST OF FIGURES – CONTINUED

Figure	Page
2.3 The colored annulus represents $f(p_\perp, p_\parallel)$ in normalized momentum space, parallel and perpendicular to the background magnetic field. The microburst $f(p_\perp, p_\parallel)$ is highlighted with the white circle. The columns show different powers of the sine extrapolation, and rows show the different magnetic latitudes of the scattering. The white dotted traces represent the boundary between the data and extrapolation. The green, red, and white solid traces are the resonance curves for $\omega = 0.2\Omega_{ce}$ , $0.4\Omega_{ce}$ , $0.6\Omega_{ce}$ , respectively. The cyan dashed traces are the diffusion curves for a $\omega = 0.4\Omega_{ce}$ wave (waves of other frequency have similar diffusion curves). The magnetic latitude of the scattering, the ratio of the plasma to the cyclotron frequency, and the power of the sine extrapolation is annotated in each panel. For the resonance and diffusion curves, the density model assumed a $n_L = 1 e^-/cm^3$ and $\psi = -1$ .....	47
3.1 HiRes data of the microburst observed at February 2nd, 2015 at 06:12:53 UT, smoothed with a 150 ms rolling average. The subsequent bounces showed some energy dispersion. As discussed in Appendix B, a time correction of -2.28 s was applied to FU3. While the flux from five energy channels is shown, only channels with reasonable counting statistics were used for the spatial scale analysis. Vertical colored bars show the $\sqrt{N}$ error every 10th data point and vertical black bars are lined up with the peaks in the 220-283 keV energy channel to help identify dispersion.	61

## LIST OF FIGURES – CONTINUED

Figure	Page
3.2 Observed and theoretical $t_b$ for electrons of energies from 200 to 770 keV. The solid black line is $t_b$ in a dipole magnetic field, derived in Schulz and Lanzerotti (1974). The red dotted and cyan dashed lines are the $t_b$ derived using the T89, and T04 magnetic field models with IRBEM-Lib. Lastly, the blue dot-dash curve is the $t_b$ derived using the Olson & Pfitzer Quiet model. The green and purple rectangles represent the observed $t_b$ for FU3 and FU4 using a Gaussian fit, respectively. The blue rectangles represent the observed $t_b$ calculated with the minima between the bounces. The width of the boxes represent the width of those energy channels, and the height represents the uncertainty from the fit.....	64
3.3 The topology of the FIREBIRD-II orbit and the multiple bounces of the microburst projected onto latitude and longitude with axis scaled to equal distance. Attributes relating to FU3 shown in red dashed lines, and FU4 with blue solid lines. The spacecraft path is shown with the diagonal lines, starting at the upper right corner. The labels P1-4 for FU4 and P1-5 for FU3 indicate where the spacecraft were when the $N^{th}$ peak was seen in the lowest energy channel in the HiRes data. The stars with the accompanying energy labels represent the locations of the electrons with that energy that started at time of P1, and were seen at the last peak on each spacecraft. The rectangles represent the lower bound of the microburst scale size, assuming that the majority of the electrons were in the upper boundary of energy channel 4.....	67
4.1 AC6 mission properties for (a) spacecraft separation and (b) number of simultaneous quality 10 Hz samples as a function of L and MLT.....	78

## LIST OF FIGURES – CONTINUED

Figure	Page
4.2 Examples of $> 35$ keV microbursts observed simultaneously by AC6-A in red and AC6-B in blue. Panels (a), (c), (e), and (g) show the temporally-aligned time series when AC6 were separated by $s = 5, 16, 37$ , and $69$ km, respectively. The corresponding panels (b), (d), (f), and (h) show the spatially-aligned time series which is made by shifting the AC6-A time series in the above panels by the in-track lag (annotated with $dt$ ) that show any spatially correlated structures. The clear temporal correlation and lack of spatial correlation demonstrates that these events are microbursts. ....	81
4.3 Microburst size distribution in low Earth orbit. Panel (a) shows the percent of microbursts observed above that separation after normalizing for the uneven AC6 sampling in separation. Panel (b) shows the microburst probability density (size histogram) as a function of separation. Lastly, panel (c) shows the normalization, i.e. number of simultaneous samples AC6 observed as a function of separation. The colored lines show the distributions binned by $L$ , and the thick black curve for the entire radiation belt ( $4 < L < 8$ ). The gray shading around the black curve shows the uncertainty due to counting statistics. ....	84
4.4 Microburst size distribution mapped to the magnetic equator in the same format as Fig. 4.3. ....	85

## LIST OF FIGURES – CONTINUED

Figure	Page
4.5 Panels A-C show the varying geometries of the analytic model. The two spacecraft are shown as black dots. The enclosing black circle around each spacecraft bounds the area where a microburst will be observed by one or both AC6 units if the microburst's center lies inside the circle. Panel (A) shows the case where microburst diameter is smaller than the AC6 separation and all microbursts will be observed by either unit A or B and never simultaneously. Panel (B) shows the intermediate case where the microburst diameter is comparable to the AC6 separation and some fraction of microbursts will be observed simultaneously. The fraction of the microbursts simultaneously observed is proportional to the circle intersection area $A(r, s)$ and is shown with grey shading. Panel (C) shows the case where the microburst diameter is much larger than the spacecraft separation and nearly all microbursts will be observed by both spacecraft. Lastly panel (D) shows $\bar{F}(s)$ from the AC6 data with a solid black line, and modeled MC and analytic $\bar{F}(s)$ curves for a single-sized microburst distribution with $d = 40$ km.....	88
4.6 Range of plausible microburst sizes assuming all microbursts are one fixed size. Panel (a) shows the posterior probability density function of microburst diameters in black. The red, green, and blue vertical lines at 38, 73, and 129 km represent the 2.5, 50, and 97.5 posterior percentiles, respectively. A uniform prior between 0 and 200 km was assumed for this MCMC run and is shown in cyan. Panel (b) shows the percent of microbursts observed above an AC6 separation for $4 < L < 8$ in black. The 2.5, 50 and 97.5 size percentiles were estimated from the posterior and plotted in red, green, and blue curves, respectively. ....	93

## LIST OF FIGURES – CONTINUED

Figure	Page
4.7 Plausible microburst percent curves assuming microburst size distribution is bimodal consisting of two sizes $d_0$ and $d_1$ with a mixing term that quantifies the relative occurrence of the $d_0$ to $d_1$ microburst populations. Panel (a) shows the posterior distribution for the microburst population mixing term, $a$ with a median value of 0.02. The $a$ prior was uniform between 0 and 0.2. Panel (b) shows the posterior distribution for $d_0$ , the larger microburst population estimated with a uniform prior between 50 and 200 km and the posterior median diameter of 122 km. Panel (c) shows the posterior distribution for $d_1$ , the smaller microburst population, estimated using a uniform prior between 0 and 50 km with a median diameter of 28 km. Panel (d) is similar to Fig. 4.6b and shows the AC6 microburst fraction for $4 < L < 8$ in black. A set of 1000 random parameter triples ( $a$ , $d_0$ , and $d_1$ ) were drawn from the posterior and used to generate a family of $\bar{F}(s)$ curves. At each $s$ the range of consistent $\bar{F}(s)$ were quantified by the 2.5, 50 and 97.5 percentiles and shown with the red, green, and blue curves, respectively. ....	94
A.1 Panel (A) shows the magnetic power spectral density as a function of frequency and time from the EMFISIS WFR instrument on board RBSP-A. The “hiss-like” wave used for the resonant diffusion analysis was observed starting at 11:17:03 UT. In the same format as panel (A), panel (B) shows the polar angle of the wave vector for this time period. The wave of interest had a normal wave vector, $\theta_k < 30^\circ$ . Since the results in panel (B) are valid only for high planarity, panel (C) shows planarity in the same format as panels (A) and (B). The wave of interest was found to have a planarity of $> 0.8$ . Lastly, panel (D) shows the available burst mode data. ....	118

## LIST OF FIGURES – CONTINUED

Figure	Page
A.2 Ratio of the RBSPICE EBR at microburst times indicated with the black vertical arrows in Fig. 2, to the EBR at the same pitch angles one spin prior (quiet time). The microburst flux was enhanced by 10-80% across $100^\circ < \alpha_L < 160^\circ$ PA, and appear to be peaked closer to $\alpha_L = 90^\circ$ .....	119
B.1 Cross-correlation time lag analysis applied to a train of microbursts. Panel (a) and (b) show the count rate from the lowest energy channel. Panel (c) shows the cross-correlation coefficient as a function of time lag. Panel (d) shows the shifted timeseries. Clock difference was 2.23 s .....	122
B.2 Same analysis as Fig. B.1 on a different time period. Clock difference was 2.21 s.....	123
B.3 Same analysis as Fig. B.1 on a different time period. Clock difference was 2.25 s.....	124
B.4 Same analysis as Fig. B.1 on a different time period. Clock difference was 2.27 s.....	125
B.5 Same cross-correlation time lag analysis applied to stationary spatial structures. The cross-correlation lag between these events is a sum of the clock difference and time lag due to the spacecraft separation. The lag derived at this time was 4.95 s .....	126
B.6 Same analysis as Fig. B.5 applied to a different stationary spatial feature. The lag derived at this time was 5.01 s .....	127

## NOMENCLATURE

$L$	L-Shell
$MLT$	magnetic local time
$\lambda$	magnetic latitude
$\alpha$	pitch angle
$\alpha_L$	local pitch angle at the spacecraft
$\alpha_{eq}$	pitch angle maped to the magnetic equator
$c$	speed of light
$R_E$	Earth's radius
$J$	flux
$f$	phase space density
$E$	energy
$E_0$	exponential e-folding energy
$p$	momentum
$\vec{E}$	electric field
$\vec{B}$	magnetic field
$B_w$	wave amplitude
$v$	velocity
$\Omega_e$	electron gyrofrequency
$\omega_{pe}$	plasma frequency
$k$	wave vector
$D_{xx}$	diffusion coefficient
$s$	spacecraft separation
$t_b$	electron bounce period

## INTRODUCTION

Above Earth's atmosphere are the Van Allen radiation belts, a toroidally-shaped pair of belts that consist of a complex and dynamic plasma environment. The inner radiation belt is stable, consists of mostly energetic protons, and is located within 2 Earth radii (measured near the equator) above Earth's surface. The outer radiation belt, on the other hand, consists of mostly energetic electrons, is dynamic on hour time scales, and is typically found between three and eight Earth radii above Earth's surface. These belts pose a threat to space exploration due to their adverse effects on our bodies and electrical components. A few effects include: a high radiation dose for manned missions, degradation of silicon that causes transistor malfunction, computer memory corruption due to bit flips, etc. With these effects in mind, it is no surprise that the radiation belts have been extensively studied since their discovery in the 1960s.

The radiation belt particles, mostly consisting of electrons and protons, are at times unstable to wave growth and generate electric and magnetic waves. These waves can then accelerate and scatter radiation belt particles with a variety of wave-particle mechanisms. These wave-particle interactions are believed to be responsible for scattering electron microbursts—a short and intense increase of precipitating electrons into Earth's atmosphere—that are capable of destroying ozone molecules and rapidly deplete the outer belt's electrons.

Electron microbursts, henceforth referred to as microbursts, are typically observed by low Earth orbiting spacecraft, sounding rockets, and high altitude balloons as a sub-second impulse of electrons. Some of the most intense microbursts

have electron fluxes that are a factor of 10 to 100 above the background (for example see Fig. 7 in Blake et al. (1996)). Since they were first reported by Anderson and Milton (1964), the intense transient nature of microbursts have compelled researchers to pursue an understanding of their properties, their effects on the environment, and the physical mechanism(s) that create microbursts. Microbursts are widely believed to be created by wave-particle scattering between a plasma wave called whistler mode chorus and outer radiation belt electrons, although many details regarding the scattering mechanism are unconstrained or unknown. The goal of this dissertation is to expand our knowledge of the wave-particle scattering mechanism that causes electron microbursts.

This chapter serves as an introduction to the fundamental physical concepts that are essential to understand wave-particle interactions in Earth's magnetosphere. We will review the main structures in the magnetosphere, the motion of charged particles in electric and magnetic fields, how particles are accelerated and lost in the magnetosphere, and asses the current state of our understanding of microbursts.

Then the rest of this dissertation expands our knowledge of microbursts. In Chapter 2 (chapter numbers will be filled in the full dissertation) we will investigate and model the scattering mechanism responsible for microbursts observed inside the outer radiation belt, near the magnetic equator. Then in Chapters 3 and 4 we will investigate the microburst scattering mechanism indirectly by estimating the microburst footprint size in low Earth orbit and the magnetic equator (near where microburst electrons are believed to be scattered) and compare it to sizes of chorus waves estimated in prior literature.

## Particle Populations and Their Interractions in the Magnetosphere

To set the scene, we will briefly tour the various populations in the magnetosphere that are most relevant to this dissertation, and are illustrated in Fig. 1.1.

The sun and its solar wind are ultimately the source of energy input into the magnetosphere. The solar wind at Earth's orbit is a plasma traveling at supersonic speeds with an embedded interplanetary magnetic field (IMF). When the solar wind encounters Earth's magnetic field, the plasma can not easily penetrate into the magnetosphere. The plasma can not easily penetrate into the magnetosphere because it is frozen-in on the magnetic field lines because plasma has a nearly infinite conductivity. Thus the plasma and its magnetic field drapes around the magnetosphere, forming a cavity in the solar wind that qualitatively has a shape similar to in Fig. 1.1. The solar wind is supersonic at 1 AU so a bow shock exists upstream of the magnetosphere which compresses and heats the solar wind. Downstream of the bow shock, the solar wind plasma flows around the magnetosphere inside the magnetosheath. The magnetopause is the surface where the solar wind ram and Earth's magnetic pressures balance. To first order, the magnetopause can be thought of as a boundary between the solar wind and Earth's magnetosphere. The shocked plasma then flows past the Earth where it shapes the magnetotail. In the magnetotail, the magnetopause exists where the solar wind magnetic pressure balances Earth's magnetic field pressure in the lobes. The magnetotail extends on the order of 100  $R_E$  downstream of Earth, and the tailward stretching of magnetic field lines creates a region where Earth's earthward and anti-earthward magnetic fields are in proximity. In this region, the curl of  $\vec{B}$  is non-zero, thus by Ampere's law there must be a current (called the plasma sheet) near the magnetic equator (e.g. Eastwood et al., 2015).

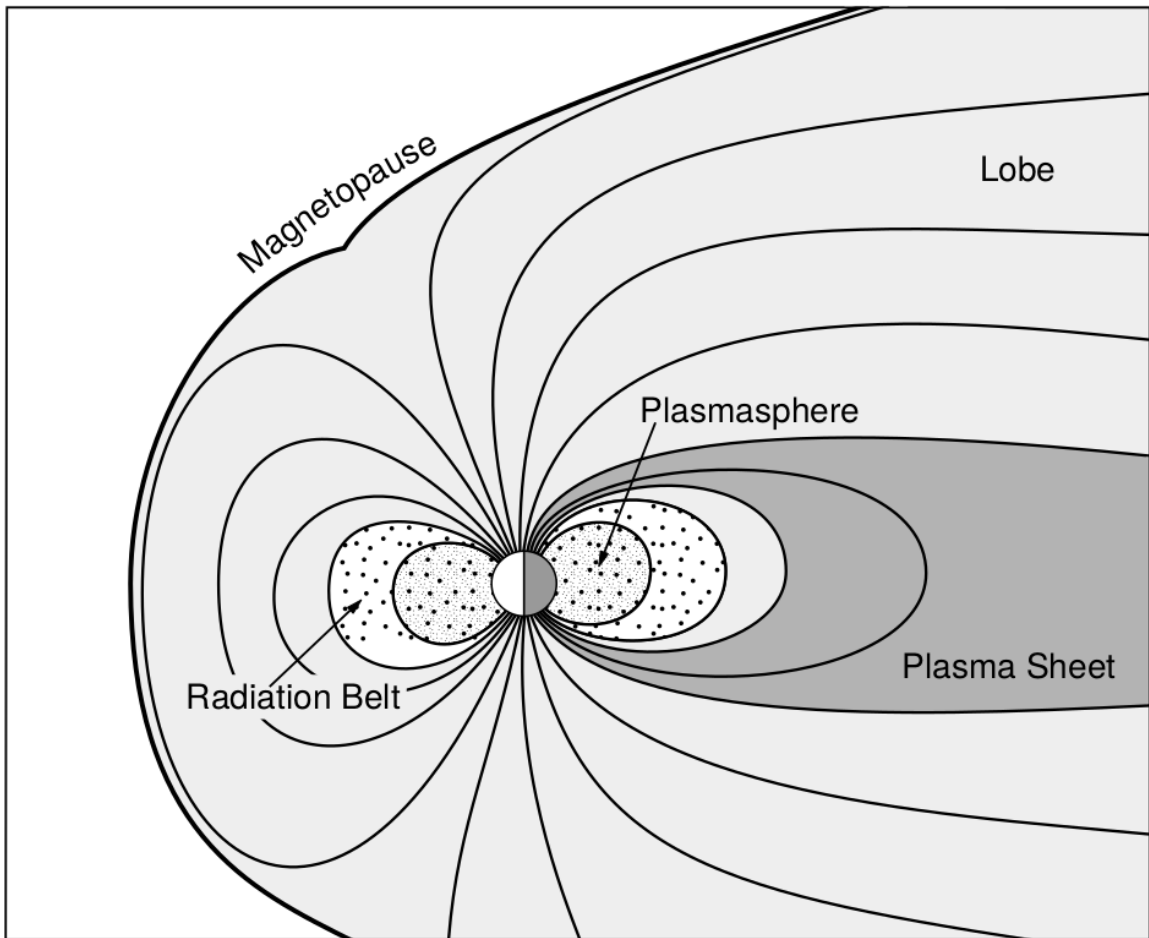


Figure 1.1: A few macroscopic structures in the magnetosphere. The magnetosphere boundary with the solar wind is the magnetopause. The magnetotail consists of two lobes that contain Earth's magnetic flux with the plasma sheet separating the two lobes. The inner magnetosphere contains the plasmasphere, the ring current, and the radiation belts which are co-located. Figure from Baumjohann and Treumann (1997).

### Populations in the Inner Magnetosphere

Closer to Earth, where the magnetic field is largely dipolar, are three plasma populations that comprise the inner magnetosphere: the plasmasphere, the ring current, and the radiation belts which are shown in Fig. 1.1. Before we describe these three particle populations in detail, we will introduce the coordinate system that most naturally describes the inner magnetosphere environment, and the electric fields that mostly effect low energy particles.

This coordinate system is shown in Fig. 1.2 and it naturally describes particles in a dipole magnetic field geometry. In this coordinate system the “radial” coordinate is the L shell. The  $L$ -shell ( $L$ ) is the distance from the Earth’s center to the location where a particular magnetic field line crosses the magnetic equator, in units of Earth radii,  $R_e = 6,371$  km. The azimuthal coordinate is the magnetic local time (MLT). For an observer above Earth’s north pole looking down, MLT is defined to be 0 (midnight) in the anti-sunward direction and increases in the counter-clockwise direction with 6 at dawn, 12 at noon (sunward direction), and 18 at dusk. The final coordinate is the magnetic latitude,  $\lambda$ , which is analogous to the latitude coordinate in the spherical coordinate system and is defined to be 0 at the magnetic equator. This coordinate system naturally describes the inner magnetosphere populations described below.

Low energy particle dynamics in the inner magnetosphere are driven by the co-rotation and the dawn-dusk (pointing from approximately 6 to 18 MLT) electric fields. The co-rotation electric field arises from Earth’s rotation. Earth’s magnetic field and the particles frozen on it rotate with the Earth so in the magnetosphere (non-rotating) reference frame the particles appear to  $\vec{E} \times \vec{B}$  drift (which will be described in the next section) with Earth’s rotation. The co-rotation  $\vec{E}$  points towards Earth. The convection electric field points from dawn to dusk, and is due to the Earthward

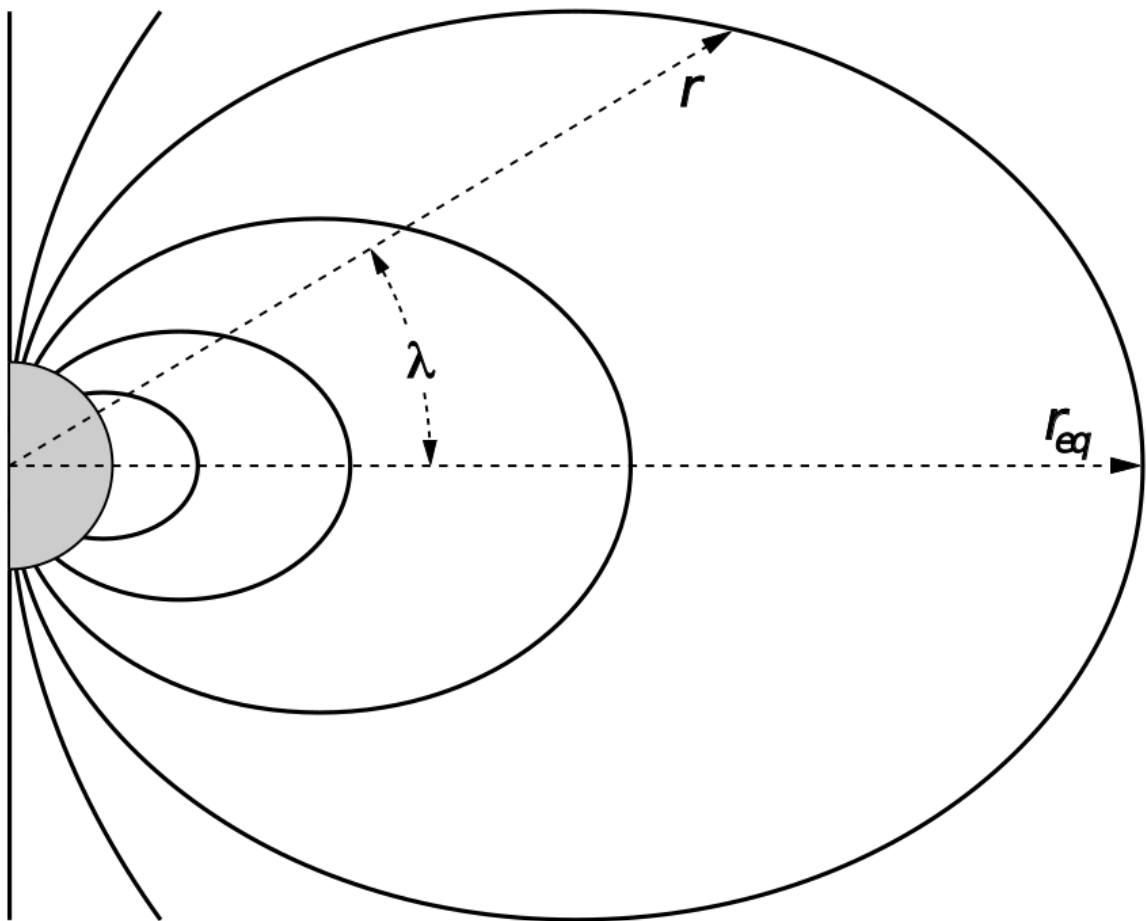


Figure 1.2: The dipole coordinate system. The magnetic latitude of  $\mathbf{r}$  is  $\lambda$ . The radial distance to a magnetic field line in the equatorial plane is typically given by  $L = r_{eq}/R_e$ . Figure from Baumjohann and Treumann (1997).

transport of particles from the magnetotail. The superposition of the co-rotation and convection electric fields is a potential field shown in Fig. 1.3. The shaded area in Fig. 1.3 shows where low energy electrons execute closed orbits around Earth (i.e. particles are trapped), and outside this region the electrons are not trapped. The dynamic topology of the shaded region in Fig. 1.3 is controlled by only the convection electric field which is dependent on the solar wind speed and the IMF. The lowest energy particles that orbit along equipotential lines in the shaded region in Fig. 1.3 make up the plasmasphere.

Plasmasphere The plasmasphere is a relatively dense ( $n_e \sim 10^3/\text{cm}^3$ ) and cool ( $\sim \text{eV}$ ) plasma. The plasmasphere typically extends to  $L \sim 4$  and the spatial extent is highly dependent on the solar wind and magnetospheric conditions. The source of the plasmasphere is the ionosphere, a layer in Earth's upper atmosphere that contains a high concentration of electrons and ions. The main mechanisms that ionize the ionosphere are ultraviolet light from the sun and particle precipitation. The ultraviolet ionization by sunlight is strongly dependent on the time of day and latitude, while particle precipitation is highly dependent on magnetospheric conditions and mostly occurs at high latitudes.

The outer boundary of the plasmasphere is called the plasmapause which is typically identified by a steep radial gradient in plasma density from  $\sim 10^3/\text{cm}^3$  to  $\sim 1/\text{cm}^3$ . It is important to know the location of the plasmapause since the plasma density strongly controls the efficiency of particle scattering by waves. For example, electron scattering by chorus waves is more efficient when the ratio of the plasma and gyro frequency is low which is typically found in low plasma density regions outside of the plasmapause (e.g. Horne et al., 2003a, 2005; O'Brien and Moldwin, 2003).

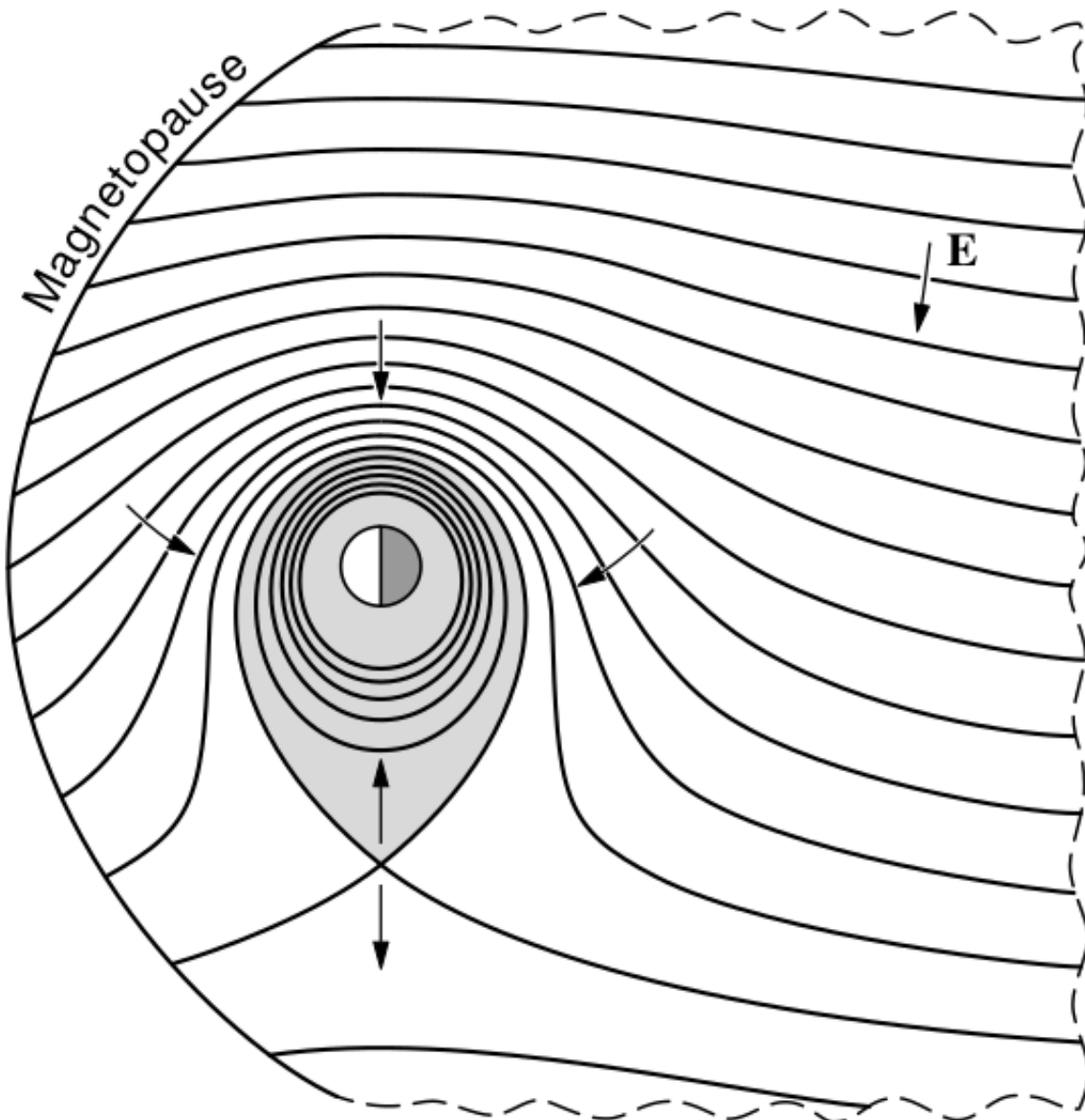


Figure 1.3: Equipotential lines and electric field arrows due to the superposition of the co-rotation and convection electric fields. Electrons in the shaded region execute closed orbits. Outside of the shaded regions the electrons are not trapped and will escape. The region separating the two regimes is called the Alfvén layer. Figure from Baumjohann and Treumann (1997).

Ring Current A higher energy population is the ring current. This population consists of protons and electrons between tens and a few hundred keV that drift around the Earth. The orbits of higher energy particles are not as affected by the convection and co-rotation electric field, instead they drift around the Earth due to gradient and curvature drifts which will be described in the following section. Since the direction of the drift is dependent on charge, protons drift west around the Earth and electrons drift East. This effect creates a current around the Earth.

The ring current generates a magnetic field which decreases the magnetic field strength at the surface of the Earth and increases it outside of the ring current. The decrease of Earth's magnetic field strength is readily observed by a system of ground-based magnetometers and is merged into a Disturbance Storm Time (DST) index to quantify the global reduction in the magnetic field. An example of a DST index time series from the 2015 St. Patrick's Day storm, driven by a coronal mass ejection (CME), is shown in Fig. 1.4. At the start of a storm, DST sometimes increases in response to the compression of the magnetopause by a shock wave (termed the initial phase or sudden storm commencement) and is shown by the red horizontal bar in Fig. 1.4. During the main phase of the storm the ring current population is rapidly built up and DST rapidly decreases which is shown by the green bar in Fig. 1.4. After the storm is over, the ring current slowly recovers to pre-storm conditions during the recovery phase shown by the blue bar in Fig. 1.4. In the recovery phase, the ring current gradually decays due to particles losses into the atmosphere, or transport through the magnetopause via mechanisms described later in this chapter. The DST index, along with other geomagnetic indices, are used by the space physics community to quantify the global state of the magnetosphere.

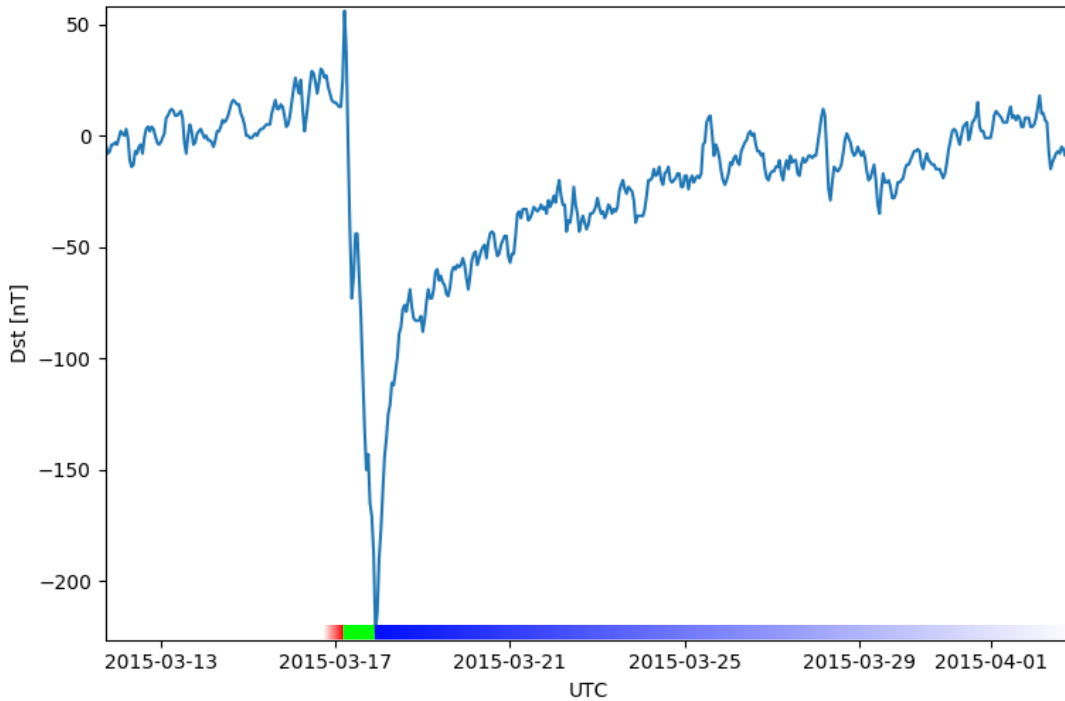


Figure 1.4: The DST index during the St. Patrick's Day 2015 storm. This storm was caused by a coronal mass ejection on March 15th, 2015. The storm phases are: initial phase, main phase, and recovery phase. The initial phase occurred when the Dst peaked at  $+50$  nT on March 17th during which the ring current was eroded by the coronal mass ejection during the interval shown by the red bar shown at the bottom. Then the following rapid decrease to  $\approx -200$  nT was during the main phase where many injections from the magnetotail enhanced the ring current, which reduced Earth's magnetic field strength at the ground, and is shown with the green bar. Lastly, the recovery phase lasted from March 18th to approximately March 29th during which the ring current particles were lost and the ring current returned to its equilibrium state. The recovery phase is shown with the blue bar.

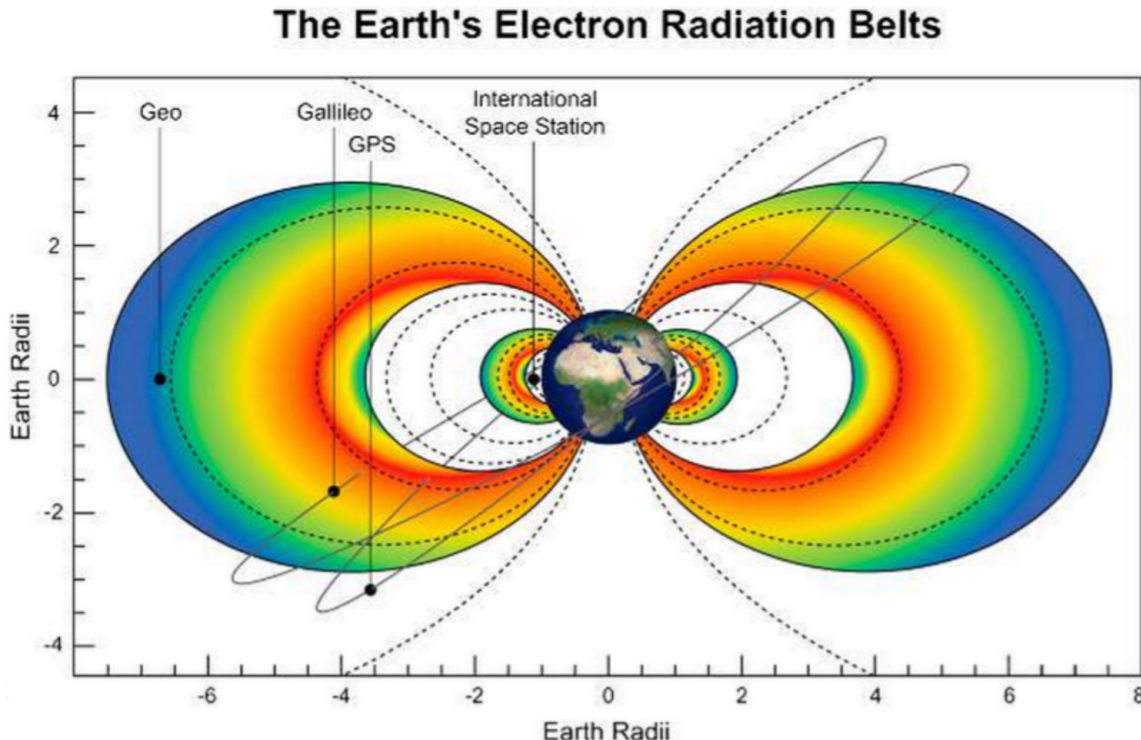


Figure 1.5: The two radiation belts with the locations of various satellites and orbits. Figure from (Horne et al., 2013).

Radiation Belts The highest particle energy populations are in the Van Allen radiation belts. These belts were discovered by Van Allen (1959) and Vernov and Chudakov (1960) during the Cold War and are a pair of toroidally shaped populations of trapped electrons and protons shown in Fig. 1.5. Their quiescent toroidal shape, similar to the shape of the plasmasphere and ring current, is a result of Earth's dipole magnetic field.

The inner radiation belt is extremely stable on year time periods, extends to  $L \approx 3$ , and mainly consists of protons with energies between MeV and GeV and electrons with energies up to  $\approx 1$  MeV (Claudepierre et al., 2019). The source of inner radiation belt protons is believed to be due to cosmic-ray albedo neutron decay (e.g. Li et al., 2017) and inward radial diffusion for electrons (e.g. O'Brien et al.,

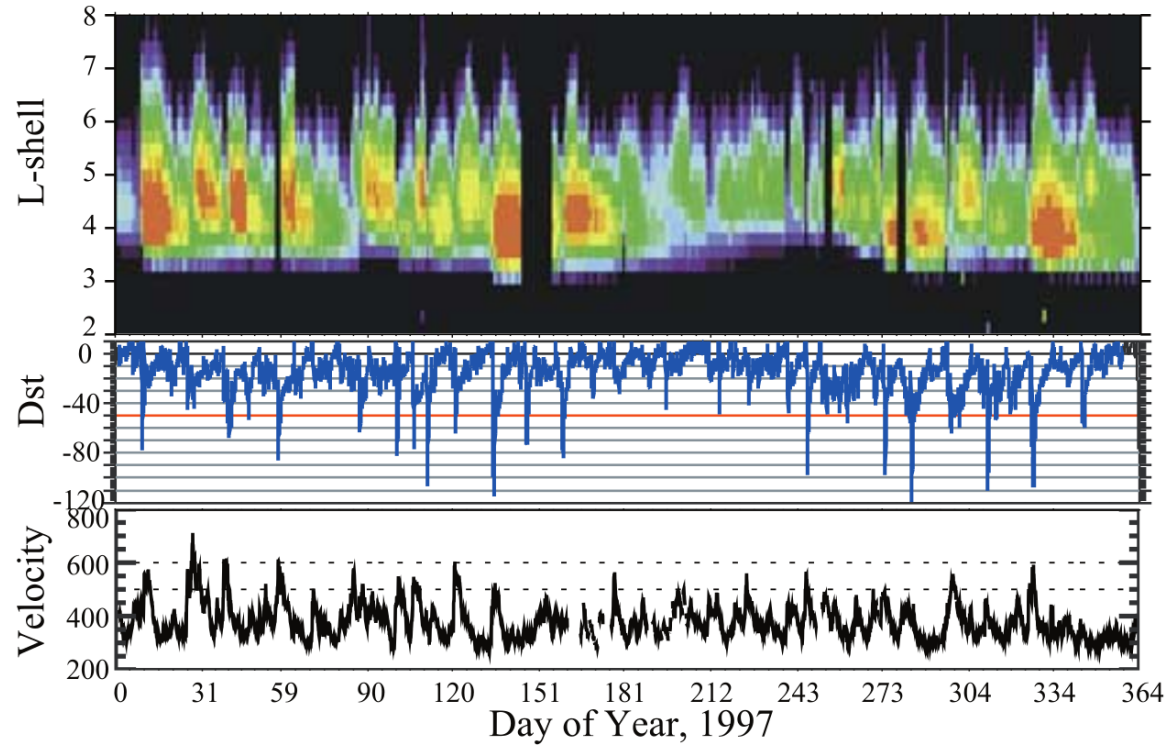


Figure 1.6: The dynamics of the outer radiation belt in 1997 from the POLAR satellite. Top panel shows the 1.2-2.4 MeV electron flux as a function of L and 1997 day of year. The middle panel shows the DST index, and bottom panel shows the solar wind velocity. Figure from (Reeves et al., 2003).

2016a). The gap between the inner and outer radiation belt is called the slot, which is believed to be due to hiss waves inside the plasmasphere (described below) scattering particles into the atmosphere (e.g. Breneman et al., 2015; Lyons and Thorne, 1973).

The outer radiation belt is much more dynamic and consists of mainly electrons of energies up to a few MeV. The outer belt's spatial extent is highly variable as shown in Fig. 1.6, and is typically observed between L of 4 and 8. The source of outer radiation belt electrons is widely believed to be injections of plasma from the magnetotail that is then accelerated to high energies.

### Charged Particle Motion in Electric and Magnetic Fields

A charged particle trapped in the magnetosphere will experience three types of periodic motion in Earth's nearly dipolar magnetic field in the absence of electric fields. The three motions are ultimately due to the Lorentz force that a particle of momentum  $\vec{p}$ , charge  $q$ , and velocity  $\vec{v}$  experiences in an electric field  $\vec{E}$  and magnetic field  $\vec{B}$  and is given by

$$\frac{d\vec{p}}{dt} = q(\vec{E} + \vec{v} \times \vec{B}). \quad (1.1)$$

For many vector quantities in this dissertation, we will adopt a widely-used convention by splitting up vectors into parallel,  $x_{||}$ , and perpendicular,  $x_{\perp}$  components with respect to the background magnetic field. In the magnetosphere, the three periodic motions, in decreasing frequency, are gyration, bounce, and drift and are schematically shown in Fig. 1.7. Each periodic motion has a corresponding conserved quantity or adiabatic invariant.

The highest frequency periodic motion is gyration about a magnetic field of

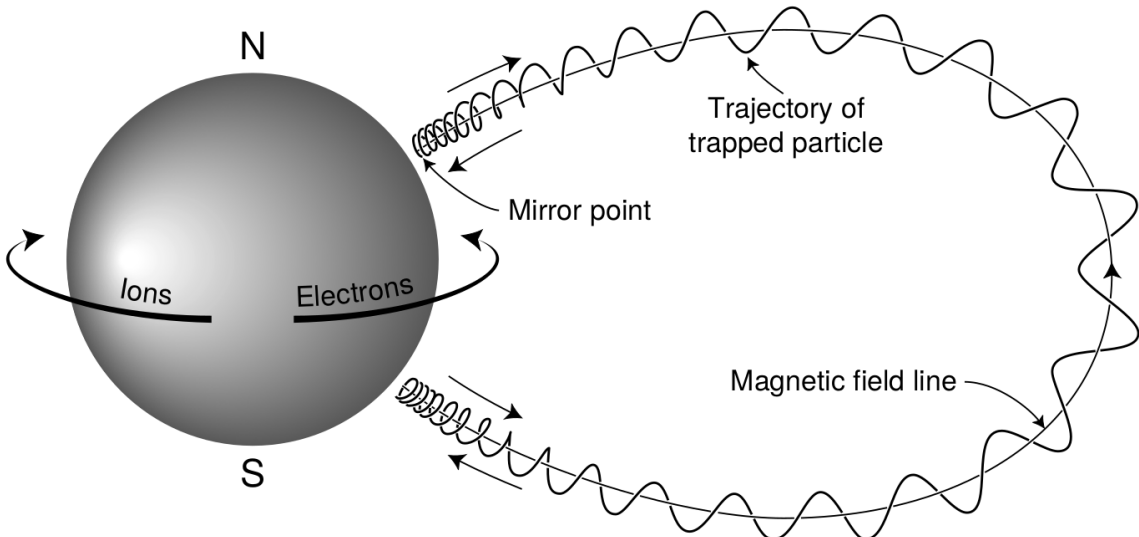


Figure 1.7: The three periodic motions of charged particles in Earth's dipole magnetic field. These motions are: gyration about the magnetic field line, bounce motion between the magnetic poles, and azimuthal drift around the Earth. Figure from (Baumjohann and Treumann, 1997).

magnitude  $B$ . This motion is circular with a Larmor radius of

$$r = \frac{mv_{\perp}}{|q|B} \quad (1.2)$$

where  $m$  is the mass and  $v_{\perp}$  the particle's velocity perpendicular to  $\vec{B}$ . This motion has a corresponding gyrofrequency of

$$\Omega = \frac{|q|B}{m} \quad (1.3)$$

in units of radians/second. In the radiation belts, the electron gyrofrequency,  $\Omega_e$ , is on the order of a kHz near the magnetic equator. The corresponding adiabatic invariant is found by integrating the particle's canonical momentum around the particle's path of gyration,

$$J_i = \oint (\vec{p} + q\vec{A}) \cdot d\vec{l} \quad (1.4)$$

where  $J_i$  is the  $i^{th}$  adiabatic invariant and  $\vec{A}$  is the magnetic vector potential. This integral is carried out by integrating the first term over the circumference of the gyro orbit and integrating the second term using Stokes theorem to calculate the magnetic flux enclosed by the gyro orbit. The gyration invariant is  $J_1 \sim v_{\perp}^2/B$  which is conserved when the frequency,  $\omega$ , of a force acting on the gyrating electron satisfies  $\omega \ll \Omega_e$ .

The second highest frequency periodic motion is bouncing due to a parallel gradient in  $\vec{B}$ . This periodic motion naturally arises in the magnetosphere because Earth's magnetic field is stronger near the poles. To understand this motion we first we need to define the concept of pitch angle,  $\alpha$  as the angle between  $\vec{B}$  and  $\vec{v}$  which is schematically shown in Fig. 1.8a. The pitch angle relates  $v$  with  $v_{\perp}$  and  $v_{\parallel}$ , the component of the particles velocity parallel to  $\vec{B}$ . As shown in Fig. 1.8b and 1.8c, a smaller (larger)  $\alpha$  will increase (decrease) the distance that the charged particle travels parallel to  $\vec{B}$  during one gyration.

Assuming the particle's kinetic energy is conserved, the conservation of  $J_1$  implies that given a particle's  $v_{\perp}(0)$  and  $B(0)$  at the magnetic equator (where Earth's magnetic field is usually at a minimum) we can calculate its  $v_{\perp}(s)$  along the particle's path,  $s$ , by calculating  $B(s)$  from magnetic field models. Thus the particle's perpendicular velocity is then related via

$$\frac{v_{\perp}^2(0)}{B(0)} = \frac{v_{\perp}^2(s)}{B(s)} \quad (1.5)$$

which can be rewritten as

$$\frac{v^2 \sin^2 \alpha(0)}{B(0)} = \frac{v^2 - v_{\parallel}^2(s)}{B(s)} \quad (1.6)$$

and re-arranged to solve for  $v_{||}(s)$  by

$$v_{||}(s) = v \sqrt{1 - \frac{B(s)}{B(0)} \sin^2 \alpha(0)} \quad (1.7)$$

which will tend towards 0 as the second term in the radical approaches 1.

The location where  $v_{||}(s) = 0$  is called the mirror point and is where a particle stops and reverses direction. Since Earth's magnetic field is stronger towards both poles, the mirroring particle will execute periodic bounce motion between two mirror points in the northern and southern hemispheres. The corresponding adiabatic invariant,  $J_2$  is

$$J_2 = \oint p_{||} ds \quad (1.8)$$

where  $ds$  describes the particle path between the mirror points in the northern and southern hemispheres (see Fig. 1.7).  $J_2$  is found by substituting Eq. 1.7 into Eq. 1.8 and defining the magnetic field strength at the mirror points as  $B_m$  (where  $\alpha(m) = 90^\circ$ ). The  $J_2$  integral can be written as

$$J_2 = 2p \int_{m_n}^{m_s} \sqrt{1 - \frac{B(s)}{B(m)}} ds \quad (1.9)$$

where  $m_n$  and  $m_s$  are the northern and southern mirror points, respectively. The bounce period can be estimated (e.g. Baumjohann and Treumann, 1997) to be

$$t_b \approx \frac{LR_e}{\sqrt{W/m}} (3.7 - 1.6 \sin \alpha(0)) \quad (1.10)$$

where  $W$  is the particle's kinetic energy. As with gyration, the particle will bounce between the mirror points as long as  $\omega \ll \Omega_b$ , where  $\Omega_b$  is the bounce frequency.

At this stage it is instructional to introduce loss cone pitch angle,  $\alpha_L$ .

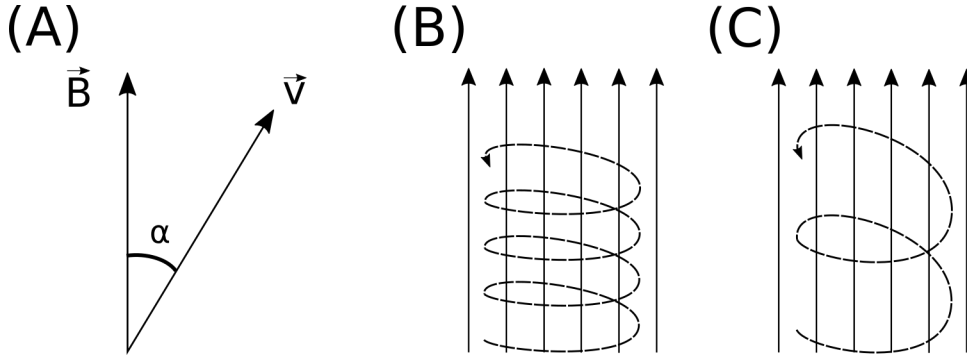


Figure 1.8: Charged particle motion in a uniform magnetic field  $\vec{B}$ . Panel (A) shows the geometry defining the pitch angle,  $\alpha$ . Panel (B) and (C) show two helical electron trajectories with dashed lines assuming a large and small  $\alpha$  (corresponding to a small and large parallel velocity  $v_{||}$ ), respectively.

Conventionally, the loss cone pitch angle is defined as the pitch angle where a particle will mirror at  $\approx 100$  km altitude in the atmosphere. A charged particle gyrating at those altitudes will encounter, and likely Coulomb scatter, with the dense atmosphere and be lost. The 100 km altitude is only a convention and not a hard boundary, e.g. the peak in the 1 MeV electron ionization rate is at  $\approx 60$  km altitudes (Fang et al., 2010).

The slowest periodic motion experienced by charged particles in Earth's magnetic field is azimuthal drift around the Earth. This drift primarily results from a combination of a radial gradient in  $\vec{B}$  and the curvature of the magnetic field. The radial gradient drift arises because Earth's magnetic field is stronger near the Earth. The particle's gyroradius shrinks as it gyrates towards Earth, and expands when it gyrates away from Earth. The overall effect is the particle gyro orbit does not close on itself causing eastward drift of negatively charged particles and westward drift of positively charged particles. The radial gradient drift is further enhanced by the centrifugal force that a particle experiences as it bounces along the curved field lines. The drift adiabatic invariant,  $J_3$  is found by integrating Eq. 1.4 over the complete

particle orbit around the Earth. The shape of this drift orbit is known as a drift shell, and can be visualized by rotating the trapped particle trajectory in Fig. 1.7 around the axis that connects the poles. For  $J_3$ , the first term is negligible and the second term is the magnetic flux enclosed by the drift shell,  $\Phi_m$  i.e.  $J_3 \sim \Phi_m$ .

To quantify the frequencies of the three periodic motions, Fig. 1.9 from Schulz and Lanzerotti (1974) shows contours of the gyration, bounce, and drift frequencies for electrons and protons in Earth's dipole magnetic field.

Up until now we have considered the three periodic motions due Earth's magnetic field in the absence of electric fields. If there is an electric field,  $\vec{E}$ , perpendicular to  $\vec{B}$ , a particle's center of gyration (averaged position of the particle over a gyration) will drift with a velocity perpendicular to both  $\vec{E}$  and  $\vec{B}$ . The drift velocity can be solved using Eq. 1.1 and is

$$\vec{v}_E = \frac{\vec{E} \times \vec{B}}{B^2}. \quad (1.1)$$

If there is a parallel magnetic field,  $E_{||}$ , then the particle is accelerated along the magnetic field line. An  $E_{||}$  pointing away from the Earth will contribute to the mirror force and raise the particle's mirror point. On the contrary, an Earthward pointing  $E_{||}$  will oppose the mirror force and lower the mirror point. If the Earthward  $E_{||}$  lowers the mirror point into the atmosphere, those particles will precipitate into the atmosphere.

### Radiation Belt Particle Sources and Sinks

Due to the highly energetic and dynamic nature of the radiation belts, and their impact on space exploration, the radiation belts have been studied for over half a century. Researchers have studied and attempted to predict the dynamics of radiation belt particles, waves, and wave-particle interactions by considering various

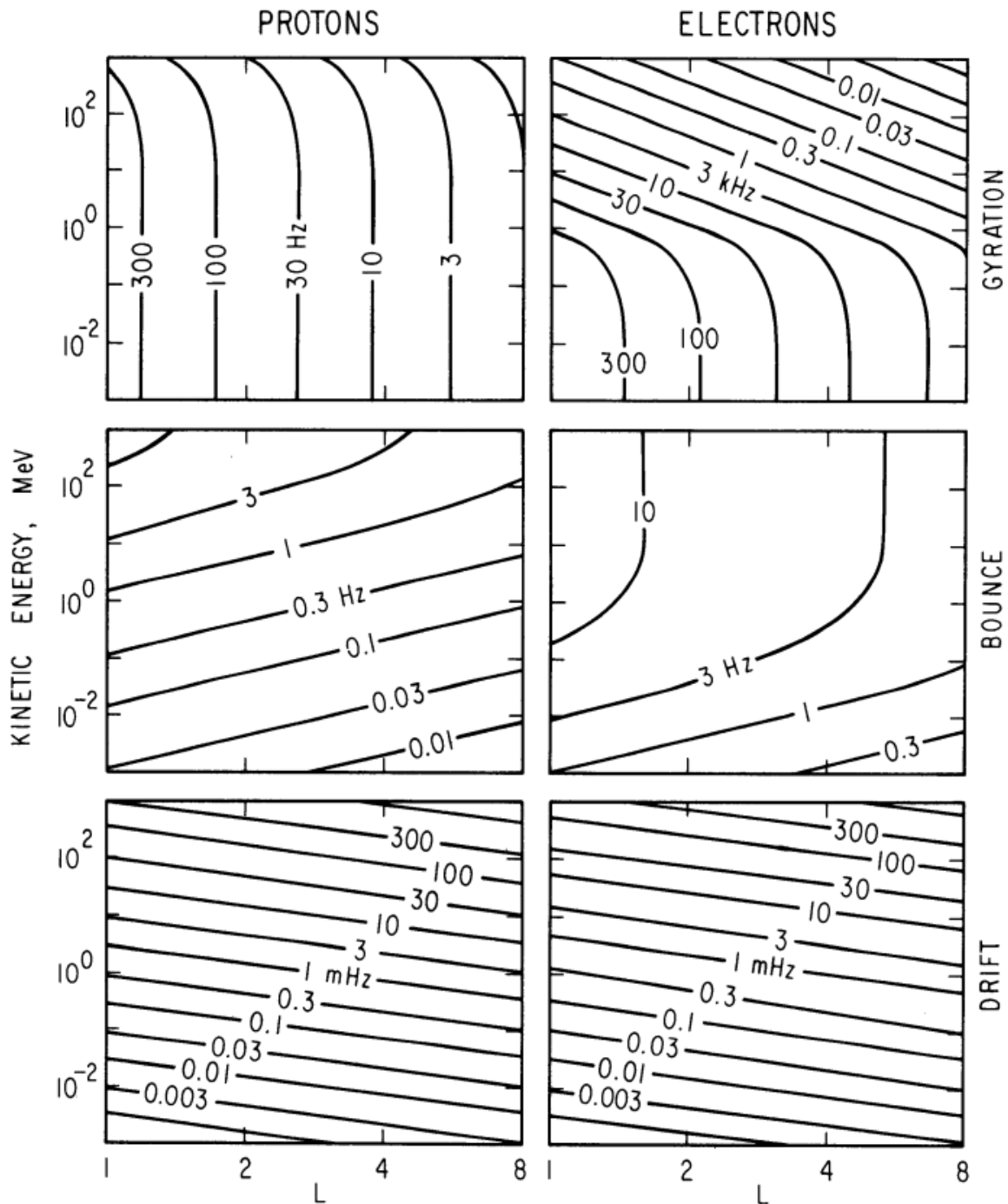


Figure 1.9: Contours of constant gyration, bounce, and drift frequencies for electrons and protons in a dipole field. Figure from Schulz and Lanzerotti (1974).

competing particle acceleration and loss mechanisms which are described below.

### Adiabatic Heating

One of the particle heating and transport mechanisms arises from the earthward convection of particles. As shown in Eq. 1.5, the conservation of  $J_1$  implies that the initial and final  $v_\perp$  depends on the change in the magnetic field magnitude. As a particle convects earthward  $B_f > B_i$  and thus  $v_\perp$  must also increase. The dipole magnetic field magnitude falls off radially as  $B \sim L^{-3}$ , and the change in  $v_\perp^2$  as the particle convects towards a stronger magnetic field is

$$\frac{v_{\perp f}^2}{v_{\perp i}^2} = \left( \frac{L_i}{L_f} \right)^3. \quad (1.12)$$

For a particle convecting earthward, if  $J_2$  is conserved, its  $v_\parallel$  also increases because the distance between the particle's mirror points decreases. Calculating the increase in  $v_\parallel$  is somewhat difficult and is approximately

$$\frac{v_{\parallel f}^2}{v_{\parallel i}^2} = \left( \frac{L_i}{L_f} \right)^k \quad (1.13)$$

where  $k$  ranges from 2 for equatorial pitch angles,  $\alpha_{eq} = 0^\circ$ , to 2.5 for  $\alpha_{eq} = 90^\circ$  (Baumjohann and Treumann, 1997). Since the rate of adiabatic heating is greater in the perpendicular direction than heating in the parallel direction, an initially isotropic particle distribution will become anisotropic during its convection. These isotropic particles can then become unstable to wave growth and generate waves in order to reach equilibrium.

### Wave Resonance Heating

Another mechanism that heats particles is caused by particles resonating with plasma waves. A few of the electromagnetic wave modes responsible for particle

acceleration (and scattering) relevant to radiation belt dynamics are hiss, whistler mode chorus (chorus), and electromagnetic ion cyclotron (EMIC) waves. These waves are created by the loss cone instability that is driven by an anisotropy of electrons for chorus waves, and protons for EMIC waves. The level of anisotropy can be quantified by the ratio of the perpendicular to parallel particle temperatures ( $T_{\perp}/T_{\parallel}$ ). A particle distribution is unstable when  $T_{\perp}/T_{\parallel} > 1$ . Since electrons gyrate in a right-handed sense, the chorus waves also tend to be right hand circularly polarized (Tsurutani and Lakhina, 1997). The same argument also applies to protons and left hand circularly polarized EMIC waves.

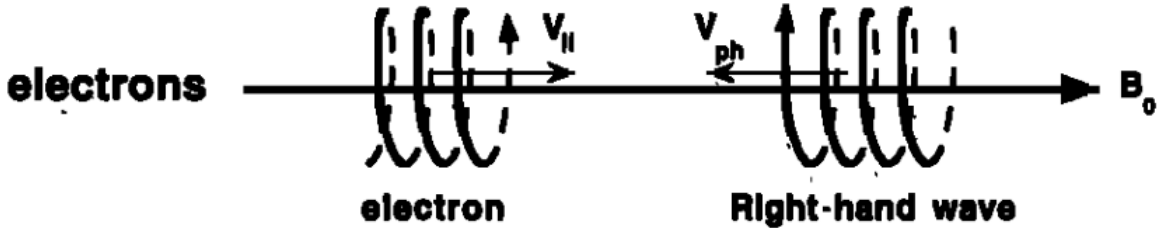
These circularly polarized waves can resonate with electrons and/or protons when their relative motion results in a static  $\vec{E}$  in the particle's reference frame. One example of a resonance between a right hand circularly polarized wave and an electron is shown in Fig. 1.10. The electron's  $v_{\parallel}$  and the wave's parallel wave vector,  $k_{\parallel}$ , are in opposite directions such that the wave frequency,  $\omega$ , is Doppler shifted to an integer multiple of the  $\Omega_e$  where the electron feels a static electric field and is accelerated or decelerated. Quantitatively, this resonance condition is easier to understand with the following toy model.

Assume a uniform magnetic field,  $\vec{B} = B_0\hat{z}$ , with a parallel propagating ( $k = k\hat{z}$ ), right-hand circularly polarized wave. The wave's electric field as a function of position and time can be written as

$$\vec{E} = E_0(\cos(\omega t - kz)\hat{x} + \sin(\omega t - kz)\hat{y}). \quad (1.14)$$

The angular component of  $\vec{E}$  that will effect the particle's  $v_{\perp}$  is

$$E_{\theta} = \vec{E} \cdot \hat{\theta} = E_0 \cos(\omega t - kz + \theta). \quad (1.15)$$



$$\omega + k_{\parallel} v_{\parallel} = \Omega^-$$

Figure 1.10: The trajectories of an electron and a right-hand circularly polarized wave during a cyclotron resonance. The electron's  $v_{\parallel}$  and the wave's  $k_{\parallel}$  are in opposite directions such that the wave's frequency is Doppler shifted to an integer multiple of the electron cyclotron frequency. Figure from (Tsurutani and Lakhina, 1997).

Now assume that the electron is traveling in the  $-\hat{z}$  direction with a velocity,  $\vec{v} = -v_0 \hat{z}$ , so its time dependent position along  $\hat{z}$  is

$$z(t) = -v_0 t \quad (1.16)$$

and gyrophase is

$$\theta(t) = -\Omega t + \theta(0) \quad (1.17)$$

where the first negative sign comes from the electron's negative charge. Now we put this all together into Eq. 1.1 and find the force that the electron will experience

$$m \frac{dv_{\theta}}{dt} = qE_{\theta} = qE_0 \sin((\omega + kv_0 - \Omega)t + \theta(0)). \quad (1.18)$$

This is a relatively complex expression, but when the time dependent component is zero, i.e.

$$\omega + kv_0 - \Omega = 0, \quad (1.19)$$

the electron will feel a static electric field and be accelerated or decelerated depending on  $\theta(0)$ , the phase between the wave and the electron. The expression in Eq. 1.19 is commonly referred to as the resonance condition and is more generally written as

$$\omega - k_{||}v_{||} = \frac{n\Omega_e}{\gamma} \quad (1.20)$$

where  $n$  is the resonance order, and  $\gamma$  is the relativistic correction (e.g. Millan and Thorne, 2007). In the case of the cyclotron resonance ( $n = 1$ ), the wave and cyclotron frequencies are approximately equal and thus  $J_1$  is violated. Since  $J_1$  is violated,  $J_2$  and  $J_3$  are also violated since the conditions required to violate  $J_2$  and  $J_3$  are less stringent than  $J_1$ .

It is important to remember that a particle will experience the effects of many waves along its drift orbit. The typical MLT extent of a handful of waves that are capable of resonating with radiation belt electrons are shown in Fig. 1.11.

### Particle Losses

Now that we have seen two general mechanisms with which particles are accelerated in the magnetosphere, we will consider a few specific mechanisms that remove particles from the magnetosphere into the atmosphere or the solar wind. One mechanism that transports magnetosperic particles into the solar wind is magnetopause shadowing (e.g. Ukhorskiy et al., 2006). Magnetopause shadowing occurs when the ring current is strengthened and Earth's magnetic field strength is increased outside of the ring current. If the ring current increases slowly enough (such that  $J_3$  is conserved), a particle drift shell will move outward to conserve  $J_3$ . If the particle's drift shell expands past the magnetopause, the particle will be lost to the solar wind.

Another particle loss (and acceleration) mechanism is called radial diffusion and

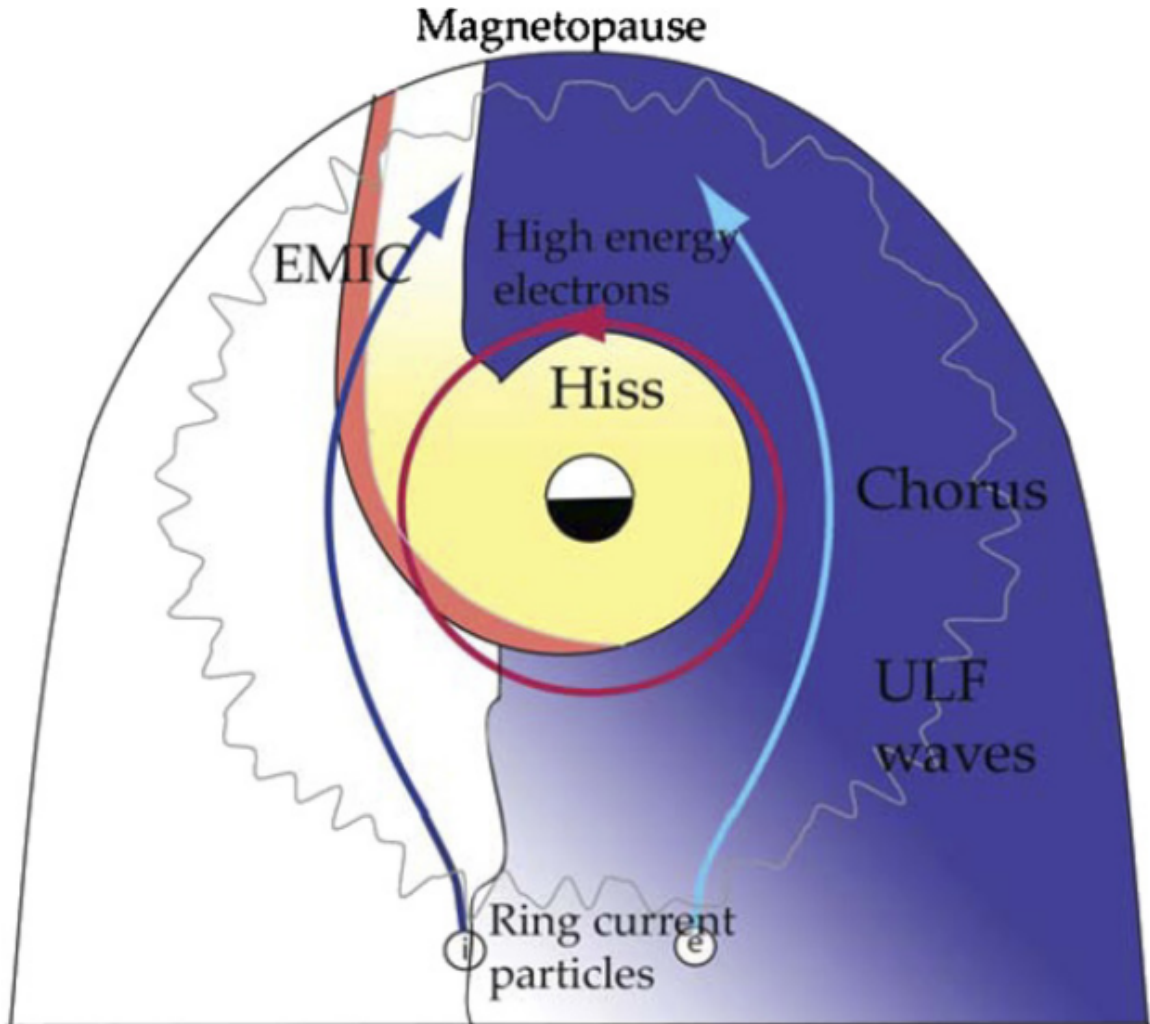


Figure 1.11: Various wave modes in the magnetosphere. Ultra low frequency waves occur through the magnetosphere. Chorus waves are typically observed in the 0-12 midnight-dawn region. EMIC waves are typically observed in the dusk MLT sector. Hiss waves are observed inside the plasmasphere. Figure from Millan and Thorne (2007).

is driven by ultra low frequency (ULF) modulation of Earth's magnetic field. For example, if the solar wind compresses the magnetopause on time scales shorter than the drift period, particles will experience radial diffusion. If the transport is radially inward, particles will be accelerated. On the other hand, radially outward radial diffusion can transport particles through the magnetopause where they will be lost to the solar wind. Reeves et al. (2013) investigated the driver of particle acceleration during the October 2012 storm and observationally found that inward radial diffusion was not dominant, rather local acceleration via wave-resonance heating appeared to be the dominant acceleration mechanism.

The loss mechanism central to this dissertation is pitch angle and energy scattering of electrons by waves. Some of the waves that scatter electrons in energy and pitch angle in the inner magnetosphere are: plasmaspheric hiss (e.g. Breneman et al., 2015; O'Brien et al., 2014), EMIC waves (e.g. Capannolo et al., 2019; Hendry et al., 2017), and chorus waves (e.g. Breneman et al., 2017; Kasahara et al., 2018; Ozaki et al., 2019). These wave-particle interactions occur when the resonance condition in Eq. 1.20 is satisfied and the particle's energy and  $\alpha$  is modified by the wave. More details regarding the theory of pitch angle and energy diffusion is given in Chapter 2. If the wave changes  $\alpha$  towards zero and  $\alpha < \alpha_L$ , then the particle's mirror point dips below 100 km altitude where the particle can be lost from the magnetosphere. One manifestation of pitch angle scattering of particles into the loss cone are microbursts, a sub-second duration impulse of electrons.

### Microbursts

Microbursts were first seen with high altitude balloons which measured bremsstrahlung X-rays emitted by microburst electrons impacting the atmosphere by Anderson and Milton (1964). In the following years, numerous balloon flights expanded our

knowledge of non-relativistic ( $< 500$  keV) microbursts by quantifying the microburst spatial extent, temporal width, occurrence frequency, extent in L and MLT, and their source. It is worth noting that relativistic microbursts have not yet been observed by high altitude balloons. The microburst source was initially believed to be either a local plasma instability or a propagating disturbance in the magnetosphere (Barcus et al., 1966; Brown et al., 1965; Parks, 1967; Trefall et al., 1966). Soon after, both non-relativistic and relativistic microburst electrons were directly observed in LEO with spacecraft including the Solar Anomalous and Magnetospheric Particle Explorer (SAMPEX) (e.g. Blake et al., 1996; Blum et al., 2015; Douma et al., 2019, 2017; Greeley et al., 2019; Lorentzen et al., 2001a,b; Nakamura et al., 1995, 2000; O'Brien et al., 2004, 2003), Montana State University's (MSU) Focused Investigation of Relativistic Electron Bursts: Intensity, Range, and Dynamics II (FIREBIRD-II) (Anderson et al., 2017; Breneman et al., 2017; Crew et al., 2016; Klumpar et al., 2015; Spence et al., 2012), and Science Technologies Satellite (STSAT-I) (e.g. Lee et al., 2012, 2005). An example microburst time series is shown in Fig. 1.12 and was observed by the FIREBIRD-II CubeSats. The prominent features of the example microbursts in Fig. 1.12 are their sub-second duration, half order of magnitude increase in count rate above the falling background, and their 200-800 keV energy extent.

Microbursts are observed on magnetic field footprints that are connected to the outer radiation belt (approximately  $4 < L < 8$ ). They are predominately observed in the 0-12 MLT sector with an elevated occurrence frequency during magnetospherically disturbed times as shown in Fig. 1.13. O'Brien et al. (2003) used SAMPEX relativistic electron data and found that microbursts predominately occur during the main phase of storms, with a heightened occurrence rate during the recovery phase. Microburst occurrence rates are also higher during high solar wind velocity events e.g. from

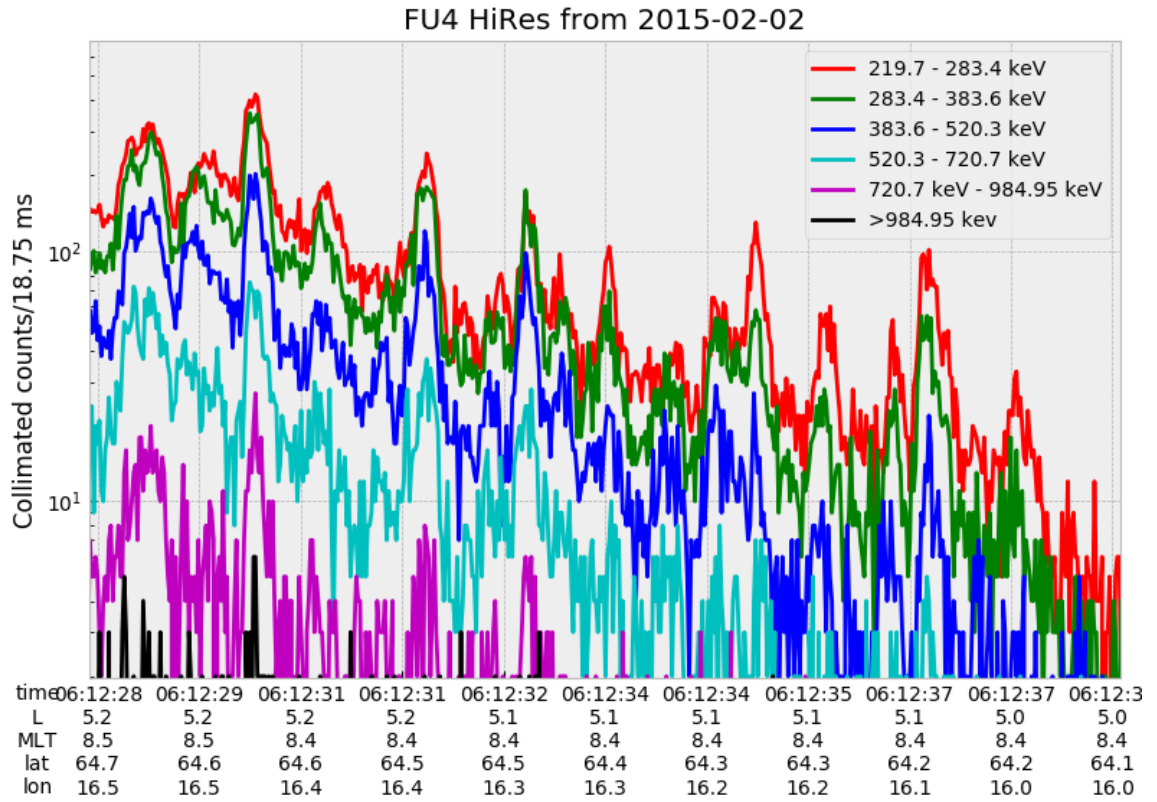


Figure 1.12: An example train of microbursts observed by FIREBIRD-II unit 4 on February 2nd, 2015. The colored curves show the differential energy channel count rates in five channels from  $\approx 200$  keV to 1 MeV and a sixth integral energy channel with a 1 MeV threshold. The x-axis labels show auxiliary information such as time of observation and the spacecraft position in L, MLT, latitude and longitude coordinates.

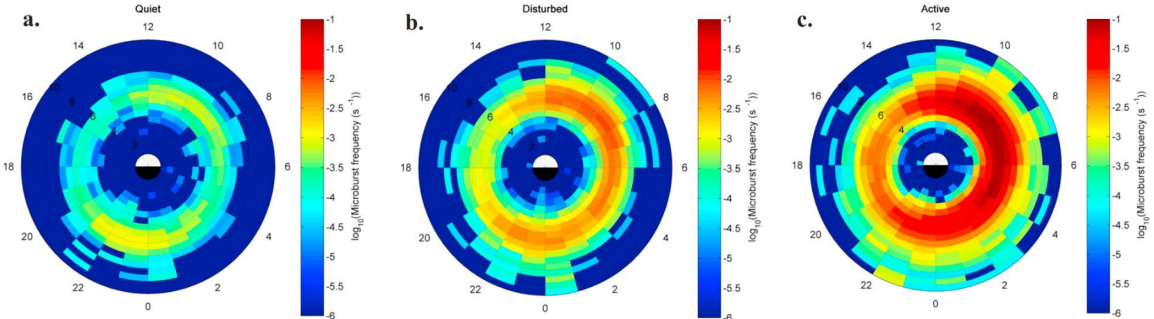


Figure 1.13: Distribution of  $> 1$  MeV microburst occurrence rates as a function of  $L$  and MLT. The three panels show the microburst occurrence rate dependence on geomagnetic activity, parameterized by the auroral electrojet (AE) index for (a)  $\text{AE} < 100 \text{ nT}$ , (b)  $100 < \text{AE} < 300 \text{ nT}$  and (c)  $\text{AE} > 300 \text{ nT}$ . Figure from Douma et al. (2017).

co-rotating interaction regions (Greeley et al., 2019; O'Brien et al., 2003).

The estimated impact of microbursts on the atmosphere and the radiation belts is significant. Relativistic microburst electrons impacting the atmosphere are ionized at  $< 100$  km altitudes, with higher energy electrons penetrating closer to the surface. The resulting chemical reaction of microburst electrons impacting the atmosphere produces odd hydrogen  $\text{HO}_x$  and odd nitrogen  $\text{NO}_x$  molecules, which are partially responsible for destroying ozone ( $\text{O}_3$ ). Seppälä et al. (2018) modeled a six hour relativistic microburst storm and found that the mesospheric ozone was reduced by 7 – 12% in the summer months and 12 – 20% in the winter months, so microbursts may have a non-negligible contribution to the dynamics of atmospheric ozone. Furthermore, microbursts have also been estimated to have a significant impact on the outer radiation belt electron population. The loss of all radiation belt electrons due to microbursts have been estimated to be on the order of a day (Breneman et al., 2017; Douma et al., 2019; Lorentzen et al., 2001b; O'Brien et al., 2004; Thorne et al., 2005).

The wave-particle interactions responsible for generating microbursts are also

believed to accelerate electrons in the radiation belts. As mentioned earlier, when an electron is in resonance with a wave, energy is exchanged with the wave and the electron is either accelerated or decelerated. The signature of wave-particle acceleration been observed for radiation belt electrons (e.g. Horne et al., 2005; Meredith et al., 2002; Reeves et al., 2013), and O'Brien et al. (2003) presented evidence that enhancements in chorus waves, microbursts, and radiation belt electrons are related. To explain their observations, O'Brien et al. (2003) proposed that microburst precipitation is a side effect of electron acceleration due to chorus waves.

The widely used theoretical framework to model the wave-particle interactions responsible for accelerating electrons and scattering microbursts is quasi-linear diffusion (e.g. Horne et al., 2005; Meredith et al., 2002; Summers, 2005; Summers et al., 1998; Thorne et al., 2005; Walker, 1993). This framework is explained in Chapter 2, and applied to an observation of a microburst in the heart of the radiation belt. Qualitatively, when a particle is resonant with a wave it can either be transported in pitch angle towards the loss cone and lose energy to the wave, or transported away from the loss cone and gain energy from the wave.

As previously mentioned, the range of observed microburst energies range from a few tens of keV (e.g Datta et al., 1997; Parks, 1967) to greater than 1 MeV (e.g. Blake et al., 1996; Greeley et al., 2019). The microburst electron flux ( $J$ ) falls off in energy, and the microburst energy spectra is typically well fit to a decaying exponential

$$J(E) = J_0 e^{-E/E_0} \quad (1.21)$$

where  $J_0$  is the flux at 0 keV (unphysical free parameter) and  $E_0$  quantifies the efficiency of the scattering mechanism in energy (e.g. Datta et al., 1997; Lee et al., 2005; Parks, 1967). A small  $E_0$  suggests that mostly low energy particles are scattered.

In contrast a high  $E_0$  suggests that the scattering mechanism scatters low and high energy electrons. Reality is a bit more messy and a high  $E_0$  may be a signature of a scattering mechanism that is most efficient at scattering high energy electrons, with a relatively minor efficiency to scatter low energy electrons. Since there are many more low energy electrons available to scatter, there may be relatively more low energy electrons scattered.

The short microburst duration, as observed by a single LEO satellite in a highly inclined orbit (motion is mostly latitudinal), has an ambiguity when interpreting what is a microburst. The two possible realities are: a microburst is very narrow in latitude and persistent, or transient. There are a few ways to distinguish between the two possible realities, and each one has a unique set of advantages.

A high altitude balloon essentially provides a stationary view of the precipitating particles under the radiation belt footprints. An intense transient microburst can be unambiguously identified above the slowly varying background. On the other hand, if the microburst precipitation is stationary, there will be too little contrast between the microburst and the background fluxes to be found.

Multi-spacecraft missions provide an alternate solution that can determine if a microburst is a spatial or a transient phenomena. As is illustrated in Fig. 1.14, a transient microburst can be recognized if two spacecraft, one trailing the other, simultaneously observe it. The size of the microburst footprint must then be larger than the spacecraft separation. On the contrary, if two spacecraft observe a microburst-like feature at the same location but at different times, then the feature is stationary and may be a curtain (Blake and O'Brien, 2016). Both balloon and multi-spacecraft observational methods have a unique set of strengths. This dissertation takes the multi-spacecraft approach to identify and study microbursts.

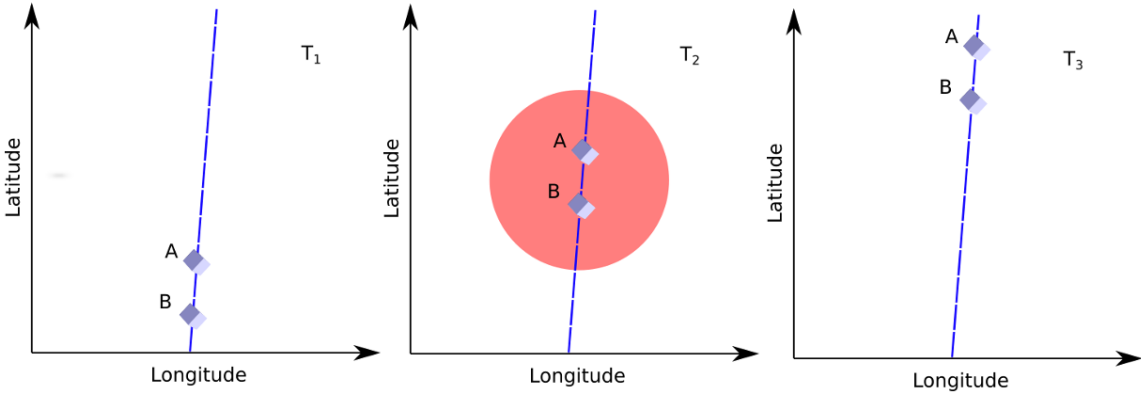


Figure 1.14: Three snapshots of a temporal microburst observed simultaneously by a pair of polar-orbiting spacecraft. The spacecraft are identified by labels "A" and "B" and are traveling upwards on the blue dashed orbital track. At  $T_1$  the spacecraft are traveling upwards and no microburst is observed. Then at  $T_2$  both spacecraft simultaneously observe a microburst shown by the red circle and the microburst size must be greater than the spacecraft separation. In the last snapshot,  $T_3$ , the microburst has precipitated and no longer observed by the spacecraft.

### Scope of Research

This dissertation furthers our understanding of the microburst scattering mechanism by presenting observational evidence of microburst scattering directly, and measuring microburst sizes and comparing them to the size of chorus waves. Chapter 2 describes a microburst scattering event observed by NASA's Van Allen Probes. For this event, particle and wave measurements were analyzed and modeled in the theoretical framework of pitch angle and energy diffusion. The following two chapters present studies of microburst sizes in comparison to chorus waves. Chapter 3 describes a bouncing packet microburst observation made by the FIREBIRD-II mission where the microburst's lower bound longitudinal and latitudinal sizes were estimated. Chapter 4 expands the case study from Chapter 3 to a statistical study of microburst sizes using The Aerospace Corporation's AeroCube-6 (AC6) CubeSats. In this study, a Monte Carlo and analytic microburst size models were developed

to account for the compounding statistical effects of random microburst sizes and locations. Lastly, Chapter 5 will summarize this work and make concluding remarks regarding outstanding questions in microburst physics.

EVIDENCE OF MICROBURSTS OBSERVED NEAR THE EQUATORIAL  
PLANE IN THE OUTER VAN ALLEN RADIATION BELT

Contribution of Authors and Co-Authors

Manuscript in Chapter 1

Author: Mykhaylo Shumko

Contributions: Found the microburst event and applied the quasi-linear diffusion theory to the observation.

Co-Author: Drew L. Turner

Contributions: Mentor who helped organize this paper and provided networking opportunities with the Van Allen Probes team.

Co-Author: T. P. O'Brien

Contributions: Mentor who proposed the quasi-linear diffusion theory analysis and helped with the analysis.

Co-Author: Seth G. Claudepierre

Contributions: Visualized the MagEIS data in a way that led to this discovery. Helped process the MagEIS data.

Co-Author: John Sample

Contributions: Provided analysis advice.

Co-Author: D. P. Hartley

Contributions: Processed the EMFISIS high resolution data.

Co-Author: Joseph Fennell

Contributions: Provided advice to interpret the observations.

Co-Author: J. Bernard Blake

Contributions: Provided advice to interpret the observations and principal investigator of MagEIS.

Co-Author: Matina Gkioulidou

Contributions: Helped correctly use the RBSPICE data.

Co-Author: Donald G. Mitchell

Contributions: Helped correctly use the RBSPICE data and principal investigator of RBSPICE.

Manuscript Information

Mykhaylo Shumko, Drew L. Turner, T. P. O'Brien, Seth G. Claudepierre, John Sample, D. P. Hartley, Joseph Fennell, J. Bernard Blake, Matina Gkioulidou, and Donald G. Mitchell

Status of Manuscript:

- Prepared for submission to a peer-reviewed journal
- Officially submitted to a peer-reviewed journal
- Accepted by a peer-reviewed journal
- Published in a peer-reviewed journal

Geophysical Research Letters Volume 45, Issue 16

DOI: 10.1029/2018GL078451

Key Points

- First report of direct observation of microbursts at high altitude, near the equatorial plane.
- Microbursts' duration, flux enhancement, and energy spectra are similar to prior observations in LEO.
- Microburst generation is not consistent with a single quasi-linear gyroresonant interaction with chorus waves.

Abstract

We present the first evidence of electron microbursts observed near the equatorial plane in Earth's outer radiation belt. We observed the microbursts on March 31st, 2017 with the Magnetic Electron Ion Spectrometer and RBSP Ion Composition Experiment on the Van Allen Probes. Microburst electrons with kinetic energies of 29-92 keV were scattered over a substantial range of pitch angles, and over time intervals of 150-500 ms. Furthermore, the microbursts arrived without dispersion in energy, indicating that they were recently scattered near the spacecraft. We have applied the relativistic theory of wave-particle resonant diffusion to the calculated phase space density, revealing that the observed transport of microburst electrons is not consistent with the hypothesized quasi-linear approximation.

Introduction

Since the Van Allen radiation belts were discovered by Van Allen (1959) and Vernov and Chudakov (1960), decades of work has focused on understanding their origins and effects on the near-Earth space environment and ionosphere-thermosphere

system. The energy content of the outer belt is dominated by energetic electrons, with dynamics controlled by a complex interplay between various source and loss mechanisms. One important loss and acceleration mechanism is gyroresonant diffusion in energy and pitch angle (PA) due to scattering of electrons by plasma waves (e.g. Bortnik et al., 2008; Horne and Thorne, 2003; Meredith et al., 2002; Millan and Thorne, 2007; Summers et al., 1998; Thorne and Andreoli, 1981; Thorne et al., 2005; Walker, 1993).

Chorus waves are commonly associated with PA and energy diffusion. These waves are typically generated by substorm injections into the inner magnetosphere, which lead to a temperature anisotropy of the source electrons with energies up to tens of keV (e.g. Horne et al., 2003b; Li et al., 2009a). Since these source electrons drift eastward, chorus is most frequently observed in the dawn sector, but it has been observed at all magnetic local times (MLT) (Li et al., 2009b). Chorus waves are believed to generate electron microburst precipitation through wave-particle interactions.

Microbursts are typically defined as an increase of electron flux in or near the atmospheric loss cone that last  $< 1$  s (e.g. Anderson and Milton, 1964; Blake et al., 1996; Lorentzen et al., 2001a). Empirical and theoretical analyses indicate that microbursts are an important loss process since they can substantially deplete the radiation belt electrons on the order of one day (e.g. Breneman et al., 2017; Lorentzen et al., 2001b; O'Brien et al., 2004; Thorne et al., 2005). Previously, microbursts have been observed in the upper atmosphere in the form of bremsstrahlung X-rays (e.g. Anderson et al., 2017; Parks, 1967; Woodger et al., 2015) and directly in low Earth orbit (LEO) (e.g. Blake et al., 1996; Blum et al., 2015; Breneman et al., 2017; Crew et al., 2016; Lee et al., 2012, 2005; Lorentzen et al., 2001a,b; Mozer et al., 2018; Nakamura et al., 1995, 2000; O'Brien et al., 2004, 2003).

We observed for the first time, microburst-like signatures near their hypothesized origin within the heart of the outer radiation belt. The unique microburst observations we report here were possible with the Van Allen Probe-A's (RBSP-A) Magnetic Electron Ion Spectrometer's (MagEIS) fast sampling rate ( $\sim$ 11 ms), and RBSP Ion Composition Experiment's (RBSPICE) PA coverage. The observed microbursts' duration, energy spectra, and energy dispersion signature were similar to microbursts previously reported from LEO. Furthermore, we simultaneously observed structureless "hiss-like" whistler mode wave power in the lower band chorus frequency range (Li et al., 2012). From previous observations in LEO (e.g. Blake et al., 1996), it is believed that microbursts result from the impulsive scattering of electrons into or near the loss cone, which is on the order of a few tens of degrees in LEO. With this assumption, high altitude microburst observations near the magnetic equator should be very difficult to make since the atmospheric loss cone there is only a few degrees wide. Thus, the loss cone is smaller than the angular resolution of most particle detectors. Even when an instrument is observing the loss cone, the instrument's field of view will include some portion of the trapped population. The trapped electron flux is typically orders of magnitude higher than that in the loss cone, so that microbursts scattered into the loss cone will be obscured. We present observational evidence that suggests that the sudden impulse of electrons studied here is consistent with the creation of microbursts. Furthermore, these microbursts were scattered over a broad PA range outside of the loss cone, though the loss cone was not directly observed by MagEIS and RBSICE.

This paper explores the properties of the observed microbursts by utilizing in-situ RBSP measurements of waves and particles. This unique high altitude point of view enables us to test whether the observed microburst scattering is consistent with a quasi-linear diffusion process. We have tested this hypothesis with in-situ electron

phase space density (PSD) measurements and the relativistic theory of wave-particle resonant diffusion (Summers et al., 1998; Walker, 1993) to determine if the microburst electrons diffused in PA and energy.

### Spacecraft Instrumentation

NASA's RBSP mission (Mauk et al., 2013), launched on August 30th, 2012, consists of a pair of identically instrumented spacecraft. Their orbit and instrumentation are uniquely configured to enrich our understanding of the particles and waves in the inner magnetosphere. The RBSP spacecraft are in highly elliptical, low-inclination orbit, with perigee of  $\sim$ 600 km and apogee of  $\sim$ 30,000 km altitude. Their attitude is maintained by spin-stabilization with a period of  $\sim$ 11 s and the spin axis is roughly sun-pointing. In this analysis, energetic electron measurements from MagEIS (Blake et al., 2013) and RBSPICE (Mitchell et al., 2013) were used, complemented by magnetic field and wave measurements from Electric and Magnetic Field Instrument and Integrated Science (EMFISIS) (Kletzing et al., 2013).

We observed these microbursts with RBSP-A's MagEIS low energy instrument (MagEIS-A) which measures 20-240 keV electrons. It has an angular acceptance of  $3^\circ - 10^\circ$  in the spacecraft spin plane, and  $20^\circ$  perpendicular to the spin plane. MagEIS-A has a high rate data mode which samples at 1000 angular sectors per spacecraft spin (11 ms cadence). MagEIS low on RBSP-B on the other hand samples at 64 angular sectors per spacecraft spin (172 ms cadence), so it was only used for context.

To expand the PA coverage of MagEIS-A, we used the RBSPICE-A time-of-flight instrument. RBSPICE-A measures electron energies in the range of 19 keV - 1 MeV with a fan of six telescopes (the sixth telescope is used only for calibration and was excluded from this analysis). These telescopes have an overall acceptance

angle of  $160^\circ$  by  $12^\circ$  which allows them to simultaneously sample a substantial part of the Pitch Angle Distribution (PAD). RBSPICE-A gathers data over 32 sectors per spacecraft spin ( $\approx 310$  ms cadence) and each sector is divided into three sub-sectors corresponding to three measurement modes (Manweiler and Zwiener, 2018). At the time of the observation, the sub-sector used for electron measurements had an accumulation time of 77 ms. We used RBSPICE-A's Electron Basic Rate (EBR) telemetry data in this analysis which is not averaged, though it is an integral energy channel.

To understand the dynamics of the local magnetic field, we used the EMFISIS instrument. EMFISIS provides measurements of the DC magnetic field with flux gate magnetometers. In addition, it measures electromagnetic waves from 10 Hz to 500 kHz with search coil magnetometers. The spectral matrix and burst data products used in this analysis were from the EMFISIS waveform receiver (WFR) (10 Hz - 12 kHz) and the high frequency receiver (10 kHz - 500 kHz). Burst data were selectively captured at a 35 kHz sample rate, and the survey mode spectral matrix data was captured every 6s.

### Observations

MagEIS-A and RBSPICE-A observed the microburst-like signatures on March 31st, 2017 at  $L^* \approx 6$  and  $MLT \approx 19$ , calculated with the Tsyganenko 2004 magnetic field model (Tsyganenko and Sitnov, 2005). The magnetosphere was in the recovery phase of a storm, with minimum Dst of -75 nT observed on March 27th. The local electron number density was on the order of  $1 \text{ cm}^{-3}$  at this time, so both RBSP spacecraft were located outside the plasmasphere. The two spacecraft were separated by 1700 km, at magnetic latitudes  $\lambda \approx -19^\circ$  and  $\lambda \approx -18^\circ$  for RBSP-A and RBSP-B, respectively.

MagEIS-A observed microburst electron flux ( $J$ ) at energies  $\geq 92$  keV around 11:17 UT as shown in panel (a) in Fig. 4.1. For directional information, panel (b) in Fig. 4.1 shows flux as a function of local pitch angle ( $\alpha_L$ ) and time for 46-66 keV electrons. Electrons that traveled towards the northern hemisphere had  $\alpha_L < 90^\circ$  and southern hemisphere had  $\alpha_L > 90^\circ$ . The interval between the two vertical dashed black lines contain the four microbursts examined in this study. We observed these microbursts at  $\alpha_L < 50^\circ$ , but MagEIS-A did not sample into the  $0^\circ$  loss cone.

Figure 4.1 panel (c) shows the EMFISIS WFR data from RBSP-A. Between 11:17:05 and 11:17:10 UT, we observed an isolated burst of whistler mode wave power in the frequency range  $0.1 < \omega < 0.3 \Omega_{ce0}$ , where  $\Omega_{ce0}$  is the equatorial electron gyrofrequency. No individual rising or falling tone elements were observed during this period, and the waves appeared more “hiss-like” (e.g. Li et al., 2012). This wave was near-parallel propagating (evidence shown in Appendix A) and about 10 minutes later, weak chorus rising tone elements were observed (not shown).

Panels (d)-(f) in Fig. 4.1 are in the same format as panels (a)-(c), but for RBSP-B. An injection or boundary was observed with RBSP-B at 11:16:50 UT and RBSP-A observed a similar feature soon after 11:18 UT (not shown).

A zoomed-in version of Fig. 4.1 panels (a) and (b) is shown in Fig. 4.2. Panel (a) shows the four microburst-like signatures observed between 11:17:10 and 11:17:12 UT, at energies up to 92 keV. The observed duration of the microbursts was 150 - 500 ms, and they did not arrive dispersed in energy, which indicates that they were recently scattered near the spacecraft location. We use IRBEM-Lib, a library dedicated to radiation belt modeling (Boscher et al., 2012), to calculate the mirror point altitudes, which were found to be above LEO. Panel (b) shows the RBSPICE-A EBR time series with the group of microbursts observed at the same time as in panel (a). To understand the timing relationship between the MagEIS-A and

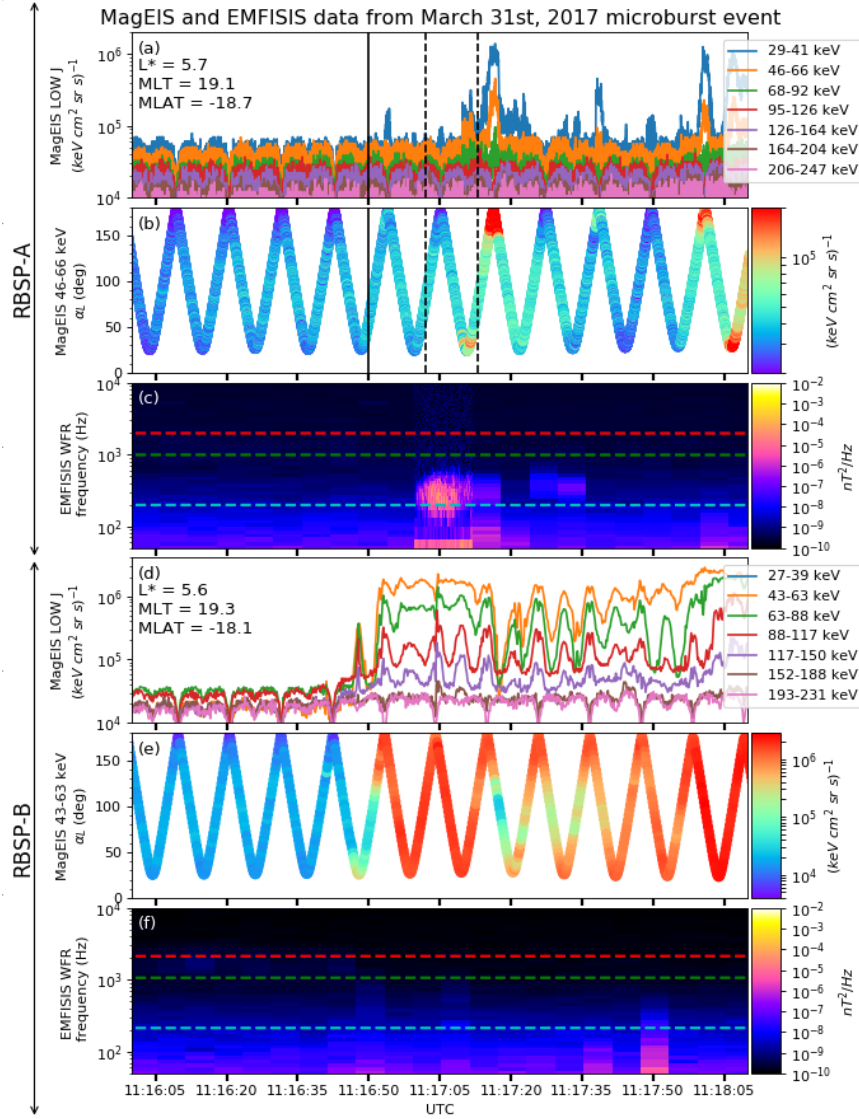


Figure 2.1: Electron and wave conditions from the MagEIS-A and EMFISIS WFR sensors for the microburst time interval. Panels (a), (b), and (c) are from RBSP-A with its position information annotated in panel (a). Panels (d), (e), and (f) are from RBSP-B with its position information annotated in panel (d). Panel (a) is the MagEIS-A high rate timeseries. Panels (b) and (e) show the evolution of the MagEIS-A  $J$  as a function of  $\alpha_L$  from the  $\sim 40$  to  $\sim 60$  keV channel. Every 10th point is shown in panel (b). The solid black line in panels (a) and (b) mark the end of the time period used for the PSD fit extrapolation analysis explained in section 3. The dashed black lines in panels (a) and (b) show the time interval used for the observed microburst PSD. Panels (c) and (f) show the EMFISIS WFR spectra, with the available burst data superposed. The red, green, and cyan traces are equatorial  $f_{ce0}$ ,  $f_{ce0}/2$ , and  $f_{ce0}/10$ , respectively.

RBSPICE-A observations, we marked the times when MagEIS-A observed the four microbursts by vertical black arrows in panels (a) and (b). MagEIS-A observed the first microburst  $\sim 0.5$  s before RBSPICE-A. The bounce period of locally mirroring, 100 keV electrons was  $\sim 0.8$  s, so this was unlikely to have been a returning bounce. This evidence confirms that these microburst signatures are packets of electrons and not a boundary moving back and forth at RBSP-A's location. To understand the PA extent of these microbursts, panel (c) shows the 29-41 keV MagEIS-A  $J$  and RBSPICE-A EBR as a function of  $\alpha_L$  and time. The microburst  $J$  was observed by MagEIS-A between  $25^\circ < \alpha_L < 50^\circ$  and RBSPICE-A between  $100^\circ < \alpha_L < 160^\circ$ , with the highest intensities close to  $\alpha_L = 90^\circ$ . RBSPICE-A observed a 10-80% enhancement in count rate over those PAs with the evidence presented in Appendix A.

### Analysis

First, we estimated the microburst energy spectra. For each microburst shown in Fig. 4.2, its flux was averaged and baseline subtracted using the method from O'Brien et al. (2004) and then fit with an exponential function. The calculated exponential E-folding energy was found to vary between 25 and 35 keV, which is consistent with spectra derived from prior measurements (Datta et al., 1997; Lee et al., 2012, 2005).

We then tested the hypothesis that the microburst electrons were transported in energy and PA by a single chorus wave. We used a procedure similar to sections 3.1 and 4.5 in Meredith et al. (2002) which we describe below.

### Microburst and Source PSD

We estimated the electron PSD,  $f(p_\perp, p_\parallel)$  where  $p_\perp$  and  $p_\parallel$  are the perpendicular and parallel components of the electron momentum relative to the local magnetic field,

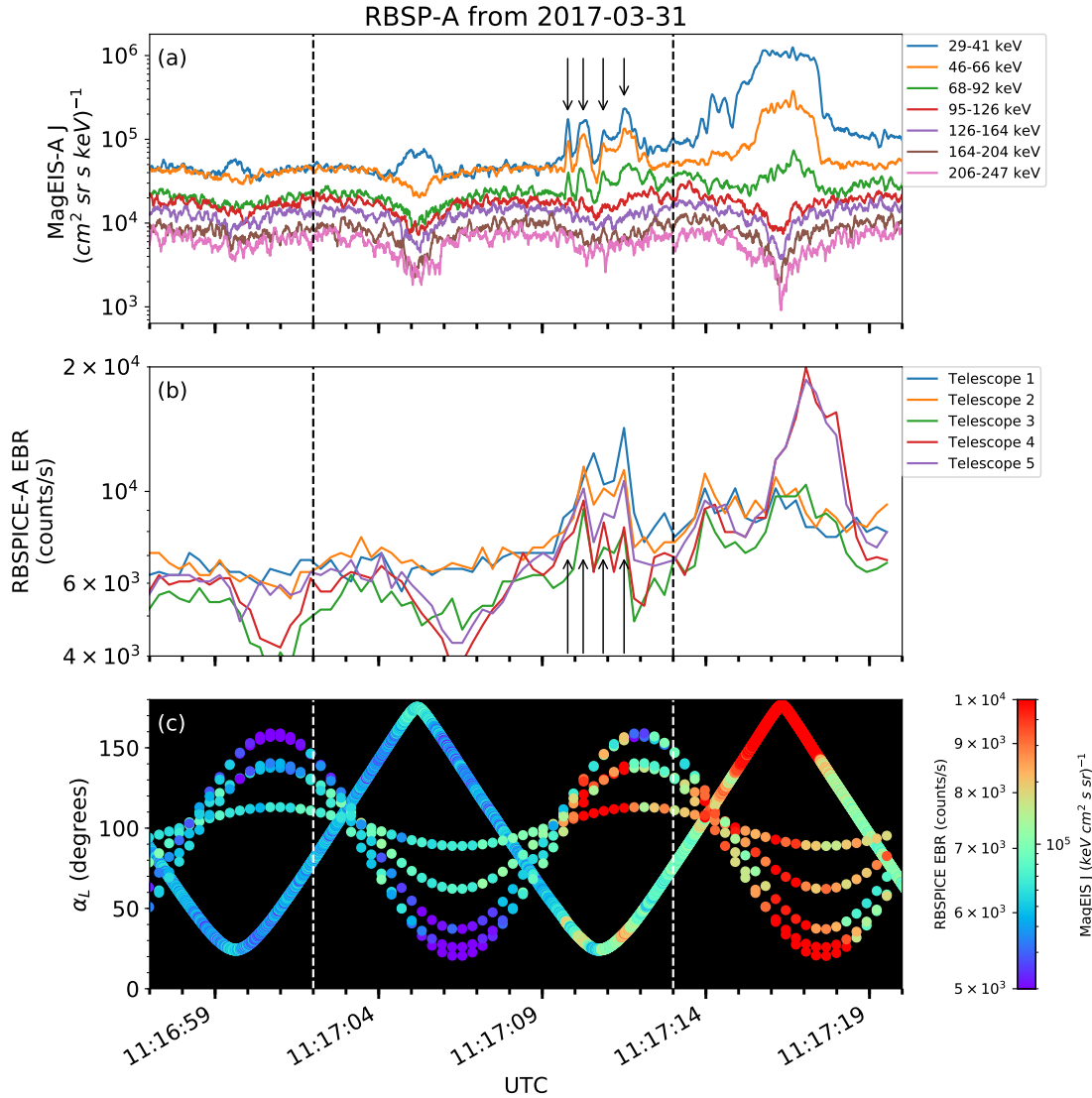


Figure 2.2: Panel (a) shows the MagEIS-A high rate timeseries. Panel (b) shows the RBSPIKE EBR count rate timeseries for > 19 keV electrons. The microbursts were observed between 11:17:10 - 11:17:12 UT and are indicated with the vertical black arrows in panels (a) and (b) for MagEIS-A times. Panel (c) shows the RBSPIKE EBR (family of relatively sparse sampled curves) and MagEIS-A  $J$  from the 29-41 keV energy channel (single curve) as a function of  $\alpha_L$ . The vertical dashed lines show the time interval for the PSD analysis.

for the microburst time period. MagEIS-A  $J(E, \alpha_L)$  was averaged between 11:17:02 and 11:17:13 UT and binned by  $\alpha_L$  into  $5^\circ$  bins. Then, we assumed the conservation of the first adiabatic invariant and mapped  $\alpha_L$  to equatorial PA,  $\alpha_{eq}$ . The binned  $J(E, \alpha_{eq})$  was then converted to  $f(p_\perp, p_\parallel)$  via

$$f(p_\perp, p_\parallel) = \frac{J(E, \alpha_{eq})}{p^2}, \quad (2.1)$$

where  $p = \sqrt{p_\perp^2 + p_\parallel^2}$ . Lastly,  $\alpha_{eq}$  was used to separate  $p$  into  $p_\perp$  and  $p_\parallel$  via

$$\frac{p_\parallel}{m_e c} = \frac{\sqrt{E(E + 2E_0)} \cos(\alpha_{eq})}{E_0} \quad (2.2)$$

$$\frac{p_\perp}{m_e c} = \frac{\sqrt{E(E + 2E_0)} \sin(\alpha_{eq})}{E_0} \quad (2.3)$$

where  $c$  is the speed of light,  $E$  is the kinetic energy,  $m_e$  is the electron mass, and  $E_0$  is the electron rest energy. The observed  $f(p_\perp, p_\parallel)$  in dimensionless momentum space is shown in Fig. 4.3 in all panels between the  $p_\parallel$  axis and the white dotted lines. The bright spot in  $f(p_\perp, p_\parallel)$  in the upper  $p_\parallel$  plane represents the four microbursts. Along with the observed PSD, we use Fig. 4.3 to explore the various PSD extrapolation and diffusion model assumptions which are described below.

We proceed under the assumption that the source of the microburst electrons is not likely to be at the latitude of the observation, and is closer to the magnetic equator. To look for a source of microburst electrons, we extrapolate the unobserved  $f(p_\perp, p_\parallel)$  of electrons with  $|\lambda_m| < 19^\circ$  using two cases with a  $90^\circ$ -peaked PAD of the form

$$f(E, \alpha_{eq}) = f_0(E) \sin^n(\alpha_{eq}) \quad (2.4)$$

where  $f_0(E)$  is a scaling parameter and  $n$  is a power parameter. Similarly to the

in-situ  $f(p_{\perp}, p_{\parallel})$ , the  $f(E, \alpha_{eq}) \mapsto f(p_{\perp}, p_{\parallel})$  conversion was applied.

In the first case, we fitted Eq. 2.4 to the quiet time  $J(E, \alpha_{eq})$  from 11:15:00 to 11:16:50 UT (end time shown as the black vertical line in Fig. 4.1). The fitted PAD was relatively flat with  $0.4 < n < 0.5$  and highest magnitude of  $f_0$  was  $0.05 \text{ cm}^3/(\text{cm MeV})^3$ . This extrapolated  $f(p_{\perp}, p_{\parallel})$  is shown in Fig. 4.3 panels (A) and (E), between the dotted white lines for scattering at  $\lambda = 0^\circ$  and  $20^\circ$ , respectively. To confirm the relatively low  $n$  parameter, we found times where RBSP-A was in a similar L-MLT location, but closer to the magnetic equator. At 2 and 19 UT on the same day, we fit the  $J(E, \alpha_{eq})$ , and the fit parameters were very similar to the pre-microburst  $f(p_{\perp}, p_{\parallel})$  at 11 UT. Thus it is a reasonable assumption that  $f(p_{\perp}, p_{\parallel})$  was relatively flat near the equator.

In the other case, we estimate how large  $n$  would have to be in order to find sufficient PSD in MagEIS-A's energy range to be a source of the microburst electrons. We used  $n \in \{1, 2, 4\}$  and we forced the  $f_0(E)$  parameter to match the observed  $f(p_{\perp}, p_{\parallel})$  at the most equatorial PAs observed by MagEIS-A. These extrapolations are shown in columns 2-4 in Fig. 4.3. There was enough source PSD anywhere in MagEIS-A's energy range only if  $n \geq 2$ .

#### Motion of resonant electrons in phase space

To calculate the motion of resonant electrons in momentum space, we used the relativistic theory of wave-particle resonant diffusion developed by Walker (1993) and Summers et al. (1998) and applied in Meredith et al. (2002). The chorus wave can modify  $f(p_{\perp}, p_{\parallel})$  when a resonance condition is satisfied. The cyclotron resonance condition between an electron with velocity  $v = \sqrt{v_{\parallel}^2 + v_{\perp}^2}$  and a parallel propagating

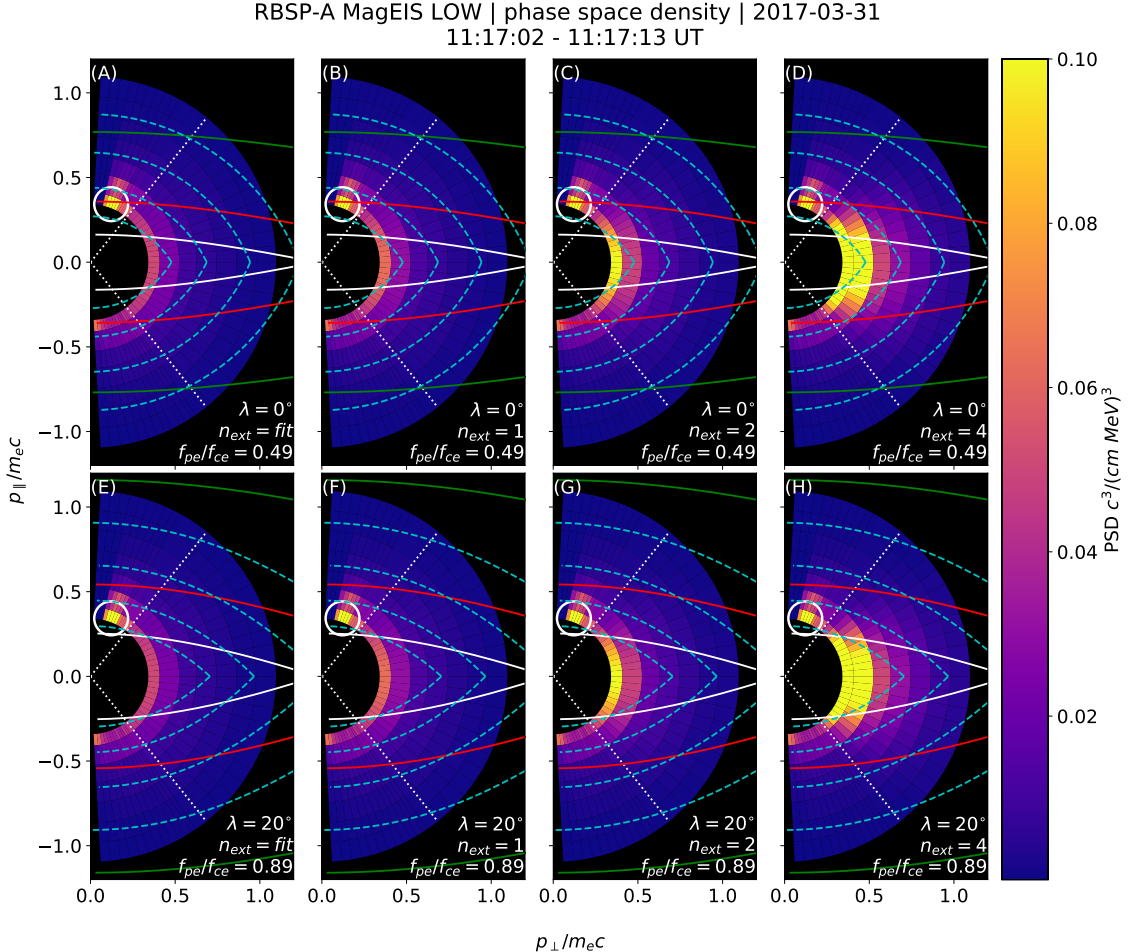


Figure 2.3: The colored annulus represents  $f(p_{\perp}, p_{\parallel})$  in normalized momentum space, parallel and perpendicular to the background magnetic field. The microburst  $f(p_{\perp}, p_{\parallel})$  is highlighted with the white circle. The columns show different powers of the sine extrapolation, and rows show the different magnetic latitudes of the scattering. The white dotted traces represent the boundary between the data and extrapolation. The green, red, and white solid traces are the resonance curves for  $\omega = 0.2\Omega_{ce}$ ,  $0.4\Omega_{ce}$ ,  $0.6\Omega_{ce}$ , respectively. The cyan dashed traces are the diffusion curves for a  $\omega = 0.4\Omega_{ce}$  wave (waves of other frequency have similar diffusion curves). The magnetic latitude of the scattering, the ratio of the plasma to the cyclotron frequency, and the power of the sine extrapolation is annotated in each panel. For the resonance and diffusion curves, the density model assumed a  $n_L = 1 e^-/cm^3$  and  $\psi = -1$ .

wave of frequency  $\omega$  and wave number  $k_{\parallel}$  is given by

$$\omega - v_{\parallel} k_{\parallel} = \frac{\Omega_{ce}}{\gamma}, \quad (2.5)$$

where  $\Omega_{ce}$  is the electron gyrofrequency at the scattering location, and  $\gamma$  is the relativistic correction. Assuming the cold plasma approximation,

$$k_{\parallel} = \frac{\omega}{c} \sqrt{1 - \frac{\omega_{pe}^2}{\omega(\omega - |\Omega_{ce}|)}}, \quad (2.6)$$

where  $\omega_{pe}$  is the plasma frequency. For a particular set of parameters, Eq. 2.5 defines a curve in momentum space that describes which electrons will resonate with a monochromatic wave.

To calculate  $k_{\parallel}$ , we approximated the electron number density,  $n_e(\lambda)$  locally and at the magnetic equator. Locally, the plasma density was approximately  $n_e(\lambda = -20^\circ) = n_L \approx 1 \text{ cm}^{-3}$ . We used magnetospheric seismology techniques (e.g. Takahashi and Denton, 2007) to parameterize  $n_e(\lambda)$  elsewhere along the field line with

$$n_e(\lambda) = n_e(0) \left( \frac{LR_e}{R(\lambda)} \right)^{\psi} \quad (2.7)$$

where  $R_e$  is the Earth's radius,  $R(\lambda)$  is the radial distance from the Earth to the spacecraft, and  $\psi$  is the exponent parameter. Assuming a dipole magnetic field for which  $R(\lambda) = LR_e \cos^2 \lambda$  (e.g. Schulz and Lanzerotti, 1974), we can express Eq. 2.7 in terms of  $n_L$  via

$$n_e(\lambda) = n_L \left( \frac{\cos \lambda_L}{\cos \lambda} \right)^{2\psi} \quad (2.8)$$

where we used  $\psi = -1$  (higher density at the magnetic equator) in this analysis. We chose this exponent parameter because it is a realistic best case scenario for the

electrons to be transported along the diffusion curves (described below).

Walker (1993) and Summers et al. (1998) argued that a resonant electron will move along diffusion curves in momentum space. A diffusion curve is derived as follows. In the reference frame moving with a monochromatic chorus wave's phase velocity (wave frame), the chorus wave is stationary and there is no electric field. Thus in the wave frame, the electron's kinetic energy is conserved, and the electron's velocity in the wave frame can be expressed in differential form as

$$v_{\parallel}dv_{\parallel} + v_{\perp}dv_{\perp} = 0. \quad (2.9)$$

After a Lorentz transformation of Eq. 2.9 into the magnetospheric frame, kinetic energy will no longer be conserved. After integration and manipulation of Eq. 2.9, we obtain:

$$\left(1 - \frac{u_0^2 v_0^2}{c^4}\right)v_{\parallel}^2 - 2u_0\left(1 - \frac{v_0^2}{c^2}\right)v_{\parallel} + \left(1 - \frac{u_0^2}{c^2}\right)v_{\perp}^2 = v_0^2 - u_0^2 \quad (2.10)$$

where  $u_0 = \omega/k_{\parallel}$  is the phase velocity, and  $v_0$  is a constant of integration (Summers et al., 1998; Walker, 1993). Equation 2.10 defines a family of diffusion curves in momentum space on which resonant electrons will move. The distance that an electron moves along a diffusion curve is a function of wave and plasma parameters, and is estimated from the magnitude of the diffusion coefficients and the resonance time.

#### Comparing the microburst PSD to diffusion theory

Superposed on the PSD plots in Fig. 4.3 are resonance curves for chorus waves of  $\omega = 0.2\Omega_{ce}$ ,  $0.4\Omega_{ce}$ ,  $0.6\Omega_{ce}$  and a few diffusion curves for a  $\omega = 0.4\Omega_{ce}$  wave. These curves were parameterized by  $\lambda$  using a dipole magnetic field for  $\lambda = 0^\circ$

(Fig. 4.3, panels A-D) and  $\lambda = 20^\circ$  (Fig. 4.3, panels E-H). If the transport of microburst electrons is consistent with gyro-resonant diffusion, a diffusion curve that passes through the microburst  $f(p_\perp, p_\parallel)$  must also pass through another region with at least the same magnitude PSD ( $f(p_\perp, p_\parallel) \geq 0.1 \text{ c}^3/(\text{cm MeV})^3$ ) e.g. Fig. 4.3, panel (D). With this constraint, an artificially high extrapolated  $f(p_\perp, p_\parallel)$  with  $n > 2$  (5 times larger than calculated from the fits) must be assumed for there to have been a sufficient source of PSD anywhere in MagEIS-A's energy range.

We now show that by comparing MagEIS observations with theory, that the minimum wave amplitude necessary to scatter these electrons is much higher than was observed by EMFISIS-A. If we assume a unrealistic PAD with enough PSD just equatorward of RBSP-A, we can use MagEIS-A observations to calculate the minimum  $\Delta\alpha_{eq}$  that the electrons were transported. We then used diffusion theory to calculate the necessary wave amplitude. For microbursts with larger PAs, MagEIS-A observed a transport of  $\Delta\alpha_{eq} = 9^\circ$  and for microbursts with smaller PAs, the observed transport was  $\Delta\alpha_{eq} = 24^\circ$ . The required wave amplitude was calculated with Eq. 3 from Thorne and Andreoli (1981) assuming a maximum resonance period of a quarter bounce. The observed change in PA requires a wave amplitude  $0.2 < |B_w| < 0.5 \text{ nT}$ . For a few brief moments, the EMFISIS-A WFR waveform data showed  $0.1 < |B_w| < 0.15 \text{ nT}$ , so a transport of  $9^\circ$  is plausible, but not likely for  $24^\circ$ .

Another source of microburst electrons may be from energies below MagEIS-A's range. The Helium, Oxygen, Proton, and Electron mass spectrometer (Funsten et al., 2013) on RBSP-A observed  $f(p_\perp, p_\parallel) \geq 0.1 \text{ c}^3/(\text{cm MeV})^3$  for  $\gtrsim 23 \text{ keV}$  electrons at this time. We then assumed the wave amplitude derived above to predict the transport in energy. We used the fact that the momentum and pitch angle diffusion coefficients,  $D_{pp}$  and  $D_{\alpha\alpha}$  are related via  $D_{pp}/p^2 \sim D_{\alpha\alpha}$  or equivalently,  $\Delta p/p \sim \Delta\alpha$ . The observed PA transport corresponds to an energy transport of  $6 < \Delta E < 16$

keV. Therefore, this wave can transport 23 keV electrons from smaller pitch angles to larger pitch angles and would be observed in the 29 – 41 keV MagEIS-A channel. However, this wave is insufficient to transport electrons to the 68 – 92 keV channel in one interaction. Therefore we conclude that quasi-linear diffusion cannot explain the observed microbursts.

### Discussion and Conclusions

These novel observations of impulsive electron signatures reported here fall well within the broad definition of a microburst as described in section 3. Their properties were similar to microbursts observed in LEO, with an E-folding energy of  $25 < E_0 < 35$  keV (Datta et al., 1997; Lee et al., 2012, 2005), duration of 150-500 ms (Lorentzen et al., 2001a), observed upper energy limit of 92 keV, and a lack of clear energy dispersion (Breneman et al., 2017). With MagEIS-A’s high time and energy resolution, we conclude that these dispersionless microbursts were recently scattered near the spacecraft. Furthermore, RBSPICE-A’s PA coverage suggests that these electrons were scattered over a substantial range of PAs, with the highest intensities near  $\alpha_L = 90^\circ$ . Overall, our observational evidence suggests that on time scales shorter than one bounce period, the chorus wave effectively accelerated trapped electrons over a broad PA range.

In the theoretical framework of wave-particle resonant diffusion applied to the observed PSD in section 3, we determine that the observed scattering is not consistent with the quasi-linear approximation. The nearest source of sufficient PSD is too far away in phase space to have been transported by the hypothesized quasi-linear process over a timescale shorter than one bounce period (one interaction). A similar conclusion was made by Mozer et al. (2018) who used quasi-linear theory constrained by RBSP wave measurements. They successfully modeled the one second average

precipitating flux observed with AeroCube-6 (AC-6) CubeSats during a conjunction, but they were unable to model the AC-6 fluxes on smaller time scales.

To put these microburst observations into a wider magnetospheric perspective, we observed them during the recovery phase of a minimum Dst of -75 nT storm, a statistically favorable time period for microbursts (O'Brien et al., 2003). Furthermore, during the same storm on March 27th, the Arase spacecraft observed highly correlated lower band chorus with 10-50 keV electron precipitation inside the loss cone. At that time, Arase's magnetic field footprint was near The Pas All-Sky Imager (part of the THEMIS mission) which simultaneously observed pulsating auroral patches (Kasahara et al., 2018). While microbursts and pulsating auroral patches have not been clearly connected, they are both believed to be a product of electron scattering by whistler mode waves (e.g. Lorentzen et al., 2001a; Nishimura et al., 2011; O'Brien et al., 2003; Ozaki et al., 2012).

The combined capabilities of the various RBSP wave and particle instruments enable comprehensive studies of wave-particle scattering and the resulting microburst precipitation. From a preliminary search by the authors, other microburst-like signatures have been found with RBSP. Similar to previous studies (e.g. Blum et al., 2015; O'Brien et al., 2003), a statistical study of high-altitude microbursts in L-MLT space needs to be conducted before we can verify that these microbursts are the counterpart of the microbursts observed in LEO and the upper atmosphere.

### Acknowledgments

The authors acknowledge the technicians, engineers, and scientists who made the RBSP and AC-6 missions possible. One author (Shumko) would like to acknowledge Dana Longcope for his help in understanding the quasi-linear diffusion theory. Dr. Gkioulidou was supported by JHU/APL subcontract 131803 to the NJIT under NASA

Prime contract NNN06AA01C. EMFISIS work was supported by JHU/APL contract no. 921647 under NASA Prime contract No. NAS5-01072. The MagEIS instrument was funded by NASA's Prime contract no. NAS5-01072. The level 3 MagEIS-A "high rate" data is available in the Supporting Information, level 1 RBSPICE EBR data is archived at <http://rbspicea.ftecs.com/>, and the EMFISIS level 2 spectral matrix and burst data as well as the level 3 magnetometer data is archived at <http://emfisis.physics.uiowa.edu/data/index>. The IRBEM Library can be obtained at [rbem.sf.net](http://rbem.sf.net).

MICROBURST SCALE SIZE DERIVED FROM MULTIPLE BOUNCES OF A  
MICROBURST SIMULTANEOUSLY OBSERVED WITH THE FIREBIRD-II  
CUBESATS

Contribution of Authors and Co-Authors

Manuscript in Chapter 1

Author: Mykhaylo Shumko

Contributions: Found bouncing packet microburst and analyzed its size and bounce period.

Co-Author: John Sample

Contributions: Provided advise and ideas.

Co-Author: Arlo Johnson

Contributions: Helped estimate the time corrections necessary for this analysis.

Co-Author: Bern Blake

Contributions: Provided advise and ideas.

Co-Author: Alex Crew

Contributions: Requested data and built the FIREBIRD-II CubeSats.

Co-Author: Harlan Spence

Contributions: FIREBIRD-II principal investigator.

Co-Author: Kavid Klumpar

Contributions: FIREBIRD-II principal investigator.

Co-Author: Oleksiy Agapitov

Contributions: Provided guidance to calculate the microburst bounce period.

Co-Author: Matthew Handley

Contributions: Downloaded data and built the FIREBIRD-II CubeSats.

Manuscript Information

Mykhaylo Shumko, John Sample, Arlo Johnson, Bern Blake, Alex Crew, Harlan Spence, David Klumpar, Oleksiy Agapitov, and Matthew Handley

Status of Manuscript:

- Prepared for submission to a peer-reviewed journal
- Officially submitted to a peer-reviewed journal
- Accepted by a peer-reviewed journal
- Published in a peer-reviewed journal

Geophysical Research Letters Volume 45, Issue 17

DOI: 10.1029/2018GL078925

This article is available under the terms of the Creative Commons Attribution Non-Commercial No Derivatives License CC BY-NC-ND (which may be updated from time to time) and permits non-commercial use, distribution, and reproduction in any medium, without alteration, provided the original work is properly cited and it is reproduced verbatim.

Key Points

- Multiple bounces from a microburst were observed by the two FIREBIRD-II CubeSats at LEO.
- The lower bounds on the microburst scale size at LEO were  $29 \pm 1$  km (latitudinal) and  $51 \pm 11$  km (longitudinal).
- Deduced lower bound equatorial scale size was similar to the whistler-mode chorus source scale.

Abstract

We present the observation of a spatially large microburst with multiple bounces made simultaneously by the FIREBIRD-II CubeSats on February 2nd, 2015. This is the first observation of a microburst with a subsequent decay made by two co-orbiting but spatially separated spacecraft. From these unique measurements, we place estimates on the lower bounds of the spatial scales as well as quantify the electron bounce periods. The microburst's lower bound latitudinal scale size was  $29 \pm 1$  km and the longitudinal scale size was  $51 \pm 1$  km in low earth orbit. We mapped these scale sizes to the magnetic equator and found that the radial and azimuthal scale sizes were at least  $500 \pm 10$  km and  $530 \pm 10$  km, respectively. These lower bound equatorial scale sizes are similar to whistler-mode chorus wave source scale sizes, which supports the hypothesis that microbursts are a product of electron scattering by chorus waves. Lastly, we estimated the bounce periods for 200-800 keV electrons and found good agreement with four common magnetic field models.

## Introduction

The dynamics of radiation belt electrons are complex, and are driven by competition between source and loss processes. A few possible loss processes are radial diffusion (Shprits and Thorne, 2004), magnetopause shadowing (Ukhorskiy et al., 2006), and pitch angle and energy diffusion due to scattering of electrons by plasma waves (e.g. Abel and Thorne, 1998; Horne and Thorne, 2003; Meredith et al., 2002; Mozer et al., 2018; Selesnick et al., 2003; Summers et al., 1998; Thorne et al., 2005). There are a variety of waves that cause pitch angle scattering, including electromagnetic ion cyclotron waves, plasmaspheric hiss, and chorus (Millan and Thorne, 2007; Thorne, 2010). Chorus predominantly occurs in the dawn sector (6-12 magnetic local times (MLT)) (Li et al., 2009b) where it accelerates electrons with large equatorial pitch angles and scatters electrons with small equatorial pitch angles (Horne and Thorne, 2003). Some of these electrons may be impulsively scattered into the loss cone, where they result in short-duration ( $\sim 100$  ms) enhancements in precipitating flux called microbursts.

Anderson and Milton (1964) coined the term microburst to describe high altitude balloon observations of  $\sim 100$  ms duration enhancements of bremsstrahlung X-rays emitted from scattered microburst electrons impacting the atmosphere. Since then, non-relativistic (less than a few hundred keV) microbursts have been routinely observed with other balloon missions (e.g. Anderson et al., 2017; Parks, 1967; Woodger et al., 2015). A review of the literature shows no reports of microbursts above a few hundred keV observed by balloons (Millan et al., 2002; Woodger et al., 2015). This lack of observation may be explained by relatively weaker pitch angle scattering of relativistic electrons by chorus (Lee et al., 2012).

In addition to the X-ray signature for bursts of electron precipitation, the

precipitating relativistic and non-relativistic electrons have been measured in situ by spacecraft orbiting in low earth orbit (LEO). Hereinafter, we refer to these electron signatures observed by LEO spacecraft also as microbursts. Microbursts have been observed with, e.g. the Solar Anomalous and Magnetospheric Particle Explorer's (SAMPEX)  $\gtrsim 150$  keV and  $\gtrsim 1$  MeV channels (Blake et al., 1996; Blum et al., 2015; Lorentzen et al., 2001a,b; Nakamura et al., 1995, 2000; O'Brien et al., 2004, 2003) and Focused Investigation of Relativistic Electron Bursts: Intensity, Range, and Dynamics (FIREBIRD-II) with its  $\gtrsim 200$  keV energy channels (Anderson et al., 2017; Breneman et al., 2017; Crew et al., 2016).

Understanding microburst precipitation and its scattering mechanism is important to radiation belt dynamics. The scattering mechanism has been observationally studied by e.g. Lorentzen et al. (2001b) who found that microbursts and chorus waves predominantly occur in the dawn sector and Breneman et al. (2017) made a direct observational link between individual microbursts and chorus elements. Microbursts have been modeled and empirically estimated to be capable of depleting the relativistic electron population in the outer radiation belt on the order of a day (Breneman et al., 2017; O'Brien et al., 2004; Shprits et al., 2007; Thorne et al., 2005). An important parameter in this estimation of instantaneous radiation belt electron losses due to microbursts is their scale size. Parks (1967) used balloon measurements of bremsstrahlung X-rays to estimate the high altitude scale size of predominantly low energy microbursts to be  $40 \pm 14$  km. In Blake et al. (1996) a microburst with multiple bounces was observed by SAMPEX, and the microburst's latitudinal scale size in LEO was estimated to have been “at least a few tens of kilometers”. Blake et al. (1996) concluded that typically microbursts are less than a few tens of electron gyroradii in size (at  $L = 5$  at LEO, the gyroradii of 1 MeV electrons is on the order of 100 m). Dietrich et al. (2010) used SAMPEX along with ground-based very low frequency

stations to conclude that during one SAMPEX pass, the observed microbursts had scale sizes less than 4 km.

Since February 1st, 2015, microbursts have been observed by FIREBIRD-II, a pair of CubeSats in LEO. Soon after launch, when the two FIREBIRD-II spacecraft were at close range, a microburst with a scale size greater than 11 km was observed (Crew et al., 2016). On the same day, FIREBIRD-II simultaneously observed a microburst with multiple bounces. The microburst decay was observed over a period of a few seconds, while the spacecraft were traveling predominantly in latitude. Here we present the analysis and results of the latitude and longitude scale sizes and bounce periods of the first microburst with multiple bounces observed with the two FIREBIRD-II spacecraft.

### Spacecraft and Observation

The FIREBIRD missions are comprised of a pair of identically-instrumented 1.5U CubeSats (15 x 10 x 10 cm) that are designed to measure electron precipitation in LEO (Klumpar et al., 2015; Spence et al., 2012). The second mission, termed FIREBIRD-II, was launched on January 31st 2015. The two FIREBIRD-II CubeSats, identified as Flight Unit 3 (FU3) and Flight Unit 4 (FU4), were placed in a 632 km apogee, 433 km perigee, and 99° inclination orbit (Crew et al., 2016). FU3 and FU4 are orbiting in a string of pearls configuration with FU4 ahead, to resolve the space-time ambiguity of microbursts. Each FIREBIRD-II unit has two solid state detectors: one is mounted essentially at the spacecraft surface, covered only by a thin foil acting as a sun shade, with a field of view of 90° (surface detector), and the other is beneath a collimator which restricts the field of view to 54° (collimated detector). Only FU3 has a functioning surface detector, so this analysis utilizes the collimated detectors. FU3's surface and collimated detectors, as well as FU4's collimated detector observe

electron fluxes in six energy channels from  $\sim 230$  keV to  $> 1$  MeV. FIREBIRD-II's High Resolution (HiRes) electron flux data is gathered with an adjustable sampling period of 18.75 ms by default and can be as fast as 12.5 ms.

On February 2nd, 2015 at 06:12 UT, both FIREBIRD-II spacecraft simultaneously observed an initial microburst, followed by subsequent periodic electron enhancements of diminishing amplitude shown in Fig. 3.1. This is thought to be the signature of a single burst of electrons, some of which precipitate, but the rest mirror near the spacecraft then bounce to the conjugate hemisphere where they mirror again and the subsequent bounces produce a train of decaying peaks (Blake et al., 1996; Thorne et al., 2005). This bounce signature occurred during the transition between the main and recovery phases of a storm with a minimum Dst of -44 nT ( $K_p = 4$ , and  $AE \approx 400$  nT). At this time, the HiRes data was sampled at 18.75 ms. Five peaks were observed by both spacecraft. The fifth peak observed by FU4 was comparable to the Poisson noise and was not used in this analysis. This microburst was observed from the first energy channel ( $\approx 200 - 300$  keV), to the fourth energy channel ( $\approx 500 - 700$  keV), and FU3's surface detector observed the microburst up to the fifth energy channel (683 - 950 keV).

The HiRes data in Fig. 3.1 shows signs of energy dispersion, characterized by higher energy electrons arriving earlier than the lower energies. This time of flight energy dispersion tends to smear out the initial sharp burst upon each subsequent bounce. The first peak does not appear to be dispersed, and subsequent peaks show a dispersion trend consistent across energy channels. The black vertical bars have been added to Fig. 3.1 to highlight this energy dispersion. This dispersion signature and amplitude decay implies that the first peak was observed soon after the electrons were scattered, followed by decaying bounces.

At this time, in magnetic coordinates, FIREBIRD-II was at McIlwain  $L = 4.7$

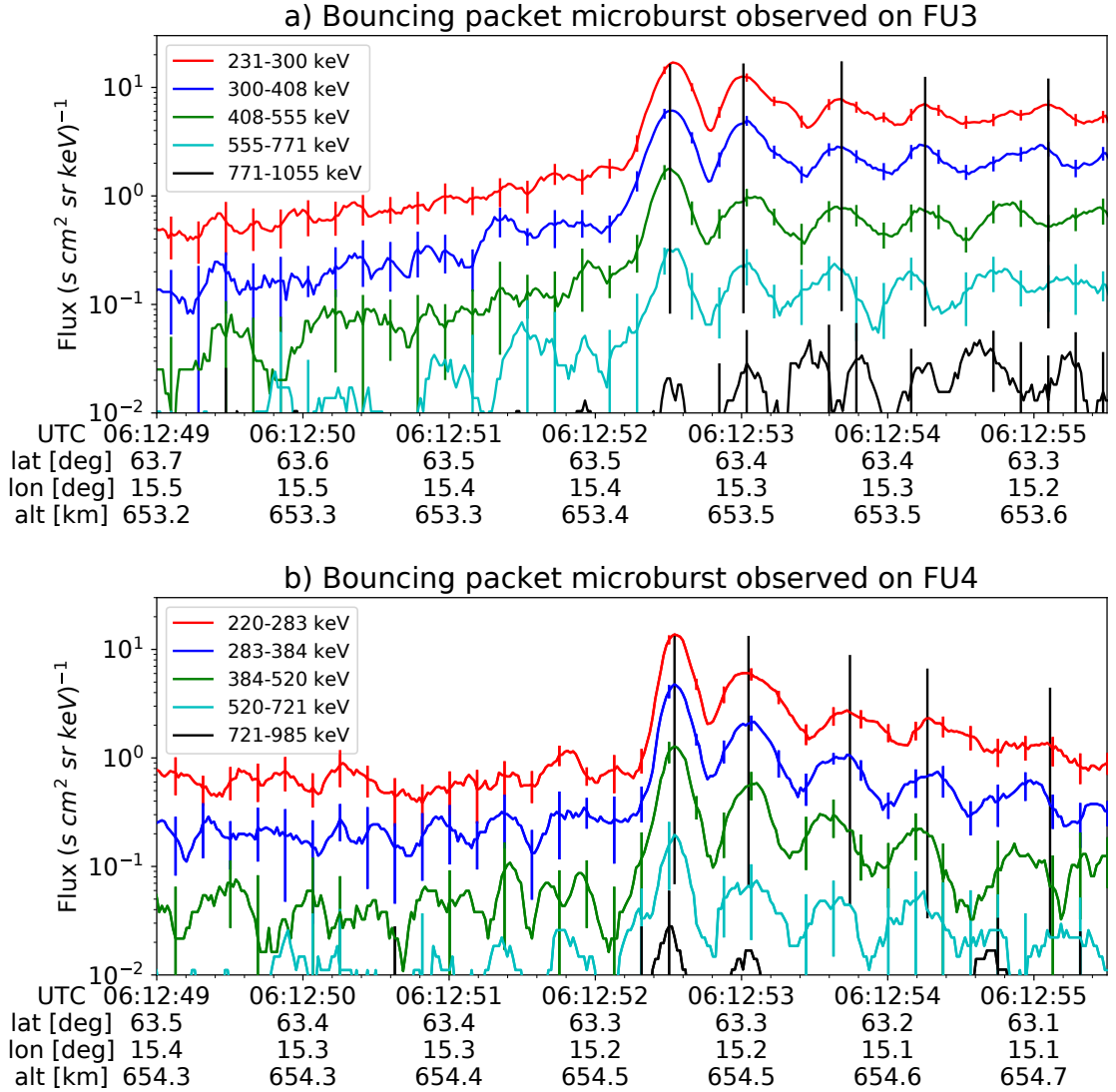


Figure 3.1: HiRes data of the microburst observed at February 2nd, 2015 at 06:12:53 UT, smoothed with a 150 ms rolling average. The subsequent bounces showed some energy dispersion. As discussed in Appendix B, a time correction of -2.28 s was applied to FU3. While the flux from five energy channels is shown, only channels with reasonable counting statistics were used for the spatial scale analysis. Vertical colored bars show the  $\sqrt{N}$  error every 10th data point and vertical black bars are lined up with the peaks in the 220-283 keV energy channel to help identify dispersion.

and MLT = 8.3, calculated with the Tsyganenko 1989 (T89) magnetic field model (Tsyganenko, 1989) using IRBEM-Lib (Boscher et al., 2012). Geographically, they were above Sweden, latitude = 63°N, longitude = 15°E, altitude = 650 km. This geographic location is magnetically conjugate to the east of the so-called South Atlantic Anomaly (SAA). The SAA is the location where the mirror points of electrons tend to occur at locations deeper in the atmosphere owing to the offset of the dipole magnetic field from the Earth's center. Electrons with pitch angles within the drift loss cone (DLC) will encounter the SAA and be removed from their eastward longitudinal drift paths (Comess et al., 2013; Dietrich et al., 2010). FU3 and FU4 are therefore both in regions where the particles in the DLC have recently precipitated, leaving only particles that were recently scattered. At the spacecraft location, locally mirroring electrons would have mirrored at 95 km in the opposite hemisphere, with more field aligned electrons mirroring at even lower altitudes. From the analysis done by Fang et al. (2010), the peak in the total ionization rate in the atmosphere for 100 keV electrons is around 80 km altitude, while the total ionization rate from 1 MeV electrons peaks around 60 km altitude. It is, therefore, expected that a fraction of the microburst electrons will survive each encounter with the atmosphere. By plotting the peak flux as a function of bounce (not shown), it was found that 40 - 60 % of the microburst electrons were lost on the first bounce, similar to the 33% loss per bounce observed for a bouncing microburst observed by SAMPEX (Thorne et al., 2005).

### Analysis

At the beginning of the FIREBIRD-II mission, two issues prevented the proper analysis of the microburst's spatial scale size: the spacecraft clocks were not synchronized, and their relative positions were not accurately known. We addressed these issues with a cross-correlation time lag analysis described in detail in Appendix

B. From this analysis, the time correction was  $2.28 \pm 0.12$  s (applied to Fig. 3.1) and the separation was  $19.9 \pm 0.9$  km at the time of the microburst observation.

### Electron Bounce Period

We used this unique observation of bouncing electrons to calculate the bounce period,  $t_b$  as a function of energy and compare it to the energy-dependent  $t_b$  curves derived from four magnetic field models, the results of which are shown in Fig. 3.2. The observed  $t_b$  and uncertainties were calculated by fitting the baseline-subtracted HiRes flux. The baseline flux used in this analysis is given in O'Brien et al. (2004) as the flux at the 10th percentile over a specified time interval, which in this analysis was taken to be 0.5 seconds. The flux was fitted with a superposition of Gaussians for each energy channel, and the uncertainty in flux was calculated using the Poisson error from the microburst and baseline fluxes summed in quadrature. Using the fit parameters, the mean  $t_b$  for the lowest four energy channels is shown in Fig. 3.2. The trend of decreasing  $t_b$  as a function of energy is evident in Fig. 3.2, which further supports the assumption that the subsequent peaks are bounces, and not a train of microbursts scattered by bouncing chorus.

The decaying peaks in the 231-408 keV electron flux observed by FU3's lowest two energy channels (see Fig. 3.1) were right-skewed. One explanation is that there was in-channel energy dispersion within those channels. Since  $t_b$  of higher energy electrons is shorter, a right-skewed peak implies that higher energy electrons were more abundant within that channel e.g. in FU3's 231-300 keV channel, the 300 keV electrons will arrive sooner than the 231 keV electrons, but will they will be binned in the same channel. A Gaussian fit cannot account for this in-channel dispersion, and as a first order correction, minima between peaks was used to calculate  $t_b$ , and is shown in Fig. 3.2. The observed energy-dependent dispersion shown in Fig. 3.2

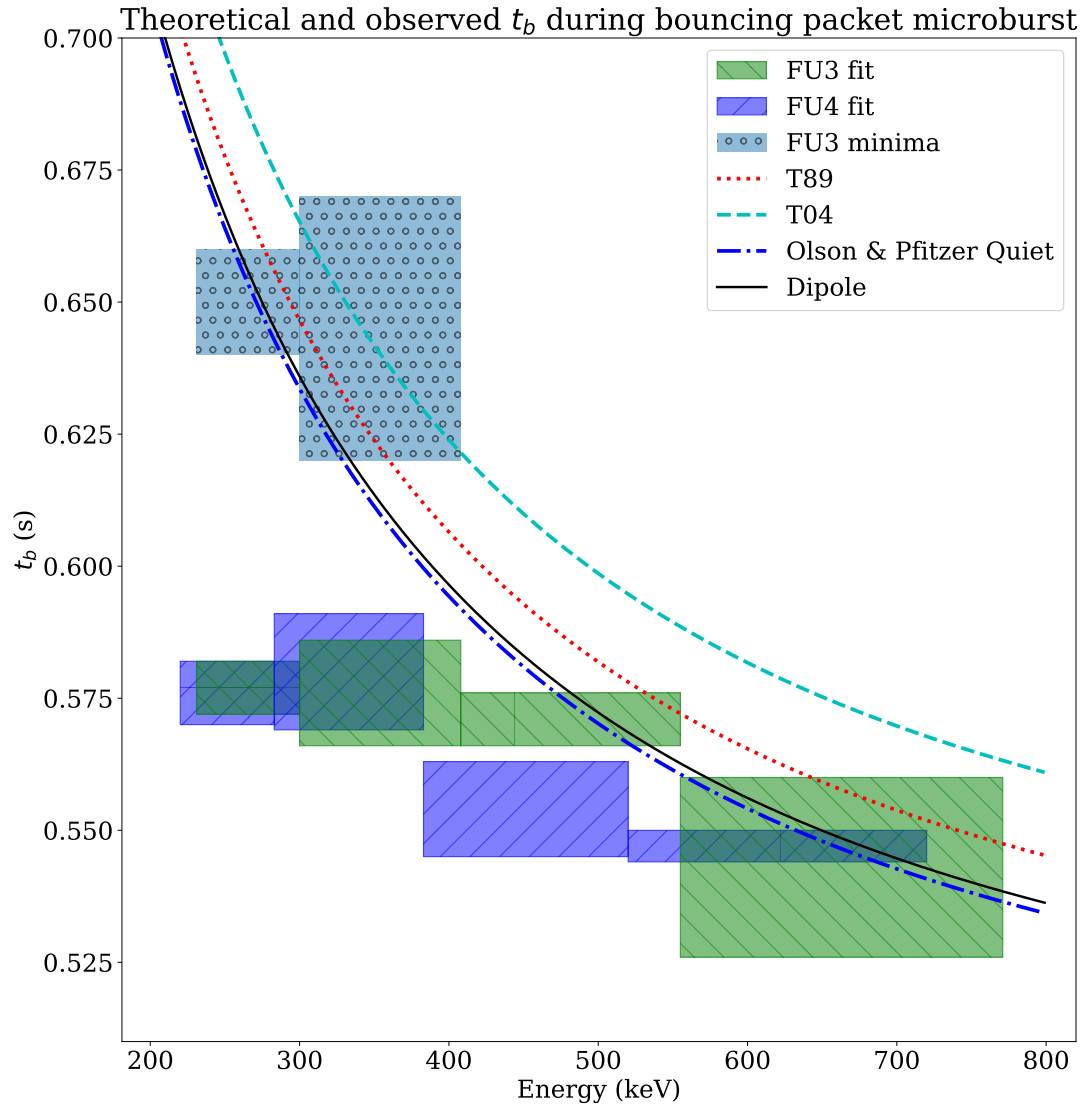


Figure 3.2: Observed and theoretical  $t_b$  for electrons of energies from 200 to 770 keV. The solid black line is  $t_b$  in a dipole magnetic field, derived in Schulz and Lanzerotti (1974). The red dotted and cyan dashed lines are the  $t_b$  derived using the T89, and T04 magnetic field models with IRBEM-Lib. Lastly, the blue dot-dash curve is the  $t_b$  derived using the Olson & Pfitzer Quiet model. The green and purple rectangles represent the observed  $t_b$  for FU3 and FU4 using a Gaussian fit, respectively. The blue rectangles represent the observed  $t_b$  calculated with the minima between the bounces. The width of the boxes represent the width of those energy channels, and the height represents the uncertainty from the fit.

is consistent with higher energy peaks returning sooner. This dispersion consistency further supports the assumption that the subsequent peaks are bounces, and not a train of microbursts scattered by bouncing chorus.

To compare the observed and modeled  $t_b$ , we superposed  $t_b$  curves for various models including an analytical solution in a dipole (Schulz and Lanzerotti, 1974), and numerical models: T89, Tsyganenko 2004 (T04) (Tsyganenko and Sitnov, 2005), and Olson & Pfitzer Quiet (Olson and Pfitzer, 1982) in Fig. 3.2. The numerical  $t_b$  curves were calculated using a wrapper for IRBEM-Lib. This code traces the magnetic field line between mirror points, and calculates  $t_b$  assuming conservation of energy and the first adiabatic invariant for electrons mirroring at FIREBIRD-II. With the empirical  $t_b$ , the models agree within FIREBIRD-II's uncertainties, but the T04 model has the largest discrepancy compared to the other models.

### Microburst Energy Spectra

Next, we investigated the energy spectra of this microburst. The energy spectra was modeled with an exponential that was fit to the peak flux derived from the Gaussian fit parameters in section 3 to all but the highest energy channel. We found that the E-folding energy,  $E_0 \sim 100$  keV. This spectra is similar to spectra show by Lee et al. (2005) from STSAT-1 and Datta et al. (1997) from sounding rocket measurements. The energy spectra is soft for a typical microburst observed with FIREBIRD-II and there was no statistically significant change in  $E_0$  for subsequent bounces.

### Microburst Scale Sizes

Lastly, after we applied the time and separation corrections detailed in Appendix B, we mapped the locations of FU3 and FU4 in Fig. 3.3. The locations where FU3 saw peaks 1-5 and where FU4 saw peaks 1-4 are shown as P1-5 and P1-4, respectively.

The lower bound on the latitudinal extent of the microburst was the difference in latitude between P1 on FU3 and P4 on FU4 and was found to be  $29 \pm 1$  km. The uncertainty was estimated from the spacecraft separation uncertainty described in Appendix B. This scale size is the largest reported by FIREBIRD-II.

In section 3, we showed that the observed decaying peaks were likely due to bouncing, so we assume that the observed electrons in subsequent bounces were the drifted electrons from the initial microburst. Under this assumption, the scattered electrons observed in the last bounce by FIREBIRD-II, must have drifted east from their initial scattering longitude, allowing us to calculate the minimum longitudinal scale size. Following geometrical arguments, the distance that electrons drift east in a single bounce is a product of the circumference of the drift shell foot print, and the fraction of the total drift orbit traversed in a single bounce and is given by,

$$d_{az} = 2\pi(R_E + A) \cos(\lambda) \frac{t_b}{\langle T_d \rangle} \quad (3.1)$$

where  $R_E$  is the Earth's radius,  $A$  is the spacecraft altitude,  $\lambda$  is the magnetic latitude,  $t_b$  is the electron bounce period, and  $\langle T_d \rangle$  is the electron drift period. Parks (2003) derived  $\langle T_d \rangle$  to be,

$$\langle T_d \rangle \approx \begin{cases} 43.8/(L \cdot E) & \text{if } \alpha_0 = 90^\circ \\ 62.7/(L \cdot E) & \text{if } \alpha_0 = 0^\circ \end{cases} \quad (3.2)$$

where  $E$  is the electron energy in MeV,  $L$  is the L shell, and  $\alpha_0$  is the equatorial pitch angle. Electrons mirroring at FIREBIRD-II have  $\alpha_0 \approx 3.7^\circ$  and so the  $\alpha_0 = 0^\circ$  limit was used.

The microburst's longitudinal scale size is defined as the distance the highest energy electrons drifted in the time between the observations of the first and last peaks. This scale size is given by  $D_{az} = n d_{az}$  where  $n$  is the number of bounces

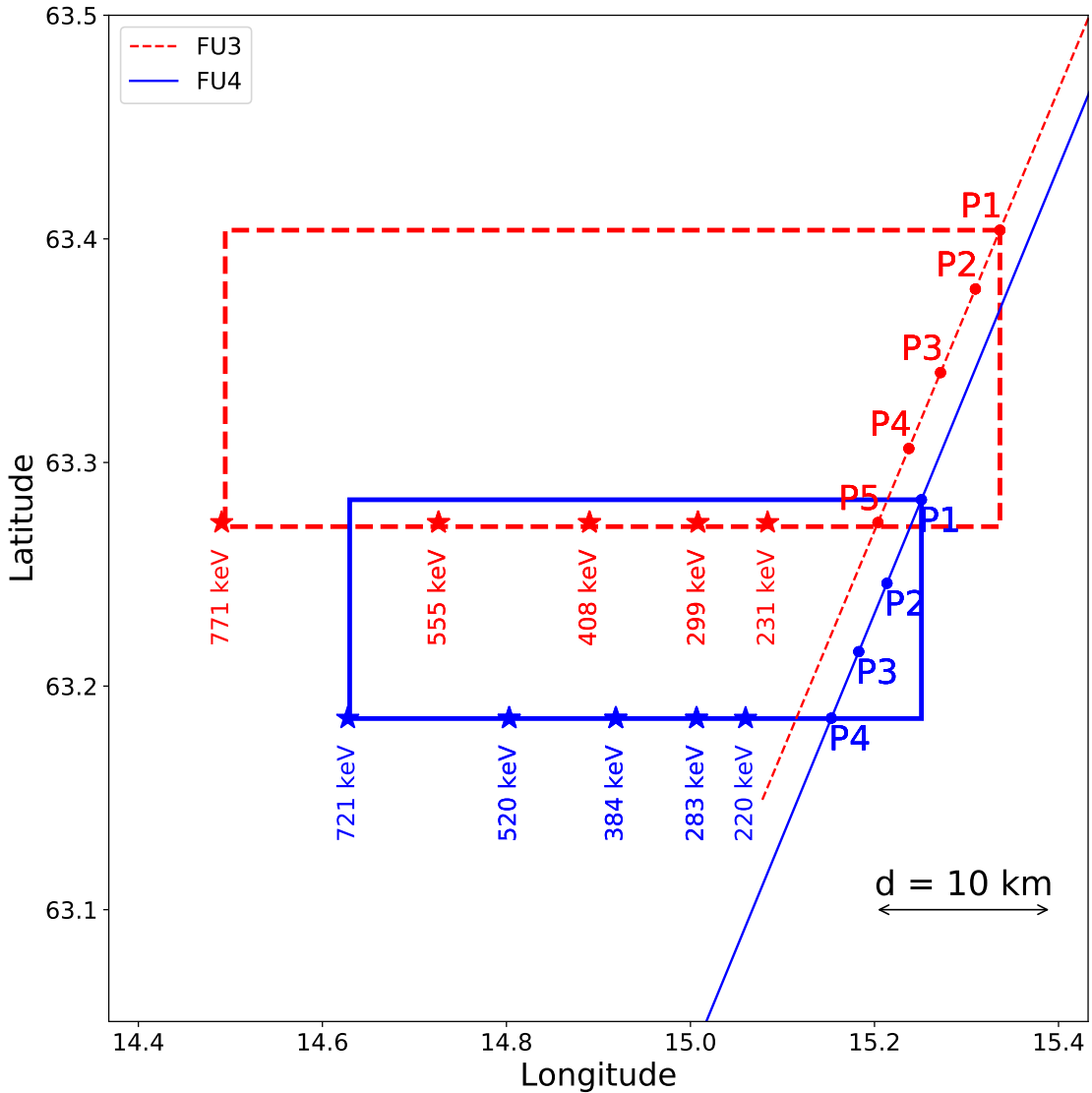


Figure 3.3: The topology of the FIREBIRD-II orbit and the multiple bounces of the microburst projected onto latitude and longitude with axis scaled to equal distance. Attributes relating to FU3 shown in red dashed lines, and FU4 with blue solid lines. The spacecraft path is shown with the diagonal lines, starting at the upper right corner. The labels P1-4 for FU4 and P1-5 for FU3 indicate where the spacecraft were when the  $N^{th}$  peak was seen in the lowest energy channel in the HiRes data. The stars with the accompanying energy labels represent the locations of the electrons with that energy that started at time of P1, and were seen at the last peak on each spacecraft. The rectangles represent the lower bound of the microburst scale size, assuming that the majority of the electrons were in the upper boundary of energy channel 4.

observed. The stars in Fig. 3.3 (with labels corresponding to energy channel boundaries) represent the locations when the microburst was observed at P1, such that an electron of that energy would drift eastward to be seen at P5 for FU3 and P4 for FU4. Since FU3 observed more peaks it observed the larger longitudinal scale size which is shown with the red dashed box in Fig. 3.3. FU3's fourth energy channel's bounds are 555 keV and 771 keV, which correspond to longitudinal distances of  $39 \pm 1$  km and  $51 \pm 1$ , respectively. The uncertainty was estimated by propagating the uncertainty in the bounce time Eq. 3.1. While the observed minimum longitudinal scale size is dependent on FIREBIRD-II's energy channels, the true scale size may not be.

To investigate how the microburst scale size compares to the scale sizes of chorus waves near the magnetic equator, the microburst's longitudinal and latitudinal scale sizes and their uncertainties in LEO were mapped to the magnetic equator with T89. The radial scale size (latitudinal scale mapped from LEO) was greater than  $500 \pm 10$  km. The azimuthal scale size (longitudinal scale mapped from LEO) of 555 keV electrons was greater than  $450 \pm 10$  km and for the 771 keV electrons it was greater than  $530 \pm 10$  km. The lower bound microburst scale size is similar to the chorus scale sizes derived by Agapitov et al. (2017, 2011), and is discussed below.

### Discussion and Conclusions

We presented the first observation of a large microburst with multiple bounces made possible by the twin FIREBIRD-II CubeSats. The microburst's lower bound LEO latitudinal and longitudinal scale sizes of  $29 \pm 1$  km and  $51 \pm 1$  km make it one of the largest observed. The microburst's LEO scale size was larger than the latitudinal scale sizes of typical  $> 1$  MeV microbursts reported in Blake et al. (1996), approximately 10 times larger than reported in Dietrich et al. (2010), and

approximately 2.6 times larger than other simultaneous microbursts observed by FIREBIRD-II (Crew et al., 2016). Lastly, the scale sizes derived here were similar to the scale sizes of  $\sim 15$  keV microbursts observed with a high altitude balloon (Parks, 1967). No energy dependence on the minimum latitudinal scale size was observed, while the observed energy dependence of the minimum longitudinal scale size is an artifact of the technique we used to estimate their drift motion.

The microburst scale size obtained in Section 3 and scaled to the geomagnetic equator can be compared with the scales of chorus waves presumably responsible for the rapid burst electron precipitation. Early direct estimates of the chorus source scales were made by the coordinated measurement by ISEE-1, 2. The wave power correlation scale was estimated to be about several hundred kilometers across the background magnetic field (Gurnett et al., 1979). Furthermore, Santolik et al. (2003) determined the correlation lengths of chorus-type whistler waves to be around 100 km based on multipoint CLUSTER Wide Band Data measurements near the chorus source region at  $L \approx 4$ , during the magnetic storm of 18 April 2002. Agapitov et al. (2017, 2011, 2010) recently showed that the spatial extent of chorus source region can be larger, ranging from 600 km in the outer radiation belt to more than 1000 km in the outer magnetosphere. The lower bound azimuthal and latitudinal scales obtained in Section 3 and scaled to the magnetic equator, are similar to the whistler-mode chorus source scale sizes reported in Agapitov et al. (2017, 2011).

No wave measurements from nearby spacecraft were available at this time. Nevertheless, during the hours before and after this observation, the Van Allen Probes' (Mauk et al., 2013) Electric and Magnetic Field Instrument and Integrated Science (Kletzing et al., 2013) observed strong wave power in the lower band chorus frequency range, inside the outer radiation belt between 22 and 2 MLT. Furthermore,  $AE \sim 400$  nT at this time, and relatively strong chorus waves were statistically more likely to

be present at FIREBIRD-II's MLT (Li et al., 2009b).

The empirically estimated and modeled  $t_b$  in this study agree within FIREBIRD-II's uncertainties, confirming that the energy-dependent dispersion was due to bouncing. The  $t_b$  curves are a proxy for field line length, and this agreement implies that they are comparable. This is expected since the magnetosphere is not drastically compressed at 8 MLT, but we expect a larger discrepancy near midnight, where the magnetosphere is more stretched and difficult to accurately model. In future studies, this analysis can be used as a diagnostic tool to validate field line lengths, and improve magnetic field models.

The similarity of the microburst and chorus source region scale sizes, as well as magnetospheric location and conditions, further support the causal relationship between microbursts and chorus.

#### Acknowledgments

This work was made possible with help from the FIREBIRD team, and the members of the Space Sciences and Engineering Laboratory at Montana State University for their hard work to make this mission a success. In addition, M. Shumko acknowledges Drew Turner for his suggestions regarding the bounce period calculations, and Dana Longcope for his proofreading feedback. The FIREBIRD-II data are available at [http://solar.physics.montana.edu/FIREBIRD\\_II/](http://solar.physics.montana.edu/FIREBIRD_II/). This analysis is supported by the National Science Foundation under Grant Numbers 0838034 and 1339414. Furthermore, the work of O. Agapitov was supported by the NASA grant NNX16AF85G.

## MICROBURST SIZE DISTRIBUTION DERIVED WITH AEROCUBE-6

Contribution of Authors and Co-Authors

Manuscript in Chapter 1

Author: M. Shumko

Contributions: Found microbursts in the AC6 data and calculated their size distribution.

Co-Author: A.T. Johnson

Contributions: Provided ideas and advice on how to analyze the AC6 data.

Co-Author: J.G. Sample

Contributions: Provided ideas and advice on how to analyze the AC6 data.

Co-Author: B.A. Griffith

Contributions: Checked the microburst detections by eye.

Co-Author: D.L. Turner

Contributions: Provided the initial inspiration for this project.

Co-Author: T.P. O'Brien

Contributions: Provided the initial inspiration for this project, proposed to use the cumulative distribution function analysis technique, and provided advise on how to use the AC6 data to address the noise issues.

Co-Author: O. Agapitov

Contributions: Provided the THEMIS wave dataset for the direct comparison of the microburst and chorus size distributions

Co-Author: J.B. Blake

Contributions: Provided advise on how to use the AC6 data and address the noise issues.

Co-Author: S. G. Claudepierre

Contributions: Checked the microburst size models and provided analysis advice

Manuscript Information

M. Shumko, A.T. Johnson, J.G. Sample, B.A. Griffith, D.L. Turner, T.P. O'Brien, O. Agapitov, J.B. Blake, S. G. Claudepierre

Journal of Geophysical Research

Status of Manuscript:

- Prepared for submission to a peer-reviewed journal
- Officially submitted to a peer-reviewed journal
- Accepted by a peer-reviewed journal
- Published in a peer-reviewed journal

Wiley

Key Points

- The dual AeroCube-6 CubeSats simultaneously observed  $> 35$  keV microbursts at a variety of spatial separations ranging from 2 to  $\approx 100$  km.
- In low Earth orbit the majority of microbursts have a size on the order of a few tens of km.
- At the magnetic equator, the size of most microbursts corresponds to the size of whistler-mode chorus wave packets.

Abstract

Microbursts are an impulsive increase of electrons from the radiation belts into the atmosphere and have been directly observed in low Earth orbit and the upper atmosphere. Prior work has estimated that microbursts are capable of rapidly depleting the radiation belt electrons on the order of a day, hence their role to radiation belt electron losses must be considered. Losses due to microbursts are not well constrained, and more work is necessary to accurately quantify their contribution as a loss process. To address this question we present a statistical study of  $> 35$  keV microburst sizes using the pair of AeroCube-6 CubeSats. The microburst size distribution in low Earth orbit and the magnetic equator was derived using both spacecraft. In low Earth orbit, the majority of microbursts were observed while the AeroCube-6 separation was less than a few tens of km, mostly in latitude. To account for the statistical effects of random microburst locations and sizes, a Monte Carlo and analytic models were developed to test hypothesized microburst size distributions. A family of microburst size distributions were tested and a Markov Chain Monte Carlo sampler was used to estimate the optimal distribution of the microburst size model

parameters. Finally, a majority of observed microbursts map to sizes less than 200 km at the magnetic equator. Since microburst are widely believed to be generated by scattering of radiation belt electrons by whistler mode waves, the observed microburst size correlates to coherent whistler mode chorus sizes derived in prior literature.

### Introduction

Since the discovery of the Van Allen radiation belts in the 1960s by Van Allen (1959) and Vernov and Chudakov (1960), decades of research has made headway in understanding the various particle acceleration and loss mechanisms. One of the extensively studied mechanisms responsible for both acceleration and loss is wave-particle scattering between whistler-mode chorus waves and electrons (Abel and Thorne, 1998; Bortnik et al., 2008; Horne and Thorne, 2003; Meredith et al., 2002; Millan and Thorne, 2007; Thorne et al., 2005). Whistler-mode chorus waves are typically generated by a temperature anisotropy of low energy electrons up to tens of kiloelectronvolts (keV) and are typically found in the  $\sim 0 - 12$  magnetic local times (MLT) (Li et al., 2009a,b). Whistler-mode chorus waves interact with radiation belt electrons, and are widely believed to cause electron precipitation termed microbursts (e.g. Millan and Thorne, 2007).

Microbursts are a subsecond impulse of electrons that are observed by high altitude balloons and satellites in low Earth orbit (LEO) on radiation belt magnetic footprints  $\sim 4 - 8$  L-shell (L) (e.g. Anderson and Milton, 1964; Breneman et al., 2017; Crew et al., 2016; Greeley et al., 2019; Lorentzen et al., 2001a; Mozer et al., 2018; O'Brien et al., 2003; Tsurutani et al., 2013; Woodger et al., 2015), mostly in the dawn MLTs, and with an enhanced occurrence rate during disturbed magnetospheric times (Douma et al., 2017; O'Brien et al., 2003). Microburst's role as a radiation belt electron loss mechanism has been estimated to be significant, with total radiation belt

electron depletion due to microbursts estimated to be on the order of a day (Breneman et al., 2017; Lorentzen et al., 2001b; O'Brien et al., 2004; Thorne et al., 2005). These average microburst loss estimates are not well constrained due to assumptions made regarding the microburst precipitation region.

One of the unconstrained microburst parameters that is critical to better quantify the role of microbursts as an instantaneous loss mechanism (the number of electrons lost per microburst) is their physical size. Historically, after the bremsstrahlung X-ray signatures of microbursts were discovered by Anderson and Milton (1964), numerous microburst size studies were done using other balloon flights in the mid 1960s. Brown et al. (1965) used data from a pair of balloons separated by 150 km, mainly in longitude, and found that one third of all microbursts observed were temporally coincident. Trefall et al. (1966) then used the results from Brown et al. (1965) to model the probability that a microburst will be observed by two balloons as a function of the radius of the microburst, radius of the precipitating area a balloon is sensitive to, and the balloon separation. Trefall et al. (1966) concluded that the microbursts reported by Brown et al. (1965) must have had a diameter of 230 km assuming a balloon has a circular field of view with a 140 km diameter (for electrons stopped at 100 km altitudes). Soon after, Barcus et al. (1966) used a pair of balloons and concluded that a microburst must have a  $< 200$  km longitudinal extent. Then Parks (1967) used data from a single balloon with four collimated scintillators oriented in different directions and found that the size of some mostly low energy microbursts to have a diameter of  $80 \pm 28$  km, and others were less than 40 km.

Direct observations of microburst electrons are made by LEO spacecraft. Blake et al. (1996) found a microburst with a size of a few tens of km using the the Solar Anomalous and Magnetospheric Particle Explorer (SAMPEX) and concluded that typically microbursts are less than a few tens of electron gyroradii in size (order of

a few km in LEO). Recently, Dietrich et al. (2010) used SAMPEX observations in another case study and concluded that the observed microbursts were smaller than 4 km. Crew et al. (2016) used the Focused Investigation of Relativistic Electron Bursts: Intensity, Range, and Dynamics (FIREBIRD-II) CubeSats and found an example of a microburst larger than 11 km. Lastly, Shumko et al. (2018) also used FIREBIRD-II to identify a microburst with a size greater than  $51 \pm 1$  km. If anything, the large variance in prior results imply that there is a distribution of microburst scale sizes which this study aims to estimate.

Besides addressing the instantaneous radiation belt electron losses due to individual microbursts, the microburst size distribution is useful to identify the wave mode(s) responsible for scattering microbursts. By mapping the microburst size distribution in LEO to the magnetic equator it can be compared to the wave sizes estimated in prior literature. This comparison can be used to identify the waves and their properties (e.g. amplitude or coherence) responsible for scattering microburst electrons.

This paper addresses these two questions by expanding the prior microburst size case studies by analyzing microburst observations over a three year time period to estimate the microburst size distribution in LEO and the magnetic equator. The twin AeroCube-6 (AC6) CubeSats are utilized for this study because they were ideally equipped to observe microbursts simultaneously over a span of three years while their total separation varied between 2 and 800 km, mostly in latitude (in-track in orbit). This paper first describes the AC-6 mission, including their orbit and instrumentation in section 4. Section 4 develops the methodology used to identify microbursts observed by each spacecraft and how they were combined to make a list of simultaneously observed microbursts. Section 4 describes the methodology used to estimate the microburst size distributions in LEO and the magnetic equator as a function of AC6

separation. Then a model is developed to shed light on how the compounding effects of a hypothesized microburst shape, size distribution, and random microburst locations will be observed by AC6, a two-point measurement platform. Lastly, in section 4 we discuss these results and compare the microburst sizes estimated here to the size distribution of the whistler-mode chorus waves that are believed to cause microbursts.

### Instrumentation

The AC6 mission consists of a pair of 0.5U (10x10x5 cm) CubeSats built by The Aerospace Corporation and launched on June 19th, 2014 into a 620 x 700 km, 98° inclination orbit. The two satellites, designated as AC6-A and AC6-B, separated after launch and drifted apart. Both AC6 units have an active attitude control system which allows them to adjust the atmospheric drag experienced by each AC6 unit by orienting their solar panel “wings” with respect to the ram direction. By changing their orientation, AC6 was able to achieve fine separation control and maintain a separation between 2-800 km. Figure 4.1a shows the AC6 separation for the duration of the mission. Figure 4.1b shows where AC6 was taking 10 Hz data simultaneously as a function of L and MLT which highlights that most data was taken at 8-12 MLT, an ideal local time for observing microbursts. Lastly Fig. 4.1b shows that the AC6 orbit was roughly dawn-dusk, sun-synchronous and precessed only a few hours in MLT over a three year period.

Each AC6 unit is equipped with three Aerospace microdosimeters (licensed to Teledyne Microelectronics, Inc). The dosimeter used for this study is dos1 and is identical on both AC6 units. Dos1 has a 35 keV electron threshold and all dosimeters sample at 1 Hz in survey mode, and 10 Hz in burst mode in the radiation belts. More detailed technical information on AC6 is described in O’Brien et al. (2016b).

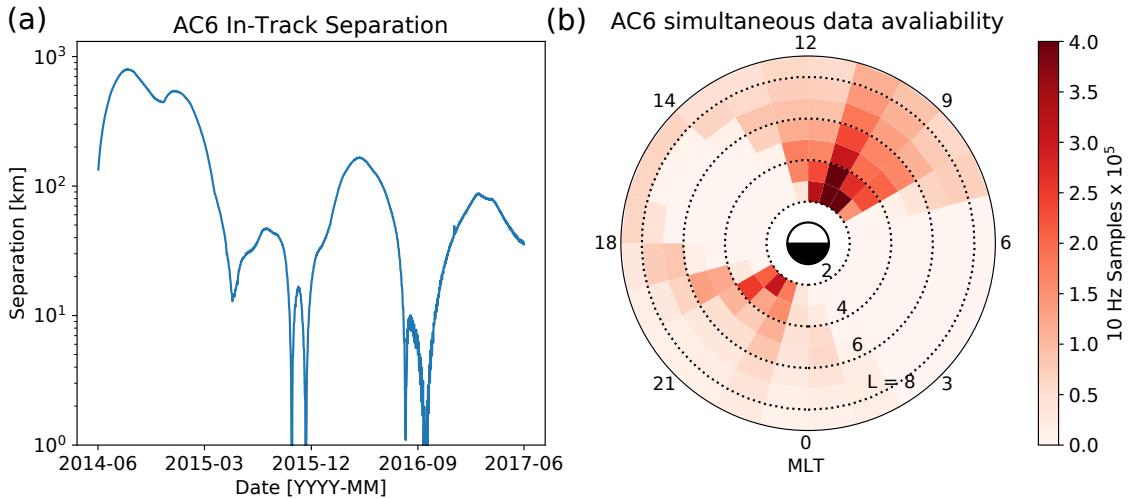


Figure 4.1: AC6 mission properties for (a) spacecraft separation and (b) number of simultaneous quality 10 Hz samples as a function of L and MLT.

### Methodology

#### Microburst Detection

The first step to find microbursts observed simultaneously by AC6 is to identify them on each individual spacecraft. Microbursts were detected with two different methods that yielded quantitatively similar results. The first method is the burst parameter (O'Brien et al., 2003). This algorithm has been successfully used in other microburst studies, mainly with the microbursts observed by SAMPEX (e.g. Blum et al., 2015; Douma et al., 2017; O'Brien et al., 2003). For AC6, a burst parameter threshold of 5 was determined to be a good trade-off between false positive and false negative microburst detections. Another microburst detection algorithm based on wavelet spectra frequency filtering was developed and the resulting list of microbursts is similar to the list from the burst parameter.

With the two microburst detection lists in hand, data cleaning to remove microburst-like transmitter noise was necessary. The transmitters on AC6 can

cause unphysical count impulses in the dosimeters that resembles periodic trains of microbursts. One source of transmitter noise was observed at times when AC6 was in contact with the ground stations above the US for data downloads and commanding, thus the microburst detections made above the US that were mostly at low L were discarded.

Another source of noise is crosslink transmissions between AC6-A and AC6-B. These transmissions occurred when either spacecraft transitioned from the survey mode to 10 Hz mode. This noise is sometimes not caught by the data quality flag, so the following empirically-derived criteria were developed to remove those detections. The dosimeter with a 250 keV nominal electron threshold, dos2, was used because it had a nearly identical response to noise while rarely responded to microbursts. Since the transmitter noise is very periodic with a  $\approx 0.2$  s period, cross-correlation (CC) and autocorrelation (AC) methods were applied to the dos1 and dos2 time series. Detections were discarded if the following two criteria were met: either dos1 or dos2 time series had a AC peak at a 0.2 or 0.4 s lag and the dos1-dos2 CC was greater than 0.9. The AC lag criteria alone sometimes falsely removed legitimate trains of microbursts, so the second criteria insured that the detection was removed if there was also an unphysically high correlation across an order of magnitude in energy.

The lists of microbursts observed individually by AC6 were then merged into a list of temporally correlated microbursts, i.e. microbursts that were observed simultaneously by both AC6 units, with the following procedure. The general idea is that a microburst detected by one spacecraft will cross-correlate well with the time series from the other spacecraft if it observed a similar microburst, and poorly if there was no microburst observed by the other spacecraft. Each microburst detection made by either spacecraft was cross-correlated with the time series from the other spacecraft whether or not a microburst was observed by the other spacecraft. Cross-

correlation windows with 1 and 1.2 s widths were chosen with slightly different window sizes to account for random count variation due to Poisson noise. Microbursts detections that had a cross-correlation greater than 0.8 were considered temporally coincident. This CC threshold was chosen as it is low enough to accept user-identified temporally coincident microbursts superposed with noise, and high enough to reject most non-coincident events. Figure 4.2, panels (a), (c), (e), and (g) show examples of microbursts observed by both AC6 units when they were separated by 5, 16, 37, and 69 km, respectively.

The last criteria requires that the temporal CC must be greater than the spatial CC + 0.3. The spatial CC was calculated by shifting one spacecraft's time series by the in-track lag to cross-correlate in the same spatial location, i.e. latitude. This criteria was applied to remove curtains, stationary structures observed by AC6 that are narrow in latitude (Blake and O'Brien, 2016) that can be misidentified as microbursts. Figure 4.2, panels (b), (d), (f), and (h) show the shifted time series to confirm that there were no spatially correlated, non-microburst structures present. Lastly the merged microburst list was spot checked by two authors to remove poorly correlated and any duplicate events. After filtering out transmitter noise and applying the CC criteria, 662 simultaneous microburst detections were found and used in this study.

### Microburst Size Distribution in LEO and Magnetic Equator

The temporally coincident microbursts, which from now on will be referred to as microbursts, are now used to estimate the fraction of microbursts observed above AC6 separation,  $s$ . When AC6 observes a microburst at  $s$ , the microburst's size must be greater than  $s$ . This fact, along with the arguments presented in Section 4 in Joy et al. (2002) who studied the most probable Jovian magnetopause and bow

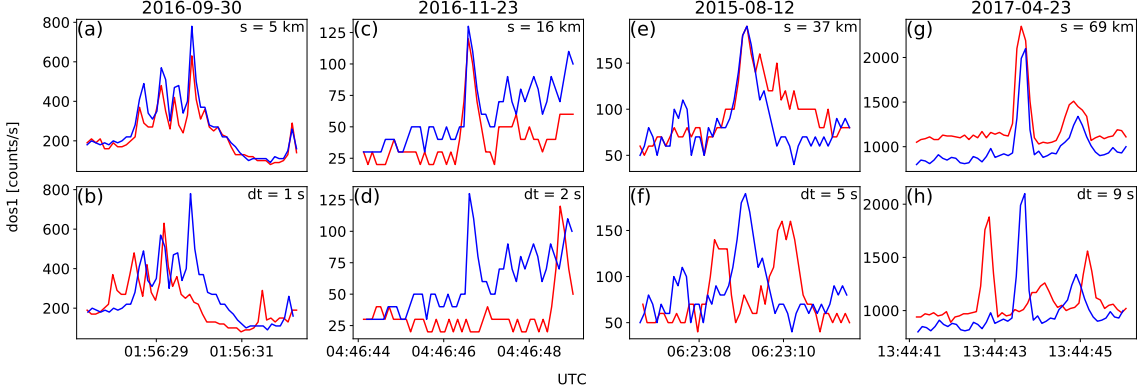


Figure 4.2: Examples of  $> 35$  keV microbursts observed simultaneously by AC6-A in red and AC6-B in blue. Panels (a), (c), (e), and (g) show the temporally-aligned time series when AC6 were separated by  $s = 5, 16, 37$ , and  $69$  km, respectively. The corresponding panels (b), (d), (f), and (h) show the spatially-aligned time series which is made by shifting the AC6-A time series in the above panels by the in-track lag (annotated with  $dt$ ) that show any spatially correlated structures. The clear temporal correlation and lack of spatial correlation demonstrates that these events are microbursts.

shock stand off distances, are used to investigate the dependence of the number of microbursts observed above  $s$ , as a function of  $s$ . This dependence is the microburst complementary cumulative distribution function  $\bar{F}(s)$ .

The cumulative fraction of microbursts observed above  $s$  is the ratio of  $N(s)$ , the normalized number of microbursts observed above  $s$ , to  $N(0)$ , the total number of microbursts observed

$$\bar{F}(s) = \frac{N(s)}{N(0)} \quad (4.1)$$

where  $N(s)$  is defined by

$$N(s) = \sum_{i=s}^{\infty} n_i \left( \frac{S_{max}}{S_i} \right) \quad (4.2)$$

where  $n_i$  is the number of microbursts observed by AC6 in  $i$ th separation bin. The normalization term  $S_{max}/S_i$  is a ratio of the number of 10 Hz samples in

the most sampled separation bin to the number of samples in the  $i$ th bin. This normalization factor corrects AC6's non-uniform sampling in separation, thus  $\bar{F}(s)$  can be interpreted as the fraction of microbursts observed above  $s$  assuming AC6 sampled evenly in separation. Microburst  $\bar{F}(s)$  in LEO is shown by the black curve in Fig. 4.3a for  $4 < L < 8$  and split into one L-wide bins with the colored curves. The separation bin width used in Fig. 4.3 is 5 km. To check for bias in  $\bar{F}(s)$  due to the choice of separation bins,  $\bar{F}(s)$  was resampled using other bin widths and offsets. Bin widths as large as 20 – 30 km and bin offsets did not qualitatively effect the curves in Fig. 4.3a. The normalization i.e., the number of 10 Hz samples in each separation bin, is shown in 4.3c.

The overall trend in Fig. 4.3a shows a sudden cumulative probability drop off, followed by a shoulder up to  $s \approx 70$  km where  $\bar{F}(s)$  drops to nearly zero. A large negative gradient of  $\bar{F}(s)$  at some separation implies that microbursts must be smaller than that separation. To quantify this, Fig. 4.3b shows the microburst probability density function (PDF), calculated by differentiating  $\bar{F}(s)$ . The microburst PDF shows a peak at  $s < 30$  km as well as a peak between 70 – 80 km separation. These PDF peaks are evidence of a sub 30 km microburst population and larger microbursts observed up 70–80 km separations. The shaded region around the black curves in Fig. 4.3a-b shows the standard error due to counting statistics. The uncertainty due to false coincidence events i.e. two unrelated microbursts lining up in time by random chance was also considered. The microburst duty cycle in a one minute window ( $\approx 1 L$ ) around each microburst was calculated. The false coincidence probability is the square of the duty cycle and was found to be less than 5% for the majority of microbursts. The false coincidence probability for each microburst was then used to randomly remove microbursts and  $\bar{F}(s)$  was recalculated in  $10^4$  trials. The spread in the  $\bar{F}(s)$  trial curves with microbursts randomly removed was much smaller than the

uncertainty due to counting statistics alone.

To compare the microburst size to the size of their hypothesized progenitor waves, the spacecraft locations during observed microbursts were mapped to the magnetic equator using the Olson-Pfitzer magnetic field model (Olson and Pfitzer, 1982) which is implemented with a Python wrapper for IRBEM-Lib (Boscher et al., 2012). As previously stated, a microburst observed in LEO has a size larger than the spacecraft separation, hence that microburst would also have a size larger than the spacecraft separation after it was mapped to the magnetic equator. Thus the procedure to estimate  $\bar{F}(s)$  is identical to the LEO size distribution but with a different normalization. The normalization factors were calculated by mapping every quality AC6 sample to the magnetic equator and binning them by equatorial separation into 100 km wide bins. Figure 4.4 shows the equatorial microburst size distribution in the same format as Fig. 4.3. The equatorial PDF trend is similar to LEO and most of the microbursts were observed when the AC6 equatorial separation was less than 200 km.

The results in Figs. 4.3 and 4.4 show the fraction of microbursts observed above a spacecraft separation and do not fully represent the microbursts size distribution due to the compounding effects from the range of microburst sizes and random locations of microbursts with respect to AC6 i.e. even if the microburst size is much larger than the AC6 separation, some fraction of those microbursts will be only observed by one AC6 spacecraft. Thus modeling is necessary to capture the compounding influence of these statistical effects on AC6.

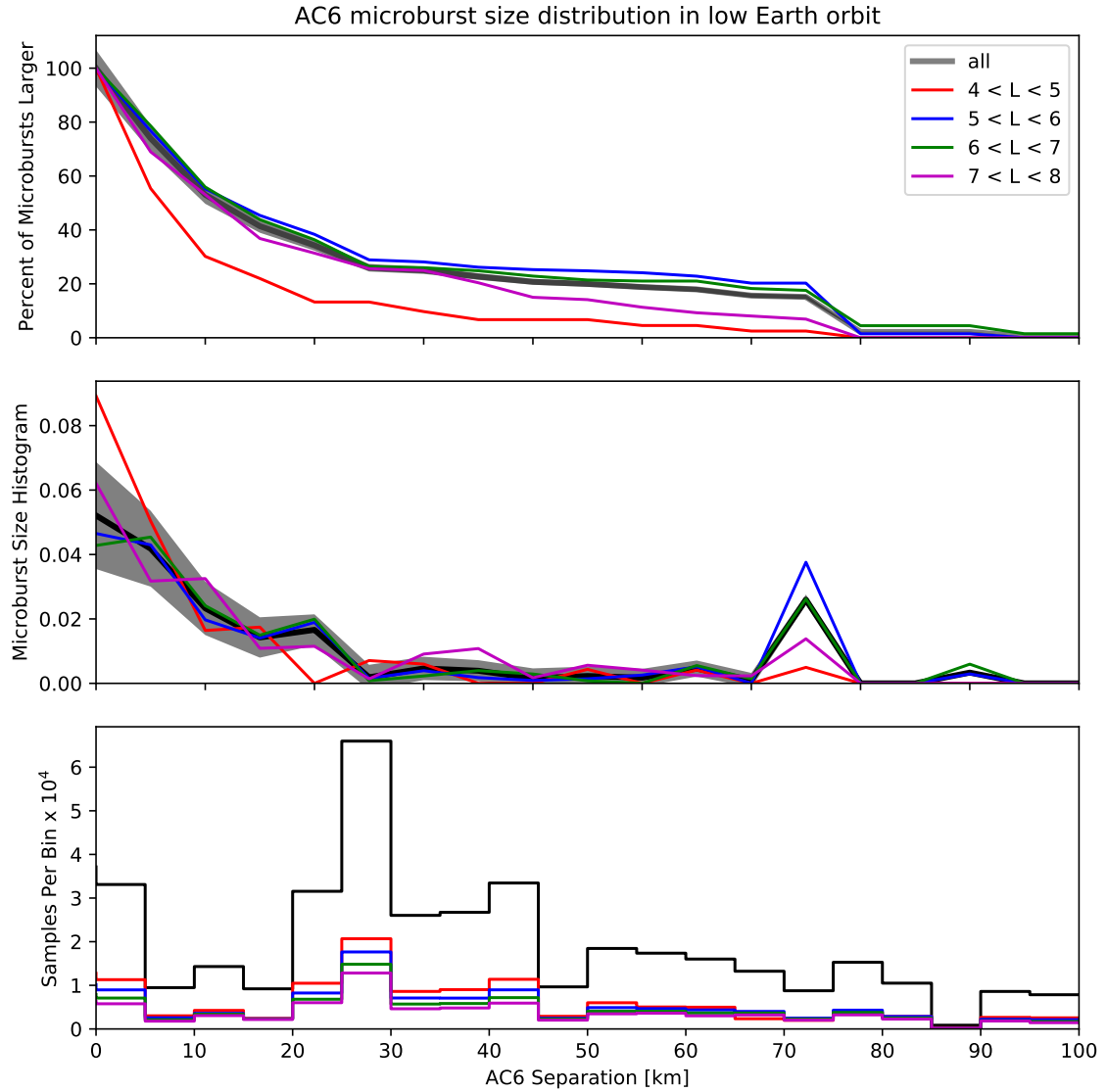


Figure 4.3: Microburst size distribution in low Earth orbit. Panel (a) shows the percent of microbursts observed above that separation after normalizing for the uneven AC6 sampling in separation. Panel (b) shows the microburst probability density (size histogram) as a function of separation. Lastly, panel (c) shows the normalization, i.e. number of simultaneous samples AC6 observed as a function of separation. The colored lines show the distributions binned by  $L$ , and the thick black curve for the entire radiation belt ( $4 < L < 8$ ). The gray shading around the black curve shows the uncertainty due to counting statistics.

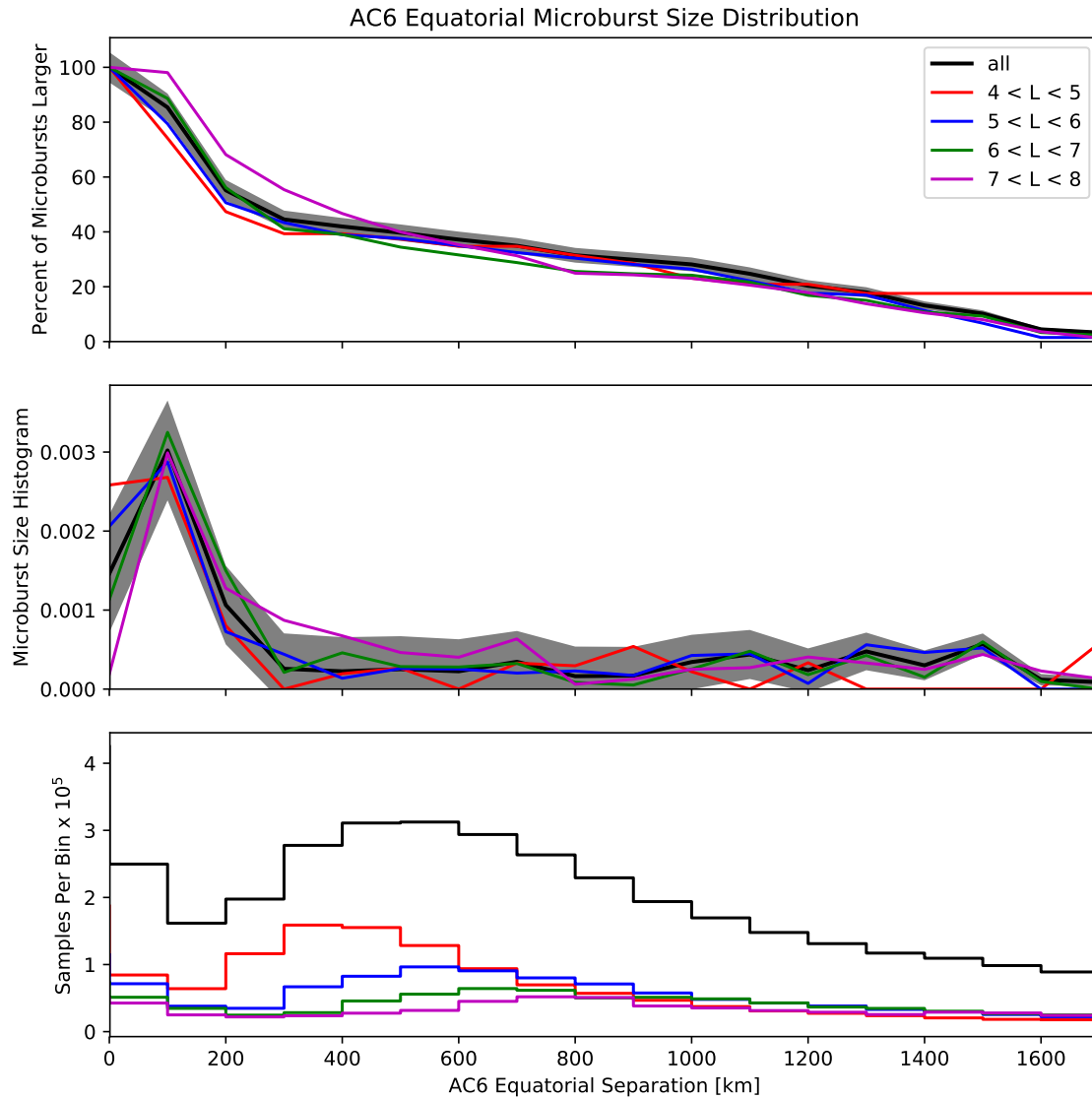


Figure 4.4: Microburst size distribution mapped to the magnetic equator in the same format as Fig. 4.3.

### Modeling the Distribution of Microburst Sizes

#### Monte Carlo and Analytic Models to Calculate $\bar{F}(s)$

To account for the effects due to microbursts randomly occurring around AC6 with an unknown distribution of microburst sizes, Monte Carlo (MC) and analytic models were developed. These models assume a hypothesized distribution of microburst sizes expressed with a probability density function  $p(d|\theta)$  where  $\theta$  are the dependent variables, and a microburst footprint shape to estimate  $\bar{F}(s)$ . The microburst footprint is assumed to be circular with a diameter  $d$ .  $p(d|\theta)$  can be understood as “the probability of observing a microburst of diameter  $d$ , given the parameters  $\theta$ ”. Various microburst size distributions were considered: a one-size and two-size microburst populations, and continuous  $p(d|\theta)$  such as Maxwell, Weibull, and log-normal.

The Monte Carlo model is the most intuitive. It first randomly scatters  $10^5$  microburst centers in a  $400 \times 400$  km grid around AC6. Then each microburst center was assigned a diameter, randomly picked from a  $p(d|\theta)$  distribution after  $\theta$  parameters were specified. Spacecraft A is placed at the origin, and spacecraft B is placed along the positive y-axis at distances from spacecraft A corresponding to the AC6 separation bins used in Section 4. Then for each spacecraft B location, the number of microbursts that encompass both spacecraft was counted. The modeled fraction of microbursts observed above  $s$  is then

$$\bar{F}(s) = \frac{\sum_{i>s}^{\infty} n_i}{\sum_{i>0}^{\infty} n_i}. \quad (4.3)$$

where as before the number of microbursts observed by both spacecraft in the  $i$ th bin

is  $n_i$ .

The analytic model, while identical to the MC model, highlights the geometrical concepts connecting  $p(d|\theta)$  and  $\bar{F}(s)$  with geometry arguments similar to Trefall et al. (1966). For a microburst with  $d = 2r \geq s$ , there is an area between AC6 where that microburst will be observed by both spacecraft if the microburst's center lands there. Figure 4.5a-c shows this geometry with the two spacecraft indicated with black dots with varying relations between  $r$  and  $s$ . All microbursts whose center lies inside the circular area of radius  $r$  surrounding either spacecraft will be observed by that spacecraft. If it exists, the intersection of the two circular areas around both spacecraft defines another area,  $A(r, s)$  where a microburst will be observed by both spacecraft if the microburst center lands there. This area can be calculated using the circle-circle intersection area equation,

$$A(r, s) = 2r^2 \cos^{-1} \left( \frac{s}{2r} \right) - \frac{s}{2} \sqrt{4r^2 - s^2}. \quad (4.4)$$

Example geometries where  $A(r, s) > 0$  are shown in Fig. 4.5b and c. With this conceptual model and  $A(r, s)$ , the analytic form of  $\bar{F}(s)$  can be found and is derived in the Supporting Information (SI) Text S1. To demonstrate the effects of random microburst locations near AC6, examples of the analytic and Monte Carlo  $\bar{F}(s)$  curves are shown in Fig. 4.5d for a one-size,  $d = 40$  km microburst population.

#### Methods for estimating optimal $\theta$ parameters

At this stage we have all of the ingredients to calculate  $\bar{F}(s)$  given a prescribed  $p(d|\theta)$ . For each  $p(d|\theta)$  tested, the optimal  $\theta$  parameters are estimated in this study using the traditional least squares regression and Bayesian inference. While we report the  $\theta$  parameters that minimize least squares, this section focuses on Bayesian inference because it seamlessly incorporates statistical uncertainty in the data. The

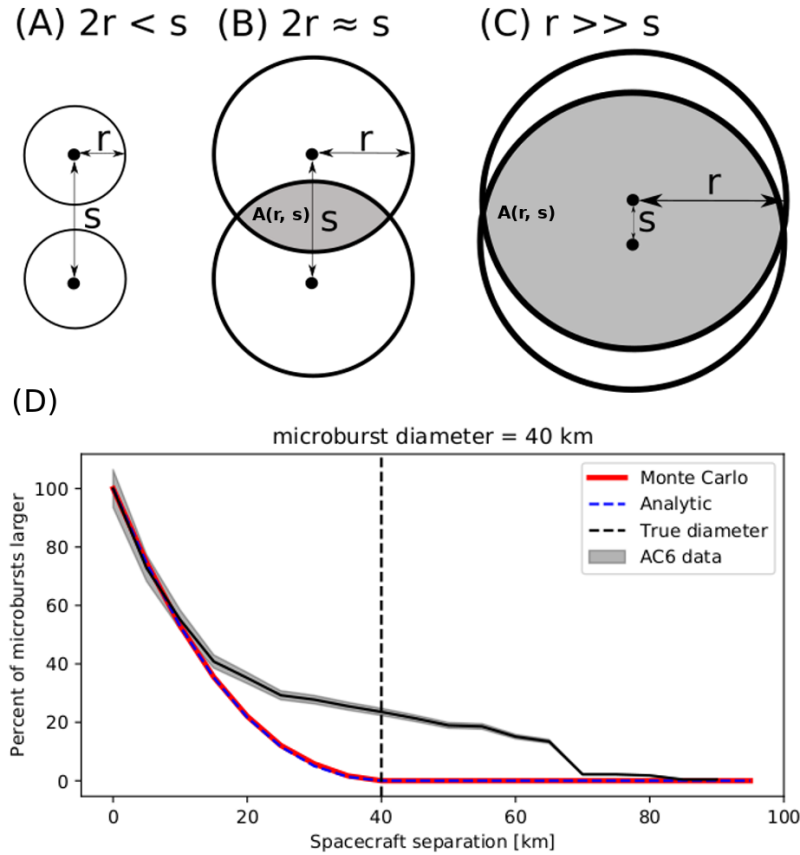


Figure 4.5: Panels A-C show the varying geometries of the analytic model. The two spacecraft are shown as black dots. The enclosing black circle around each spacecraft bounds the area where a microburst will be observed by one or both AC6 units if the microburst's center lies inside the circle. Panel (A) shows the case where microburst diameter is smaller than the AC6 separation and all microbursts will be observed by either unit A or B and never simultaneously. Panel (B) shows the intermediate case where the microburst diameter is comparable to the AC6 separation and some fraction of microbursts will be observed simultaneously. The fraction of the microbursts simultaneously observed is proportional to the circle intersection area  $A(r, s)$  and is shown with grey shading. Panel (C) shows the case where the microburst diameter is much larger than the spacecraft separation and nearly all microbursts will be observed by both spacecraft. Lastly panel (D) shows  $\bar{F}(s)$  from the AC6 data with a solid black line, and modeled MC and analytic  $\bar{F}(s)$  curves for a single-sized microburst distribution with  $d = 40$  km.

uncertainty in the data is then propagated to  $\theta$  which is then no longer an optimal value, rather a distribution of values that is consistent with the observations and its uncertainty.

Bayesian inference is rooted in Bayes theorem of conditional probability. Given the observed  $\bar{F}(s)$  as  $y$ , and model's dependent variables as  $\theta$ , Bayes theorem can be written as

$$p(\theta|y) = \frac{p(y|\theta)p(\theta)}{p(y)}. \quad (4.5)$$

$p(\theta)$  is the distribution of  $\theta$  that describe our prior level of knowledge about that parameter e.g. from earlier microburst size studies, a microburst size must less than 500 km in LEO. This is called the prior which is quantified by a PDF such as normal, uniform, etc. Next term is the likelihood,  $p(y|\theta)$ , the conditional probability of obtaining  $y$  given a particular  $\theta$ . The likelihood probability is a probabilistic penalty function that quantifies the discrepancy between the modeled and observed  $\bar{F}(s)$  in terms of the standard error. The resulting PDF of  $\theta$ s consistent with the observations is  $p(\theta|y)$  known as the posterior distribution. The posterior is an update to our prior distributions, modified by the likelihood i.e. the data and its uncertainties. Here, the posterior is used to make inferences regarding the range of  $\theta$  parameters that generate a  $\bar{F}(s)$  that is consistent with the observations. The last parameter in Bayes theorem is  $p(y)$ .  $p(y)$  is the marginal likelihood (evidence) that describes the probability of obtaining  $y$  after marginalizing over all prior variables. Calculation of  $p(y)$  is difficult, and often not necessary for model parameter estimation.

With all of the above terminology, the important takeaway is that the posterior distribution for each model parameter is interpreted as the range of our model's dependent parameters that are consistent with the observations. A 95% credible

interval (CI) for each model parameter is reported here that is interpreted as: assuming a hypothesized  $p(d|\theta)$ , there is a 95% probability that the true  $\theta$  is inside the CI. To sample the posterior distribution, the  $\theta$  parameter space is explored with a Markov Chain Monte Carlo (MCMC) sampler. In a nutshell a Markov Chain is a process that samples random variables that depend on only the previous state of those random variables. Hence a MCMC sampler is a Monte Carlo sampler that samples the  $\theta$  parameter space by picking random  $\theta$  values based on the previous state of  $\theta$ .

The first and one of the most popular MCMC is the Metropolis-Hastings sampler (Hastings, 1970; Metropolis et al., 1953). While the Metropolis-Hastings sampler is explained in detail in Metropolis et al. (1953) and Hastings (1970) and a good introduction given in Sambridge et al. (2006) as well as Sharma (2017), a brief overview is warranted. The Metropolis-Hastings sampler samples the posterior distribution in  $N$  trials. Once an initial set of  $\theta$  is randomly picked from the prior, the  $i^{th}$  trial involves the following steps. First calculate the posterior probability for  $\theta_i$ . Then pick a proposal  $\theta_{i+1}$  to jump to, randomly picked near  $\theta_i$  in parameter space. If the  $\theta_{i+1}$  posterior probability is higher than  $\theta_i$ , the MCMC accepts the proposal and moves to  $\theta_{i+1}$ . If the posterior probability of  $\theta_{i+1}$  is smaller than  $\theta_i$ , there is a random chance that  $\theta_{i+1}$  will be accepted or rejected (if rejected,  $\theta_{i+1} = \theta_i$  and a new proposal is generated). This accept/reject criteria allows the sampler to trend to more probable  $\theta$  while also exploring the neighboring regions. After the  $N$  trials, a histogram is made using the accepted  $\theta$ s to produce the posterior distribution for each model parameter.

#### Estimating optimal parameters for various microburst size models

The MCMC sampler is first used to test the simplest microburst size model where all microbursts are one size and the MCMC will estimate that size. The microburst

size PDF for this model can be expressed as

$$p(d|d_0) = \delta(d - d_0) \quad (4.6)$$

where  $\delta$  is the Dirac Delta function and  $d_0$  is the diameter of all microbursts according to this model. The range of  $d$  that are consistent with the observed  $\bar{F}(s)$  is shown in Fig. 4.6. Assuming this model, there is a 95% probability that the microburst diameter is between 38 and 129 km. As a sanity check the optimal size that minimizes least squares is 73 km.

A slight generalization of the one-size model is a two-size microburst population model that assumes the following microburst PDF

$$p(d|d_0, d_1, a) = a\delta(d - d_0) + (1 - a)\delta(d - d_1) \quad (4.7)$$

where the diameters of the two microburst populations are given by  $d_0$  and  $d_1$  and  $a$  is the parameter that quantifies the relative fractions of the two populations. The result of this model is shown in Fig. 4.7. The fit is slightly better than the one-size model, although that is to be expected given two more free model parameters. A majority, 98 %, of microbursts, have a diameter between 12 and 47 km with a rare population with a diameter between 76 and 234 km. The set of parameters that minimize least squares is 99.5 % of microbursts are small with a size of 21 km and the remaining 0.5 % of microbursts have a 140 km size.

Other, continuous PDFs were tested including: Maxwellian (Maxwell – Boltzmann), log-normal, and Weibull. The range of model parameters that are consistent with the observed  $\bar{F}(s)$  are presented in the SI text S2. These distributions were chosen because they have the following properties that are most realistic: they are continuous, approach 0 in the limit as  $r \rightarrow 0$  (lower bound microburst

size is ultimately limited by the electron gyroradius), and can be symmetrical or asymmetrical.

### Discussion

The LEO microburst  $\bar{F}(s)$  estimated in section 4 shows that a majority of coincident microbursts were observed by AC6 when they were separated by less than a few tens of km. This conclusion is consistent with prior literature and most similar to Parks (1967) who reported that many  $> 15$  keV microbursts are less than 40 km in diameter while others were on average  $80 \pm 28$  km in diameter. Furthermore, these results are similar to the bouncing packet example shown in Blake et al. (1996) with a size of “at least a few tens of kilometers”. The relatively small number of large  $> 70$  km microbursts observed by AC6 fit in well with the results from Barcus et al. (1966) and Brown et al. (1965), although the AC6 separation is mostly latitudinal while Barcus et al. (1966) and Brown et al. (1965) used data from pairs of balloons separated predominantly in longitude.

Without knowledge of the microburst shape, a direct comparison between the AC6 and balloon observations is difficult. Trefall et al. (1966) discussed how a hypothetical circular microburst at the scattering location near the magnetic equator will be stretched into an ellipse with a semi-major axis in the longitudinal direction. This stretching effect should be explored further as it introduces an ambiguity from the eccentricity of the ellipse that prevents a direct latitudinal and longitudinal comparison.

When comparing our results to more recent studies, the AC6 microburst size distribution is much larger than the sizes reported in Dietrich et al. (2010) who used very low (VLF) frequency transmission paths and SAMPEX to conclude that microbursts must be smaller than 4 km from a small number of microbursts observed

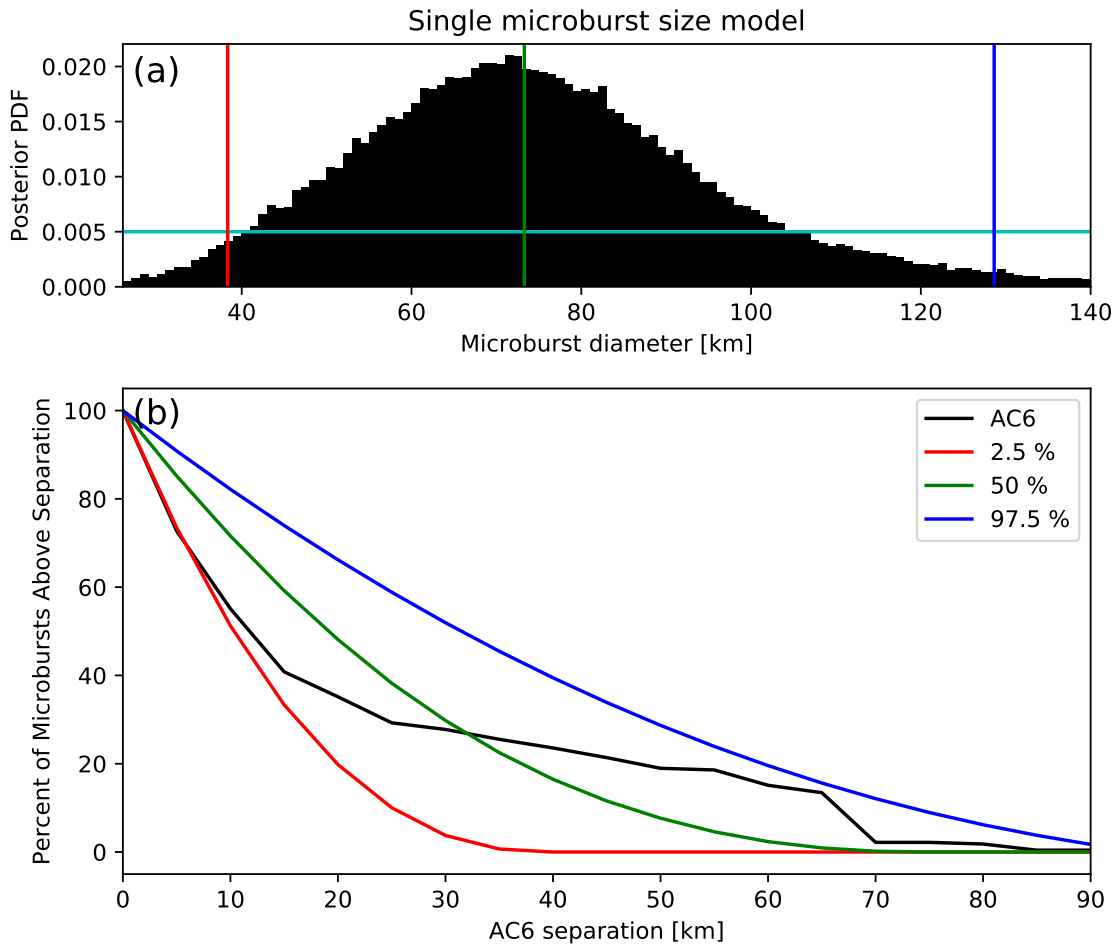


Figure 4.6: Range of plausible microburst sizes assuming all microbursts are one fixed size. Panel (a) shows the posterior probability density function of microburst diameters in black. The red, green, and blue vertical lines at 38, 73, and 129 km represent the 2.5, 50, and 97.5 posterior percentiles, respectively. A uniform prior between 0 and 200 km was assumed for this MCMC run and is shown in cyan. Panel (b) shows the percent of microbursts observed above an AC6 separation for  $4 < L < 8$  in black. The 2.5, 50 and 97.5 size percentiles were estimated from the posterior and plotted in red, green, and blue curves, respectively.

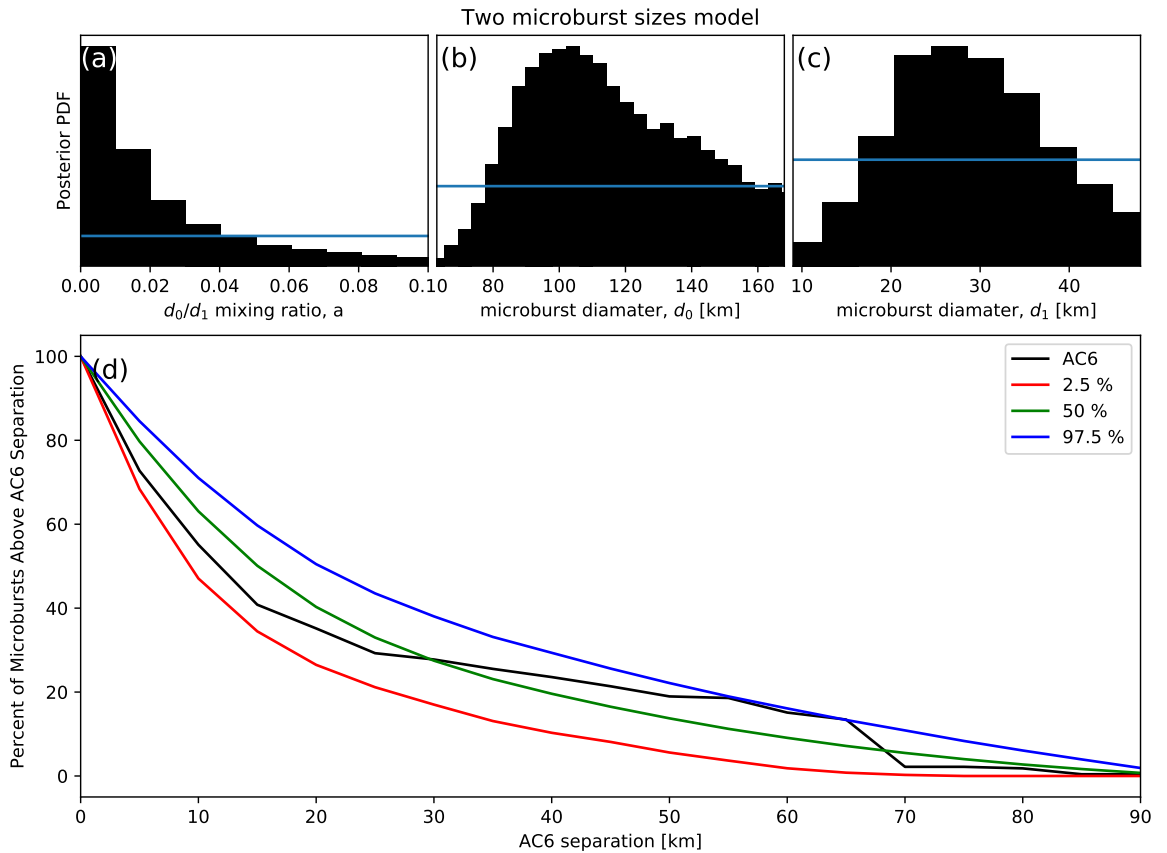


Figure 4.7: Plausible microburst percent curves assuming microburst size distribution is bimodal consisting of two sizes  $d_0$  and  $d_1$  with a mixing term that quantifies the relative occurrence of the  $d_0$  to  $d_1$  microburst populations. Panel (a) shows the posterior distribution for the microburst population mixing term,  $a$  with a median value of 0.02. The  $a$  prior was uniform between 0 and 0.2. Panel (b) shows the posterior distribution for  $d_0$ , the larger microburst population estimated with a uniform prior between 50 and 200 km and the posterior median diameter of 122 km. Panel (c) shows the posterior distribution for  $d_1$ , the smaller microburst population, estimated using a uniform prior between 0 and 50 km with a median diameter of 28 km. Panel (d) is similar to Fig. 4.6b and shows the AC6 microburst fraction for  $4 < L < 8$  in black. A set of 1000 random parameter triples ( $a$ ,  $d_0$ , and  $d_1$ ) were drawn from the posterior and used to generate a family of  $\bar{F}(s)$  curves. At each  $s$  the range of consistent  $\bar{F}(s)$  were quantified by the 2.5, 50 and 97.5 percentiles and shown with the red, green, and blue curves, respectively.

during one SAMPEX radiation belt pass. Dietrich et al. (2010) arrived at their conclusion by looking for temporal coincidence of microbursts and FAST events, subsecond VLF transmission perturbations, but the connection between FAST events and microbursts is not well understood. Lastly, our results are consistent with FIREBIRD-II observations of a  $> 11$  km microburst reported by Crew et al. (2016), and the minority of microbursts observed by AC6 up to  $s \approx 70$  km are consistent with the  $> 51$  km bouncing packet microburst reported in Shumko et al. (2018).

The microburst PDF shown in Fig. 4.3b suggests that the microburst size distribution is bimodal. This has been suggested before by Blake et al. (1996) who noted that the  $> 150$  keV and  $> 1$  MeV microbursts are not always well correlated e.g. Fig. 10 in Blake et al. (1996). The quality of the AC6 data is insufficient to definitively conclude that there are two distinct microburst populations. The different microburst population hypothesis can be better tested with an AC6-like mission with better energy resolution and homogeneous MLT coverage.

The model results from section 4 emphasize that care must be taken when comparing the  $\bar{F}(s)$  curves observed by AC6 and the true microburst size distribution due to the compounding effect of an unknown microburst size distribution, unknown microburst shape, and random microburst locations near AC6. By assuming there is only one microburst size, the results in Fig. 4.6 suggest that there is a 95% probability that the microburst diameter is somewhere between 38 and 129 km, a relatively wide range of values. On the other hand, the two-size model has a smaller variance around the AC6  $\bar{F}(s)$ , which is expected with the addition of two more free parameters. The two size model is interpreted as 98% of microbursts diameters are between 12 and 47 km and larger microbursts are very uncommon.

A variety of continuous  $p(d)$  such as the Maxwellian, Weibull and log-normal were also tested. While the continuous microburst PDFs are more realistic, there is

no clear choice of which microburst PDF nature prefers. The one and two-size model are simple to interpret, and the two-size model qualitatively fits the observations the best out of all  $p(d)$  tested. Surely nature does not only have two discrete microburst sizes. Rather, the current evidence and reasoning supports a bimodal and continuous PDF hypothesis. Due to lack of prior observations and theoretical predictions, it is difficult to identify and test a more appropriate  $p(d)$  hypothesis at this time.

The equatorial microburst  $\bar{F}(s)$  estimated in section 4 and Fig. 4.4b in particular shows that the majority of microbursts were observed when the equatorial AC6 separation was less than 200 km. We will now explore how these results compare to prior multi-point measurements of chorus source sizes made near the magnetic equator. The International Sun-Earth Explorers (ISEE 1 and 2) were used by Gurnett et al. (1979) to make one of the first direct chorus source scale measurements. Gurnett et al. (1979) estimated that the wave power correlation scale was on the order of a few hundred km across the background magnetic field. Using the Cluster Wide Band Data measurements Santolik et al. (2003) found the correlation scale of whistler mode chorus waves to be around 100 km near the source region at  $L \approx 4$  and midnight MLT sector. Furthermore, Turner et al. (2017) used the four satellites comprising the Magnetospheric Multiscale Mission and found that rising tone whistler mode chorus elements were phase coherent up to 70 km at  $L \approx 8$ . Lastly, Agapitov et al. (2017, 2011, 2010, 2018) used multiple sets of spacecraft missions with wave measurements near the chorus source region to statistically show that the extent of chorus source region can extend from 600 km in the outer radiation belt to greater than 1,000 km in the outer magnetosphere.

The equatorial microburst size of less than a few hundred km shows that the waves responsible for scattering microburst electrons must have correlated properties on those scales. The wave properties necessary for scattering microburst electrons

e.g. coherence, polarization, wave normal angle, etc. can be identified by studying the waves properties that are only observed by multiple equatorial spacecraft at small separations. These properties can then aid wave-particle scattering model development by constraining the wave properties and scattering modes responsible for scattering microburst electrons. In turn, future models could then make predictions regarding the distribution of microburst sizes in LEO.

### Conclusions

In conclusion, the twin AC6 CubeSats enabled the detailed statistical study of microburst sizes from a two point measurement platform. Roughly 60% of the  $> 35$  keV microbursts were simultaneously observed while AC6 was separated by less than 20 km and the rest were observed up to  $\approx 70$  km separation. Modeling the microburst cumulative distribution function is essential to quantify the relationship between the number of microbursts observed as a function of separation to a hypothesized microburst size distributions. The AC6 microburst data, together with modeling, has hinted at the existence of a bimodal microburst size PDF with the majority of microbursts with a diameter smaller than 40 km and a rare microburst population with a diameter around 100 km. The bimodal size hypothesis may be more comprehensively addressed from LEO spacecraft with more simultaneous microburst observations, homogeneous MLT coverage, and differential energy channels. Moreover, to disentangle the compounding effect that affects two-point microburst measurements, a X-ray imager on a high altitude balloon can observe the atmospheric microburst footprint and determine the microburst size, shape, and any spatial correlations with little ambiguity.

When mapped to the magnetic equator, most microbursts were observed while the mapped AC6 separation was less than 200 km. This correlates well with the sizes

of highly correlated chorus waves and it suggests that the wave properties crucial for scattering microbursts must be correlated over relatively small regions. By studying the wave properties that are correlated on a few hundred km scales, the dominant wave scattering modes may be identified.

#### Acknowledgments

This work was made possible with the help from the many engineers and scientists at The Aerospace Corporation who designed, built, and operated AC6. M. Shumko was supported by NASA Headquarters under the NASA Earth and Space Science Fellowship Program - Grant 80NSSC18K1204. D.L. Turner is thankful for support from the Van Allen Probes mission and a NASA grant (Prime award number: 80NSSC19K0280). **Other Aerospace and MSU funding sources...** The AC6 data is available at <http://rbspgway.jhuapl.edu/ac6> and the IRBEM-Lib version used for this analysis can be downloaded from <https://sourceforge.net/p/irbem/code/616/tree/>.

## CONCLUSIONS AND FUTURE WORK

In this dissertation we have explored the microburst scattering mechanism directly in Chapter 2 and indirectly in Chapters 3 and 4. In Chapter 2 we used particle and wave instruments on the Van Allen Probes to study microburst signatures near their scattering region inside the radiation belts. To these observations we applied the relativistic theory of wave-particle resonant diffusion and found that the motion of the microburst electrons was not along single-wave characteristic curves in momentum phase space, given the spacecraft position, orientation and the plasma environment. This result at first appears to contradict the belief that many members of the community hold, that microburst precipitation is due to a diffusive process. In reality both are probably valid on different time scales. Individual microbursts are probably not scattered diffusively, but the combined contribution of an ensemble of microbursts will have properties that are well modeled as a diffusion process.

The microburst sizes estimated in prior literature as well as Chapters 3 and 4 show that there is a large variability in microburst sizes although microbursts are generally small. The study in Ch. 3 gave us a glimpse into the dynamics of a rarely observed bouncing packet microburst from a dual point measurement platform. This study has shed light on the lower bound latitudinal and longitudinal sizes of that microburst, and it was found to be larger than microburst sizes reported in recent literature, and somewhat smaller than the microburst sizes observed with high altitude balloons in the mid 1960s. A comparison between satellites separated in latitude and balloons separated in longitude is somewhat an apples to oranges comparison because the microburst shape is still unknown.

The AC6 microburst study in Ch. 4 showed that in LEO, 60% of the 662 microbursts were observed while the AC6 separation was less than a few tens of km

while a minority of microbursts were observed up to  $\approx 100$  km separation. These conclusions agree with prior literature from high altitude balloons and LEO spacecraft, although as mentioned before the microburst shape makes comparisons somewhat ambiguous. The equatorial microburst size distribution is heavily dominated by microbursts smaller than 200 km. This is a very small size, highlighting that the waves that scatter microburst electrons must have correlated properties on those scales. A preliminary comparison between the equatorial distributions of microbursts and lower band whistler mode chorus waves shows a better agreement between high amplitude chorus waves and microbursts, although a more thorough study is necessary to address the various systematic biases.

### Future work

An extension of the case study in Chapter 2 is a statistical study using the Van Allen Probes. Other microburst-like events have already been identified by eye. These other events were also simultaneously observed with enhanced wave activity, hence they may be related and a further investigation is warranted. A microburst detection scheme similar to the one used in Chapter 4 can be easily implemented to automatically identify other microbursts for further study. A few compelling questions that can be addressed with this study are: what is the typical pitch angle extent of microbursts? Do these microbursts have a similar MLT distribution to microbursts observed in LEO? What fraction of microbursts were observed during enhanced wave activity? What wave modes and properties are observed during these events? And lastly, what fraction of microbursts can be modeled with a diffusive process?

Another study related to the electron bounce period analysis done in Ch. 3 can be used to verify magnetic field models and in particular the length of magnetic field lines. Current magnetospheric magnetic field models assume that Earth's internal

magnetic field is relatively static e.g. the International Geomagnetic Reference Field, and superpose that field with a highly dynamic field model who's dynamics are driven by the plasma environment in the magnetosphere and the solar wind. The difficulty lies in accurately modeling this dynamic field, and verifying these models is somewhat difficult. One verification technique involves identifying bouncing packet microbursts observed by SAMPEX and FIREBIRD, and then estimate the electron bounce period in a similar fashion to the analysis in Ch. 3. The empirical bounce period can then be compared to modeled bounce periods from a variety of magnetic field models, and then model accuracy estimated. Identifying the bouncing packet microbursts is not easy, but may be possible with an auto-correlation or machine learning approaches e.g. a neural network.

The last project described here that can be done with existing data is to test the hypothesis that curtains, which were briefly described in Ch. 4, are remnants of microbursts in the drift loss cone. One way to test this hypothesis is to look for the occurrence rates of curtains eastward and westward of the SAA. If curtains are electrons in the drift loss cone then the SAA will remove curtains as they drift to the east. Thus under the proposed hypothesis the number of curtains should be greater just to the west of the SAA than to the east. An alternative approach to test this hypothesis is to estimate how each curtain's flux changes between the two AC6 units. If curtains are drifting and have a falling energy spectra, then the larger number of slower-drifting, low energy, electrons will appear as an enhancement in the flux for the trailing spacecraft. If such a trend is apparent then curtains must be drifting, otherwise they may be actively scattered in the same location.

### Future missions

A few upcoming missions are dedicated to study microbursts and would be able to address some of the unknown questions raised in this dissertation and discussed below.

One approach to determine if microburst scattering is a diffusive or a non-linear process can be done in LEO where the transport of microburst electrons inside the loss cone can be more easily observed. In contrast to particle measurements made near the magnetic equator where the local loss cone is only a few degrees, the loss cone in LEO is  $\approx 60^\circ$  which is much easier to resolve with an instrument with multiple look directions. With this measurement, different scattering mechanisms can be studied. If the scattering process is diffusive, then the microburst flux will be monotonically decreasing (or flat) deeper into the loss cone. A non-linear scattering process, on the other hand, will have a more complex pitch angle vs flux profile e.g. a relative maximum at  $0^\circ$ , followed by decreasing flux towards the loss cone boundary. One mission that plans to make this measurement is The Relativistic Electron Atmospheric Loss (REAL) CubeSat. This CubeSat, planned to launch in 2021, will sample the inside and outside of the loss cone with a solid state detector with a five look directions.

As previously mentioned, the unknown microburst shape makes microburst size comparisons between balloons and satellites ambiguous. One of the most feasible ways to resolve this ambiguity is to image microburst precipitation in the upper atmosphere using a balloon. This imaging is possible because when microburst electrons impact the atmosphere, they scatter with Earth's atmosphere and generate bremsstrahlung X-rays. These X-rays have a relatively long mean free path at  $\approx 35$  km balloon altitudes so a balloon-borne imager will predominately observe primary X-rays emitted directly from the microburst electrons. This idea is the basis for the

upcoming Balloon Observations Of Microburst Scales (BOOMS) mission. BOOMS will fly a set of X-ray pinhole imagers containing a scintillator crystal (to convert from X-rays to visible light) and a grid of photomultiplier tubes (PMT) underneath to record the distribution of light. The distribution of light across the grid of PMTs, together with instrument modeling, can be used to convert between the PMT signal and the angular position for each observed X-ray. Over a longer exposure, a probabilistic image can then be constructed of the microburst X-ray source. Then the microburst shape, and any spatial correlations of trains of microbursts can be observed.

REFERENCES CITED

## Bibliography

- Abel, B. and Thorne, R. M. (1998). Electron scattering loss in earth's inner magnetosphere: 1. dominant physical processes. *Journal of Geophysical Research: Space Physics*, 103(A2):2385–2396.
- Agapitov, O., Blum, L. W., Mozer, F. S., Bonnell, J. W., and Wygant, J. (2017). Chorus whistler wave source scales as determined from multipoint van allen probe measurements. *Geophysical Research Letters*, pages n/a–n/a. 2017GL072701.
- Agapitov, O., Krasnoselskikh, V., Dudok de Wit, T., Khotyaintsev, Y., Pickett, J. S., Santolik, O., and Rolland, G. (2011). Multispacecraft observations of chorus emissions as a tool for the plasma density fluctuations' remote sensing. *Journal of Geophysical Research: Space Physics*, 116(A9):n/a–n/a. A09222.
- Agapitov, O., Krasnoselskikh, V., Zaliznyak, Y., Angelopoulos, V., Le Contel, O., and Rolland, G. (2010). Chorus source region localization in the earth's outer magnetosphere using themis measurements. *Annales Geophysicae*, 28(6):1377–1386.
- Agapitov, O., Mourenas, D., Artemyev, A., Mozer, F., Bonnell, J., Angelopoulos, V., Shastun, V., and Krasnoselskikh, V. (2018). Spatial extent and temporal correlation of chorus and hiss: Statistical results from multipoint themis observations. *Journal of Geophysical Research: Space Physics*, 123(10):8317–8330.
- Anderson, B., Shekhar, S., Millan, R., Crew, A., Spence, H., Klumpar, D., Blake, J., O'Brien, T., and Turner, D. (2017). Spatial scale and duration of one microburst region on 13 August 2015. *Journal of Geophysical Research: Space Physics*.
- Anderson, K. A. and Milton, D. W. (1964). Balloon observations of X rays in the auroral zone: 3. High time resolution studies. *Journal of Geophysical Research*, 69(21):4457–4479.
- Barcus, J., Brown, R., and Rosenberg, T. (1966). Spatial and temporal character of fast variations in auroral-zone x rays. *Journal of Geophysical Research*, 71(1):125–141.
- Baumjohann, W. and Treumann, R. A. (1997). *Basic space plasma physics*. World Scientific.
- Blake, J., Carranza, P., Claudepierre, S., Clemons, J., Crain, W., Dotan, Y., Fennell, J., Fuentes, F., Galvan, R., George, J., et al. (2013). The magnetic electron ion spectrometer (MagEIS) instruments aboard the radiation belt storm probes (RBSP) spacecraft. *Space Science Reviews*, 179(1-4):383–421.

- Blake, J., Looper, M., Baker, D., Nakamura, R., Klecker, B., and Hovestadt, D. (1996). New high temporal and spatial resolution measurements by sampex of the precipitation of relativistic electrons. *Advances in Space Research*, 18(8):171 – 186.
- Blake, J. B. and O'Brien, T. P. (2016). Observations of small-scale latitudinal structure in energetic electron precipitation. *Journal of Geophysical Research: Space Physics*, 121(4):3031–3035. 2015JA021815.
- Blum, L., Li, X., and Denton, M. (2015). Rapid MeV electron precipitation as observed by SAMPEX/HILT during high-speed stream-driven storms. *Journal of Geophysical Research: Space Physics*, 120(5):3783–3794. 2014JA020633.
- Bortnik, J., Thorne, R., and Inan, U. S. (2008). Nonlinear interaction of energetic electrons with large amplitude chorus. *Geophysical Research Letters*, 35(21).
- Boscher, D., Bourdarie, S., O'Brien, P., Guild, T., and Shumko, M. (2012). Irbem-lib library.
- Breneman, A., Crew, A., Sample, J., Klumpar, D., Johnson, A., Agapitov, O., Shumko, M., Turner, D., Santolik, O., Wygant, J., et al. (2017). Observations directly linking relativistic electron microbursts to whistler mode chorus: Van allen probes and FIREBIRD II. *Geophysical Research Letters*.
- Breneman, A. W., Halford, A., Millan, R., McCarthy, M., Fennell, J., Sample, J., Woodger, L., Hospodarsky, G., Wygant, J. R., Cattell, C. A., et al. (2015). Global-scale coherence modulation of radiation-belt electron loss from plasmaspheric hiss. *Nature*, 523(7559):193.
- Brown, R., Barcus, J., and Parsons, N. (1965). Balloon observations of auroral zone x rays in conjugate regions. 2. microbursts and pulsations. *Journal of Geophysical Research (U.S.)*.
- Capannolo, L., Li, W., Ma, Q., Shen, X.-C., Zhang, X.-J., Redmon, R., Rodriguez, J., Engebretson, M., Kletzing, C., Kurth, W., et al. (2019). Energetic electron precipitation: multi-event analysis of its spatial extent during emic wave activity. *Journal of Geophysical Research: Space Physics*.
- Claudepierre, S., O'Brien, T., Looper, M., Blake, J., Fennell, J., Roeder, J., Clemons, J., Mazur, J., Turner, D., Reeves, G., et al. (2019). A revised look at relativistic electrons in the earth's inner radiation zone and slot region. *Journal of Geophysical Research: Space Physics*, 124(2):934–951.
- Comess, M., Smith, D., Selesnick, R., Millan, R., and Sample, J. (2013). Duskside relativistic electron precipitation as measured by sampex: A statistical survey. *Journal of Geophysical Research: Space Physics*, 118(8):5050–5058.

- Crew, A. B., Spence, H. E., Blake, J. B., Klumpar, D. M., Larsen, B. A., O'Brien, T. P., Driscoll, S., Handley, M., Legere, J., Longworth, S., Mashburn, K., Mosleh, E., Ryhajlo, N., Smith, S., Springer, L., and Widholm, M. (2016). First multipoint in situ observations of electron microbursts: Initial results from the NSF FIREBIRD II mission. *Journal of Geophysical Research: Space Physics*, 121(6):5272–5283. 2016JA022485.
- Datta, S., Skoug, R., McCarthy, M., and Parks, G. (1997). Modeling of microburst electron precipitation using pitch angle diffusion theory. *Journal of Geophysical Research: Space Physics*, 102(A8):17325–17333.
- Dietrich, S., Rodger, C. J., Clilverd, M. A., Bortnik, J., and Raita, T. (2010). Relativistic microburst storm characteristics: Combined satellite and ground-based observations. *Journal of Geophysical Research: Space Physics*, 115(A12).
- Douma, E., Rodger, C., Blum, L., O'Brien, T., Clilverd, M., and Blake, J. (2019). Characteristics of relativistic microburst intensity from sampex observations. *Journal of Geophysical Research: Space Physics*.
- Douma, E., Rodger, C. J., Blum, L. W., and Clilverd, M. A. (2017). Occurrence characteristics of relativistic electron microbursts from SAMPEX observations. *Journal of Geophysical Research: Space Physics*, 122(8):8096–8107. 2017JA024067.
- Eastwood, J., Hietala, H., Toth, G., Phan, T., and Fujimoto, M. (2015). What controls the structure and dynamics of earths magnetosphere? *Space Science Reviews*, 188(1-4):251–286.
- Fang, X., Randall, C. E., Lummerzheim, D., Wang, W., Lu, G., Solomon, S. C., and Frahm, R. A. (2010). Parameterization of monoenergetic electron impact ionization. *Geophysical Research Letters*, 37(22).
- Funsten, H., Skoug, R., Guthrie, A., MacDonald, E., Baldonado, J., Harper, R., Henderson, K., Kihara, K., Lake, J., Larsen, B., et al. (2013). Helium, Oxygen, Proton, and Electron (HOPE) mass spectrometer for the radiation belt storm probes mission. *Space Science Reviews*, 179(1-4):423–484.
- Greeley, A., Kanekal, S., Baker, D., Klecker, B., and Schiller, Q. (2019). Quantifying the contribution of microbursts to global electron loss in the radiation belts. *Journal of Geophysical Research: Space Physics*.
- Gurnett, D., Anderson, R., Scarf, F., Fredricks, R., and Smith, E. (1979). Initial results from the iese-1 and-2 plasma wave investigation. *Space Science Reviews*, 23(1):103–122.
- Hastings, W. K. (1970). Monte carlo sampling methods using markov chains and their applications.

- Hendry, A. T., Rodger, C. J., and Clilverd, M. A. (2017). Evidence of sub-mev emic-driven electron precipitation. *Geophysical Research Letters*, 44(3):1210–1218.
- Hoots, F. R. and Roehrich, R. L. (1980). Models for propagation of norad element sets. Technical Report 3, Spacetrack.
- Horne, R., Glauert, S., Meredith, N., Boscher, D., Maget, V., Heynderickx, D., and Pitchford, D. (2013). Space weather impacts on satellites and forecasting the earth's electron radiation belts with spacecast. *Space Weather*, 11(4):169–186.
- Horne, R., Glauert, S., and Thorne, R. (2003a). Resonant diffusion of radiation belt electrons by whistler-mode chorus. *Geophysical research letters*, 30(9).
- Horne, R., Thorne, R., Meredith, N., and Anderson, R. (2003b). Diffuse auroral electron scattering by electron cyclotron harmonic and whistler mode waves during an isolated substorm. *Journal of Geophysical Research: Space Physics*, 108(A7).
- Horne, R. B. and Thorne, R. M. (2003). Relativistic electron acceleration and precipitation during resonant interactions with whistler-mode chorus. *Geophysical Research Letters*, 30(10). 1527.
- Horne, R. B., Thorne, R. M., Shprits, Y. Y., Meredith, N. P., Glauert, S. A., Smith, A. J., Kanekal, S. G., Baker, D. N., Engebretson, M. J., Posch, J. L., et al. (2005). Wave acceleration of electrons in the van allen radiation belts. *Nature*, 437(7056):227.
- Joy, S., Kivelson, M., Walker, R., Khurana, K., Russell, C., and Ogino, T. (2002). Probabilistic models of the jovian magnetopause and bow shock locations. *Journal of Geophysical Research: Space Physics*, 107(A10):SMP–17.
- Kasahara, S., Miyoshi, Y., Yokota, S., Mitani, T., Kasahara, Y., Matsuda, S., Kumamoto, A., Matsuoka, A., Kazama, Y., Frey, H., et al. (2018). Pulsating aurora from electron scattering by chorus waves. *Nature*, 554(7692):337.
- Kletzing, C., Kurth, W., Acuna, M., MacDowall, R., Torbert, R., Averkamp, T., Bodet, D., Bounds, S., Chutter, M., Connerney, J., et al. (2013). The electric and magnetic field instrument suite and integrated science (EMFISIS) on RBSP. *Space Science Reviews*, 179(1-4):127–181.
- Klumpar, D., Springer, L., Mosleh, E., Mashburn, K., Berardinelli, S., Gunderson, A., Handly, M., Ryhajlo, N., Spence, H., Smith, S., Legere, J., Widholm, M., Longworth, S., Crew, A., Larsen, B., Blake, J., and Walmsley, N. (2015). Flight system technologies enabling the twin-cubesat firebird-ii scientific mission.
- Lee, J. J., Parks, G. K., Lee, E., Tsurutani, B. T., Hwang, J., Cho, K. S., Kim, K.-H., Park, Y. D., Min, K. W., and McCarthy, M. P. (2012). Anisotropic pitch angle

distribution of 100 keV microburst electrons in the loss cone: measurements from STSAT-1. *Annales Geophysicae*, 30(11):1567–1573.

Lee, J.-J., Parks, G. K., Min, K. W., Kim, H. J., Park, J., Hwang, J., McCarthy, M. P., Lee, E., Ryu, K. S., Lim, J. T., Sim, E. S., Lee, H. W., Kang, K. I., and Park, H. Y. (2005). Energy spectra of 170–360 keV electron microbursts measured by the korean STSAT-1. *Geophysical Research Letters*, 32(13). L13106.

Li, W., Thorne, R., Angelopoulos, V., Bonnell, J., McFadden, J., Carlson, C., LeContel, O., Roux, A., Glassmeier, K., and Auster, H. (2009a). Evaluation of whistler-mode chorus intensification on the nightside during an injection event observed on the THEMIS spacecraft. *Journal of Geophysical Research: Space Physics*, 114(A1).

Li, W., Thorne, R., Bortnik, J., Tao, X., and Angelopoulos, V. (2012). Characteristics of hiss-like and discrete whistler-mode emissions. *Geophysical Research Letters*, 39(18).

Li, W., Thorne, R. M., Angelopoulos, V., Bortnik, J., Cully, C. M., Ni, B., LeContel, O., Roux, A., Auster, U., and Magnes, W. (2009b). Global distribution of whistler-mode chorus waves observed on the THEMIS spacecraft. *Geophysical Research Letters*, 36(9). L09104.

Li, X., Selesnick, R., Schiller, Q., Zhang, K., Zhao, H., Baker, D. N., and Temerin, M. A. (2017). Measurement of electrons from albedo neutron decay and neutron density in near-earth space. *Nature*, 552(7685):382.

Lorentzen, K. R., Blake, J. B., Inan, U. S., and Bortnik, J. (2001a). Observations of relativistic electron microbursts in association with VLF chorus. *Journal of Geophysical Research: Space Physics*, 106(A4):6017–6027.

Lorentzen, K. R., Looper, M. D., and Blake, J. B. (2001b). Relativistic electron microbursts during the GEM storms. *Geophysical Research Letters*, 28(13):2573–2576.

Lyons, L. R. and Thorne, R. M. (1973). Equilibrium structure of radiation belt electrons. *Journal of Geophysical Research*, 78(13):2142–2149.

Manweiler, J. W. and Zwiener, H. M. (2018). Science Operations Center (SOC) RBSPICE Science Data Handbook Revision: e. Technical report, Fundamental Technologies, LLC.

Mauk, B., Fox, N. J., Kanekal, S., Kessel, R., Sibeck, D., and Ukhorskiy, A. (2013). Science objectives and rationale for the radiation belt storm probes mission. *Space Science Reviews*, 179(1-4):3–27.

- Meredith, N., Horne, R., Summers, D., Thorne, R., Iles, R., Heynderickx, D., and Anderson, R. (2002). Evidence for acceleration of outer zone electrons to relativistic energies by whistler mode chorus. In *Annales Geophysicae*, volume 20, pages 967–979.
- Metropolis, N., Rosenbluth, A. W., Rosenbluth, M. N., Teller, A. H., and Teller, E. (1953). Equation of state calculations by fast computing machines. *The journal of chemical physics*, 21(6):1087–1092.
- Millan, R. and Thorne, R. (2007). Review of radiation belt relativistic electron losses. *Journal of Atmospheric and Solar-Terrestrial Physics*, 69(3):362 – 377.
- Millan, R. M., Lin, R., Smith, D., Lorentzen, K., and McCarthy, M. (2002). X-ray observations of mev electron precipitation with a balloon-borne germanium spectrometer. *Geophysical research letters*, 29(24).
- Mitchell, D., Lanzerotti, L., Kim, C., Stokes, M., Ho, G., Cooper, S., Ukhorskiy, A., Manweiler, J., Jaskulek, S., Haggerty, D., et al. (2013). Radiation belt storm probes ion composition experiment (RBSPICE). *Space Science Reviews*, 179(1-4):263–308.
- Mozer, F. S., Agapitov, O. V., Blake, J. B., and Vasko, I. Y. (2018). Simultaneous observations of lower band chorus emissions at the equator and microburst precipitating electrons in the ionosphere. *Geophysical Research Letters*.
- Nakamura, R., Baker, D. N., Blake, J. B., Kanekal, S., Klecker, B., and Hovestadt, D. (1995). Relativistic electron precipitation enhancements near the outer edge of the radiation belt. *Geophysical Research Letters*, 22(9):1129–1132.
- Nakamura, R., Isowa, M., Kamide, Y., Baker, D., Blake, J., and Looper, M. (2000). Observations of relativistic electron microbursts in association with VLF chorus. *J. Geophys. Res.*, 105:15875–15885.
- Nishimura, Y., Bortnik, J., Li, W., Thorne, R., Chen, L., Lyons, L., Angelopoulos, V., Mende, S., Bonnell, J., Le Contel, O., et al. (2011). Multievent study of the correlation between pulsating aurora and whistler mode chorus emissions. *Journal of Geophysical Research: Space Physics*, 116(A11).
- O'Brien, T., Claudepierre, S., Blake, J., Fennell, J. F., Clemons, J., Roeder, J., Spence, H. E., Reeves, G., and Baker, D. (2014). An empirically observed pitch-angle diffusion eigenmode in the earth's electron belt near  $l^*= 5.0$ . *Geophysical Research Letters*, 41(2):251–258.
- O'Brien, T., Claudepierre, S., Guild, T., Fennell, J., Turner, D., Blake, J., Clemons, J., and Roeder, J. (2016a). Inner zone and slot electron radial diffusion revisited. *Geophysical Research Letters*, 43(14):7301–7310.

- O'Brien, T. and Moldwin, M. (2003). Empirical plasmapause models from magnetic indices. *Geophysical Research Letters*, 30(4).
- O'Brien, T. P., Blake, J. B., and W., G. J. (2016b). Aerocene-6 dosimeter data readme. Technical Report TOR-2016-01155, The Aerospace Corporation.
- O'Brien, T. P.,Looper, M. D., and Blake, J. B. (2004). Quantification of relativistic electron microburst losses during the GEM storms. *Geophysical Research Letters*, 31(4). L04802.
- O'Brien, T. P., Lorentzen, K. R., Mann, I. R., Meredith, N. P., Blake, J. B., Fennell, J. F., Looper, M. D., Milling, D. K., and Anderson, R. R. (2003). Energization of relativistic electrons in the presence of ULF power and MeV microbursts: Evidence for dual ULF and VLF acceleration. *Journal of Geophysical Research: Space Physics*, 108(A8).
- Olson, W. P. and Pfitzer, K. A. (1982). A dynamic model of the magnetospheric magnetic and electric fields for july 29, 1977. *Journal of Geophysical Research: Space Physics*, 87(A8):5943–5948.
- Ozaki, M., Miyoshi, Y., Shiokawa, K., Hosokawa, K., Oyama, S.-i., Kataoka, R., Ebihara, Y., Ogawa, Y., Kasahara, Y., Yagitani, S., et al. (2019). Visualization of rapid electron precipitation via chorus element wave–particle interactions. *Nature communications*, 10(1):257.
- Ozaki, M., Yagitani, S., Ishizaka, K., Shiokawa, K., Miyoshi, Y., Kadokura, A., Yamagishi, H., Kataoka, R., Ieda, A., Ebihara, Y., Sato, N., and Nagano, I. (2012). Observed correlation between pulsating aurora and chorus waves at Syowa Station in Antarctica: A case study. *Journal of Geophysical Research: Space Physics*, 117(A8).
- Parks, G. (2003). *Physics Of Space Plasmas: An Introduction, Second Edition*. Westview Press.
- Parks, G. K. (1967). Spatial characteristics of auroral-zone X-ray microbursts. *Journal of Geophysical Research*, 72(1):215–226.
- Reeves, G., Spence, H. E., Henderson, M., Morley, S., Friedel, R., Funsten, H., Baker, D., Kanekal, S., Blake, J., Fennell, J., et al. (2013). Electron acceleration in the heart of the van allen radiation belts. *Science*, 341(6149):991–994.
- Reeves, G. D., McAdams, K. L., Friedel, R. H. W., and O'Brien, T. P. (2003). Acceleration and loss of relativistic electrons during geomagnetic storms. *Geophysical Research Letters*, 30(10):n/a–n/a. 1529.

- Sambridge, M., Gallagher, K., Jackson, A., and Rickwood, P. (2006). Trans-dimensional inverse problems, model comparison and the evidence. *Geophysical Journal International*, 167(2):528–542.
- Santolik, O., Gurnett, D., Pickett, J., Parrot, M., and Cornilleau-Wehrlin, N. (2003). Spatio-temporal structure of storm-time chorus. *Journal of Geophysical Research: Space Physics*, 108(A7).
- Santolk, O., Parrot, M., and Lefevre, F. (2003). Singular value decomposition methods for wave propagation analysis. *Radio Science*, 38(1):n/a–n/a. 1010.
- Schulz, M. and Lanzerotti, L. J. (1974). *Particle Diffusion in the Radiation Belts*. Springer.
- Selesnick, R. S., Blake, J. B., and Mewaldt, R. A. (2003). Atmospheric losses of radiation belt electrons. *Journal of Geophysical Research: Space Physics*, 108(A12). 1468.
- Seppälä, A., Douma, E., Rodger, C., Verronen, P., Clilverd, M. A., and Bortnik, J. (2018). Relativistic electron microburst events: Modeling the atmospheric impact. *Geophysical Research Letters*, 45(2):1141–1147.
- Sharma, S. (2017). Markov chain monte carlo methods for bayesian data analysis in astronomy. *Annual Review of Astronomy and Astrophysics*, 55:213–259.
- Shprits, Y. Y., Meredith, N. P., and Thorne, R. M. (2007). Parameterization of radiation belt electron loss timescales due to interactions with chorus waves. *Geophysical Research Letters*, 34(11):n/a–n/a. L11110.
- Shprits, Y. Y. and Thorne, R. M. (2004). Time dependent radial diffusion modeling of relativistic electrons with realistic loss rates. *Geophysical Research Letters*, 31(8):n/a–n/a. L08805.
- Shumko, M., Sample, J., Johnson, A., Blake, B., Crew, A., Spence, H., Klumpar, D., Agapitov, O., and Handley, M. (2018). Microburst scale size derived from multiple bounces of a microburst simultaneously observed with the firebird-ii cubesats. *Geophysical Research Letters*, 45(17):8811–8818.
- Spence, H. E., Blake, J. B., Crew, A. B., Driscoll, S., Klumpar, D. M., Larsen, B. A., Legere, J., Longworth, S., Mosleh, E., O'Brien, T. P., Smith, S., Springer, L., and Widholm, M. (2012). Focusing on size and energy dependence of electron microbursts from the van allen radiation belts. *Space Weather*, 10(11).
- Summers, D. (2005). Quasi-linear diffusion coefficients for field-aligned electromagnetic waves with applications to the magnetosphere. *Journal of Geophysical Research: Space Physics*, 110(A8):n/a–n/a. A08213.

- Summers, D., Thorne, R. M., and Xiao, F. (1998). Relativistic theory of wave-particle resonant diffusion with application to electron acceleration in the magnetosphere. *Journal of Geophysical Research: Space Physics*, 103(A9):20487–20500.
- Takahashi, K. and Denton, R. E. (2007). Magnetospheric seismology using multi-harmonic toroidal waves observed at geosynchronous orbit. *Journal of Geophysical Research: Space Physics*, 112(A5).
- Thorne, R. M. (2010). Radiation belt dynamics: The importance of wave-particle interactions. *Geophysical Research Letters*, 37(22). L22107.
- Thorne, R. M. and Andreoli, L. J. (1981). *Mechanisms for Intense Relativistic Electron Precipitation*, pages 381–394. Springer Netherlands, Dordrecht.
- Thorne, R. M., O'Brien, T. P., Shprits, Y. Y., Summers, D., and Horne, R. B. (2005). Timescale for MeV electron microburst loss during geomagnetic storms. *Journal of Geophysical Research: Space Physics*, 110(A9). A09202.
- Trefall, H., Bjordal, J., Ullaland, S., and Stadsnes, J. (1966). On the extension of auroral-zone x-ray microbursts. *Journal of Atmospheric and Terrestrial Physics*, 28(2):225–233.
- Tsurutani, B. T. and Lakhina, G. S. (1997). Some basic concepts of wave-particle interactions in collisionless plasmas. *Reviews of Geophysics*, 35(4):491–501.
- Tsurutani, B. T., Lakhina, G. S., and Verkhoglyadova, O. P. (2013). Energetic electron ( $\gtrsim 10$  kev) microburst precipitation,  $\sim 5\text{--}15$  s x-ray pulsations, chorus, and wave-particle interactions: A review. *Journal of Geophysical Research: Space Physics*, 118(5):2296–2312.
- Tsyganenko, N. (1989). A solution of the chapman-ferraro problem for an ellipsoidal magnetopause. *Planetary and Space Science*, 37(9):1037 – 1046.
- Tsyganenko, N. A. and Sitnov, M. I. (2005). Modeling the dynamics of the inner magnetosphere during strong geomagnetic storms. *Journal of Geophysical Research: Space Physics*, 110(A3).
- Turner, D., Lee, J., Claudepierre, S., Fennell, J., Blake, J., Jaynes, A., Leonard, T., Wilder, F., Ergun, R., Baker, D., et al. (2017). Examining coherency scales, substructure, and propagation of whistler mode chorus elements with magnetospheric multiscale (mms). *Journal of Geophysical Research: Space Physics*, 122(11).
- Ukhorskiy, A. Y., Anderson, B. J., Brandt, P. C., and Tsyganenko, N. A. (2006). Storm time evolution of the outer radiation belt: Transport and losses. *Journal of Geophysical Research: Space Physics*, 111(A11):n/a–n/a. A11S03.

- Van Allen, J. A. (1959). The geomagnetically trapped corpuscular radiation. *Journal of Geophysical Research*, 64(11):1683–1689.
- Vernov, S. and Chudakov, A. (1960). Investigation of radiation in outer space. In *International Cosmic Ray Conference*, volume 3, page 19.
- Walker, A. D. M. (1993). *Plasma waves in the magnetosphere*, volume 24. Springer Science & Business Media.
- Woodger, L., Halford, A., Millan, R., McCarthy, M., Smith, D., Bowers, G., Sample, J., Anderson, B., and Liang, X. (2015). A summary of the BARREL campaigns: Technique for studying electron precipitation. *Journal of Geophysical Research: Space Physics*, 120(6):4922–4935.

## APPENDICES

APPENDIX A

WAVE PROPERTIES OBSERVED BY EMFISIS AND PITCH ANGLE EXTENT  
OF MICROBURST

This appendix contains Figs. A.1 and A.2. Figure A.1 shows evidence that supports our claim that the “hiss-like” chorus wave observed at 11:17:03 UT with EMFISIS WFR instrument on RBSP-A was parallel propagating. The polar angle of the wave vector and the supporting planarity of the magnetic field polarization shown in Fig. A.1 was calculated using the singular value decomposition (SVD) method (Santolk et al., 2003).

Figure A.2 supports the claim that RBSPICE-A observed a 10-80% increase in the count rates at the microburst times and pitch angles. Figure A.2 shows the ratio of the RBSPICE-A’s EBR count rates during the four microbursts to the quiet time one spin before, at the same pitch angles.

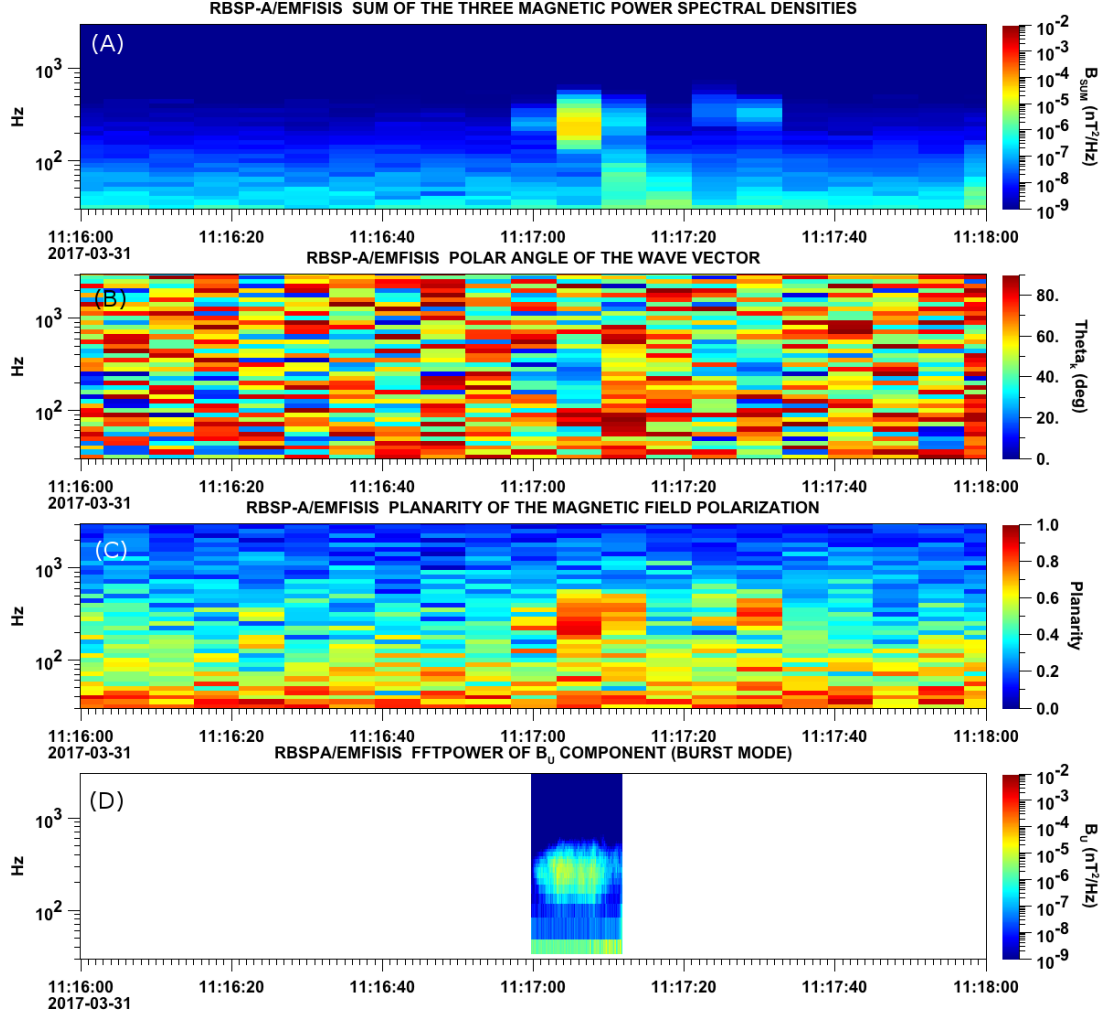


Figure A.1: Panel (A) shows the magnetic power spectral density as a function of frequency and time from the EMFISIS WFR instrument on board RBSP-A. The “hiss-like” wave used for the resonant diffusion analysis was observed starting at 11:17:03 UT. In the same format as panel (A), panel (B) shows the polar angle of the wave vector for this time period. The wave of interest had a normal wave vector,  $\theta_k < 30^\circ$ . Since the results in panel (B) are valid only for high planarity, panel (C) shows planarity in the same format as panels (A) and (B). The wave of interest was found to have a planarity of  $> 0.8$ . Lastly, panel (D) shows the available burst mode data.

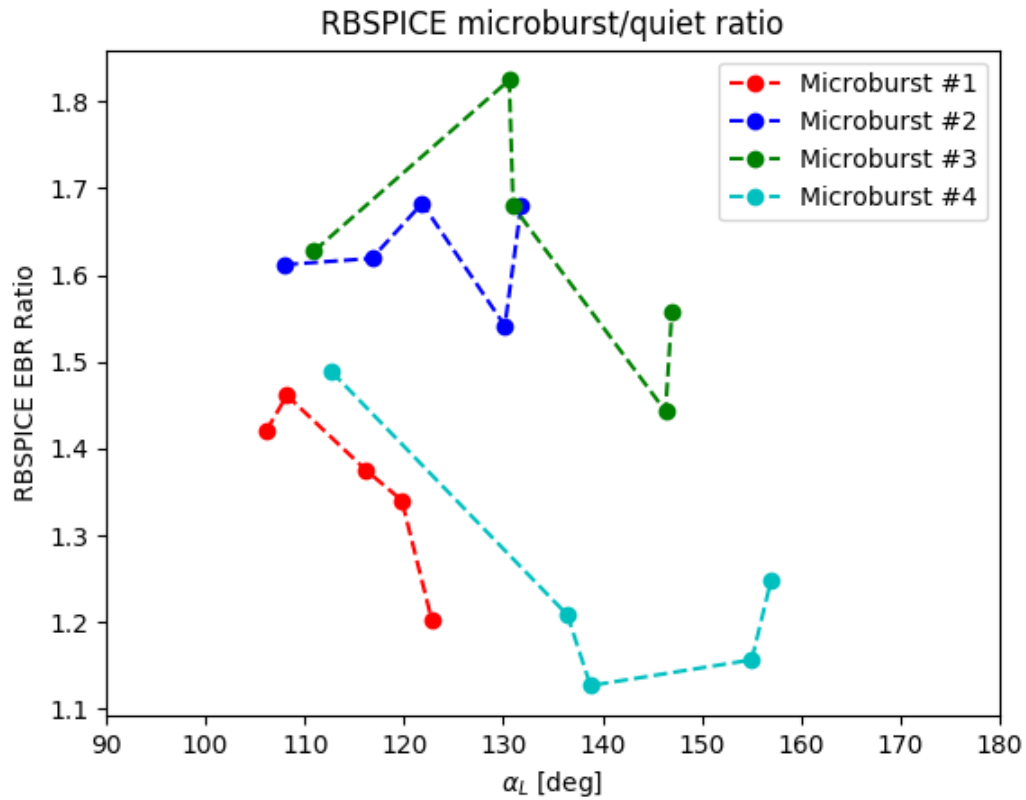


Figure A.2: Ratio of the RBSPICE EBR at microburst times indicated with the black vertical arrows in Fig. 2, to the EBR at the same pitch angles one spin prior (quiet time). The microburst flux was enhanced by 10-80% across  $100^\circ < \alpha_L < 160^\circ$  PA, and appear to be peaked closer to  $\alpha_L = 90^\circ$ .

APPENDIX B

ESTIMATING THE CLOCK ERROR AND SEPARATION ON FIREBIRD-II

This appendix describes the method we used to calculate the time difference and separation between FU3 and FU4 at 06:12 UT on February 2nd, 2015. We used the following method to calculate the clock difference,  $\delta t_c$  and separation,  $d$  between FU3 and FU4 at 06:12 UT on February 2nd, 2015.

The relative clock difference was calculated with a cross-correlation time lag analysis on uniquely-identified trains of microbursts that hit both spacecraft simultaneously. Four time periods with coincident microbursts were hand-picked on February 2nd, 2015 and are shown in Figs. B.1-B.4, panels (a) and (b). The cross-correlation time lag analysis was applied to the HiRes time series in panels (a) and (b), and the resulting normalized cross-correlation coefficient as a function of time is shown in panel (c). To validate the peak lag identified in panel (c), FU3's time series was shifted by that lag and is shown in panel (d).

The clock differences from the simultaneous microbursts in Figs. B.1-B.4 were linearly fit to account for the relative clock drift ( $\approx 20$  ms/hour at this time), giving a value of  $\delta t_c = 2.28 \pm 0.12$  s at the time of the microburst analyzed here. This time shift was applied to the HiRes data in Fig. 1. A clock difference of  $\delta t_c = 2.45^{+0.51}_{-0.98}$  s was independently calculated with the FIREBIRD-II telemetry beacon time stamps that were downlinked during operational passes.

We calculate the spacecraft separation, by applying same the cross-correlation time lag analysis on structures assumed to be spatial and are shown in Figs. B.5 and B.6. The lag from the peak cross-correlation between these events is a sum of the clock difference and time lag due to the spacecraft separation. We interpret the time lag due to the spacecraft separation as the time difference between when the leading satellite observed a stationary spatial feature, to when the trailing satellite observed the same stationary spatial feature. With the method described above, we find the spatial time lag to be  $\delta t_d = 2.64 \pm 0.12$  s (after we account for the clock difference and its uncertainty). To convert from a spatial time lag to a spacecraft separation, we calculate the satellite velocity. We calculate the velocity using a Two Line Element (TLE), a data format containing the orbit parameters that are used for orbit propagation. With the TLE derived spacecraft velocity,  $v = 7.57$  km/s, the spacecraft separation was  $d = 19.9 \pm 0.9$  km.

An independent method to calculate the spacecraft separation was developed. The separation was calculated using TLEs. The TLE from February 2nd was anomalous and was not used in this analysis. Instead, seven TLEs released up to five days after the microburst event were backpropagated, using the SGP-4 algorithm (Hoots and Roehrich, 1980) that calculates orbital state vectors with perturbations such as Earth's atmosphere, as well as gravitational effects from the moon and sun. Then the predicted spacecraft separations at the time of the microburst event were averaged to derive a separation of  $d = 18.4 \pm 1.5$  km. These two methods give similar separations, which implies that the stationary event assumption used in the cross-correlation time lag analysis is reasonable.

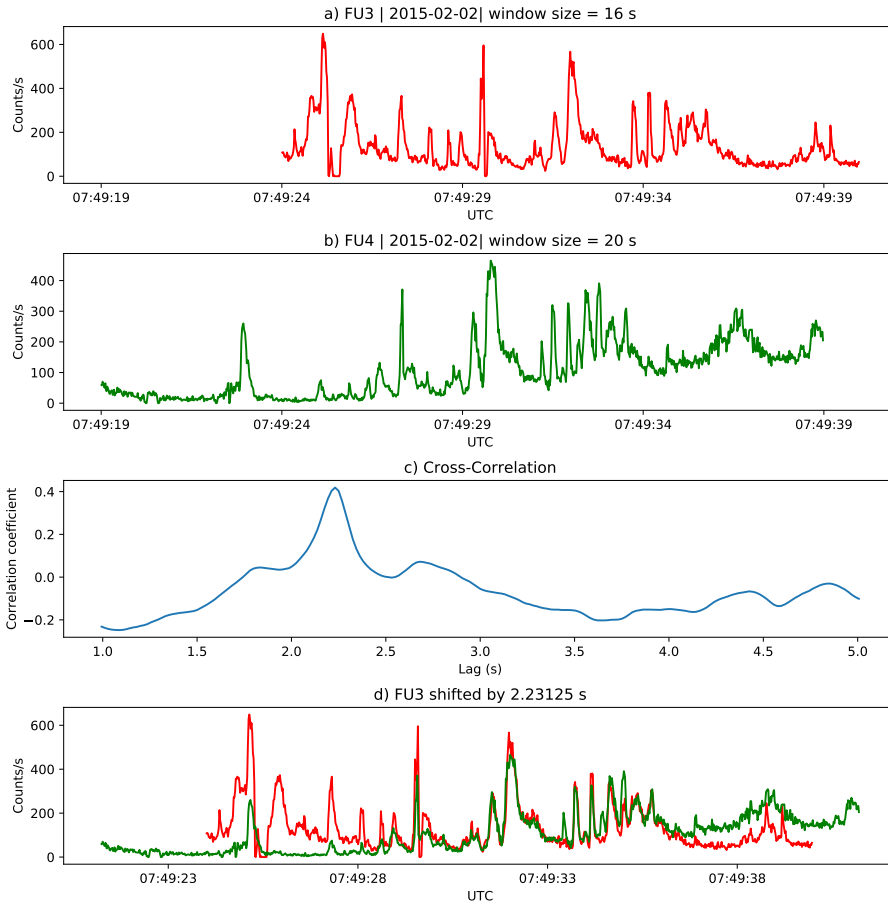


Figure B.1: Cross-correlation time lag analysis applied to a train of microbursts. Panel (a) and (b) show the count rate from the lowest energy channel. Panel (c) shows the cross-correlation coefficient as a function of time lag. Panel (d) shows the shifted timeseries. Clock difference was 2.23 s.

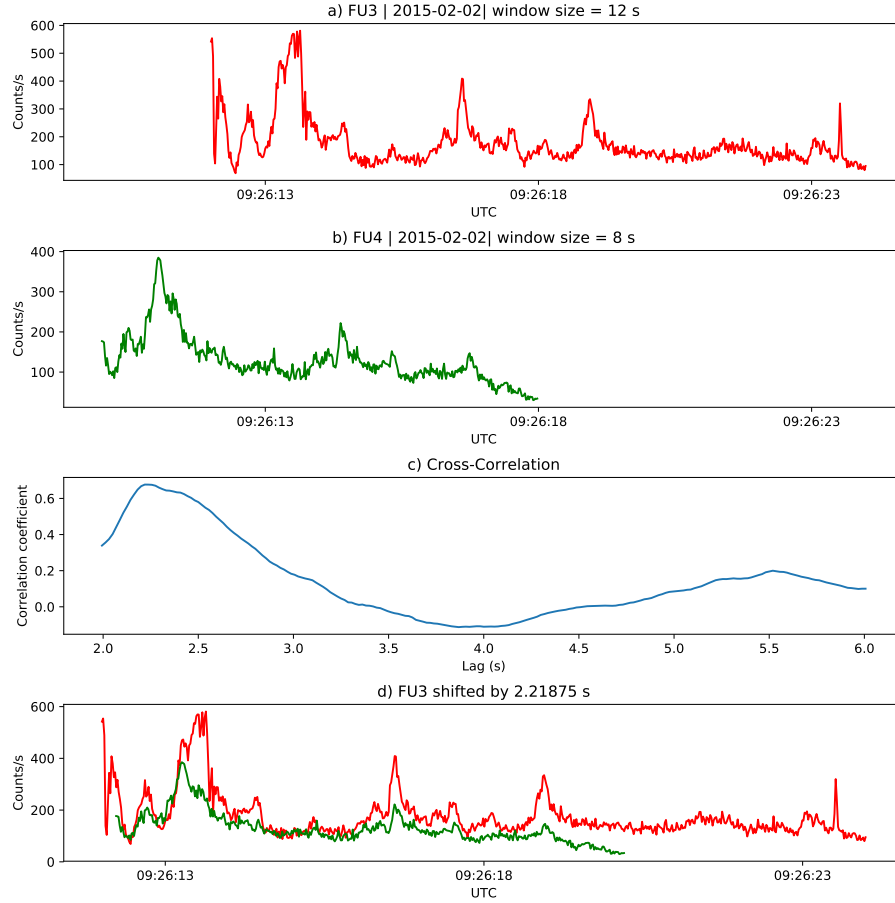


Figure B.2: Same analysis as Fig. B.1 on a different time period. Clock difference was 2.21 s.

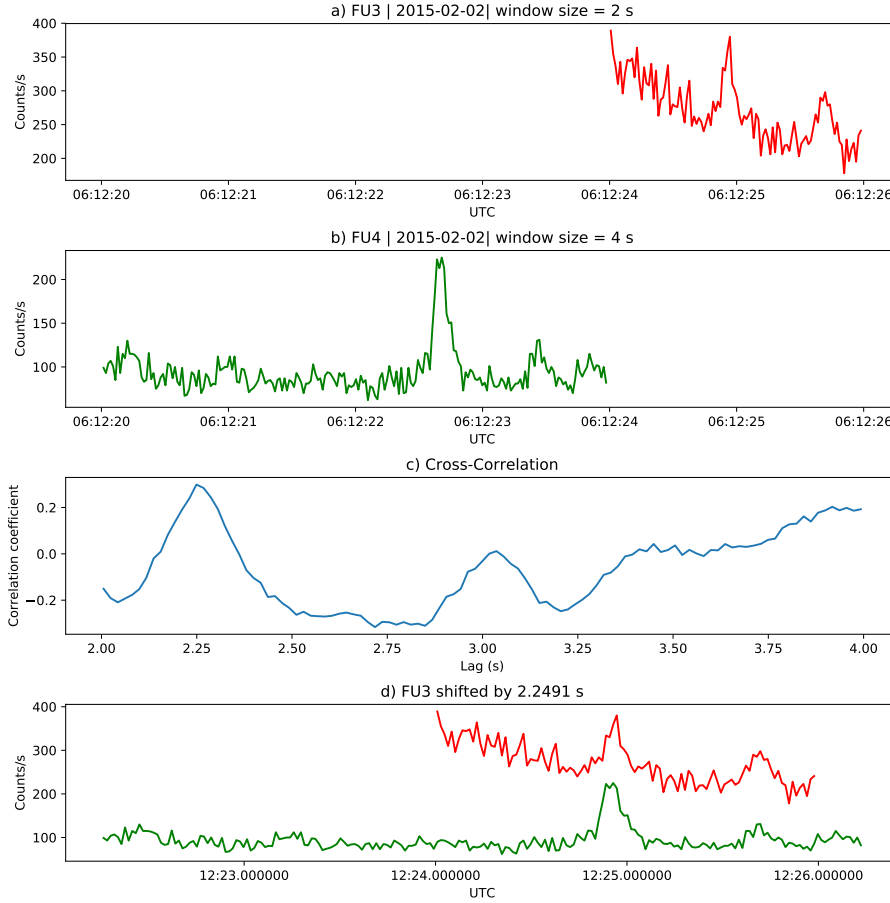


Figure B.3: Same analysis as Fig. B.1 on a different time period. Clock difference was 2.25 s.

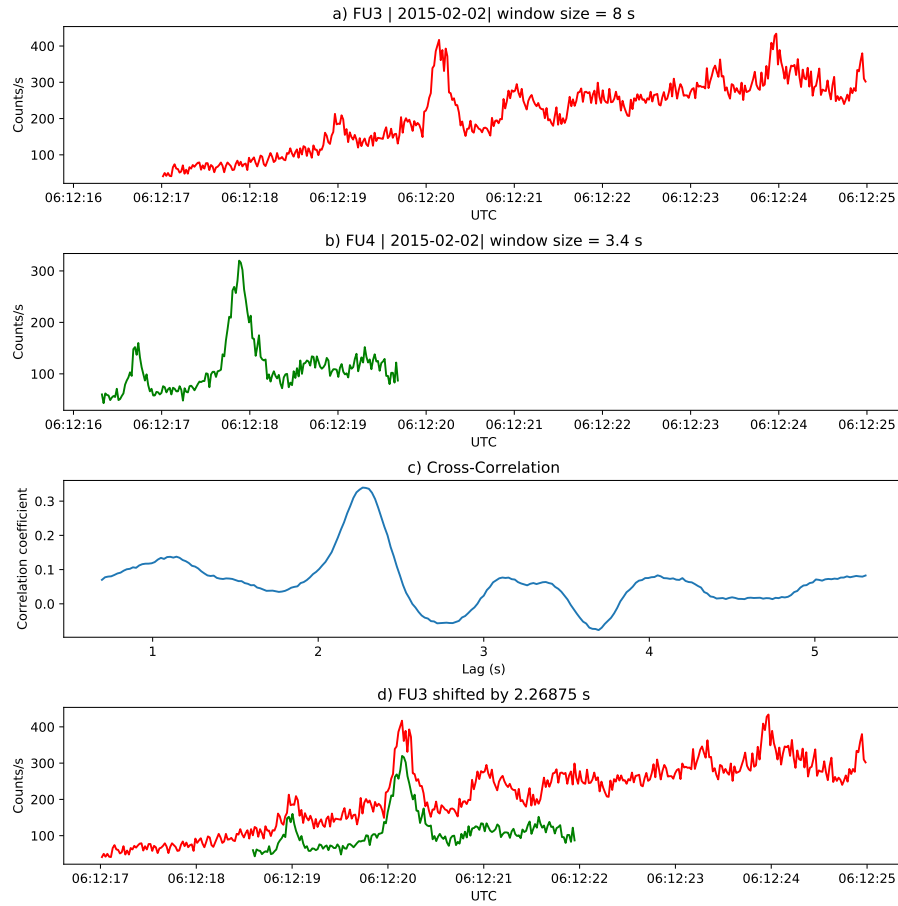


Figure B.4: Same analysis as Fig. B.1 on a different time period. Clock difference was 2.27 s.

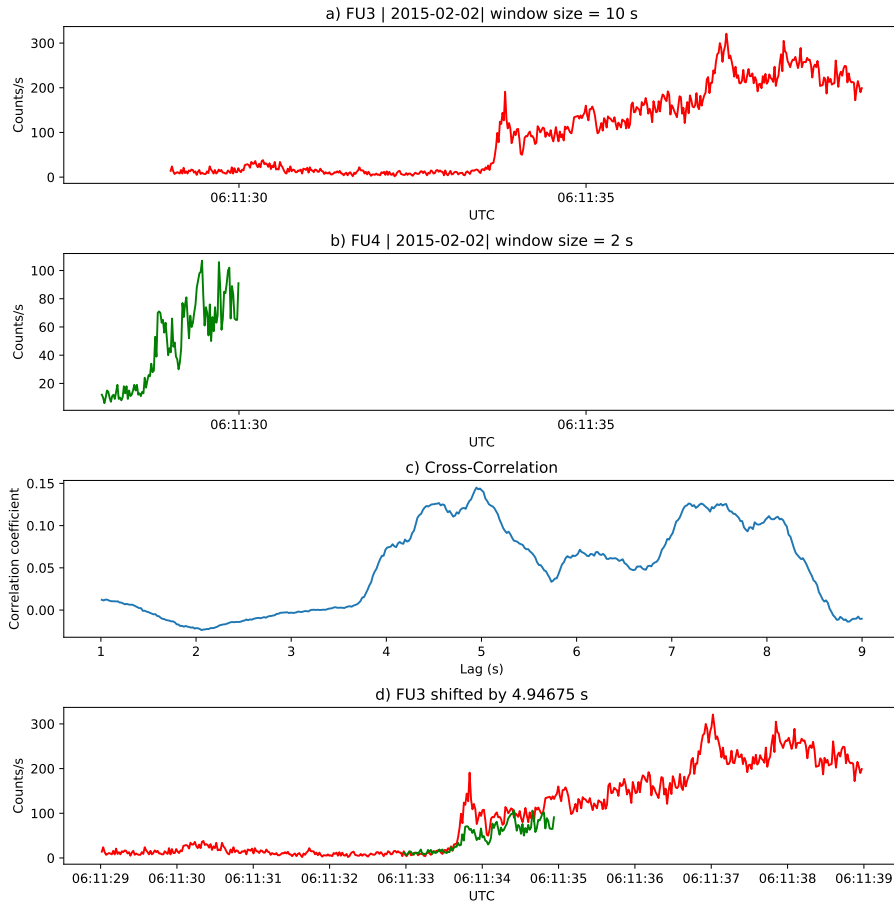


Figure B.5: Same cross-correlation time lag analysis applied to stationary spatial structures. The cross-correlation lag between these events is a sum of the clock difference and time lag due to the spacecraft separation. The lag derived at this time was 4.95 s.

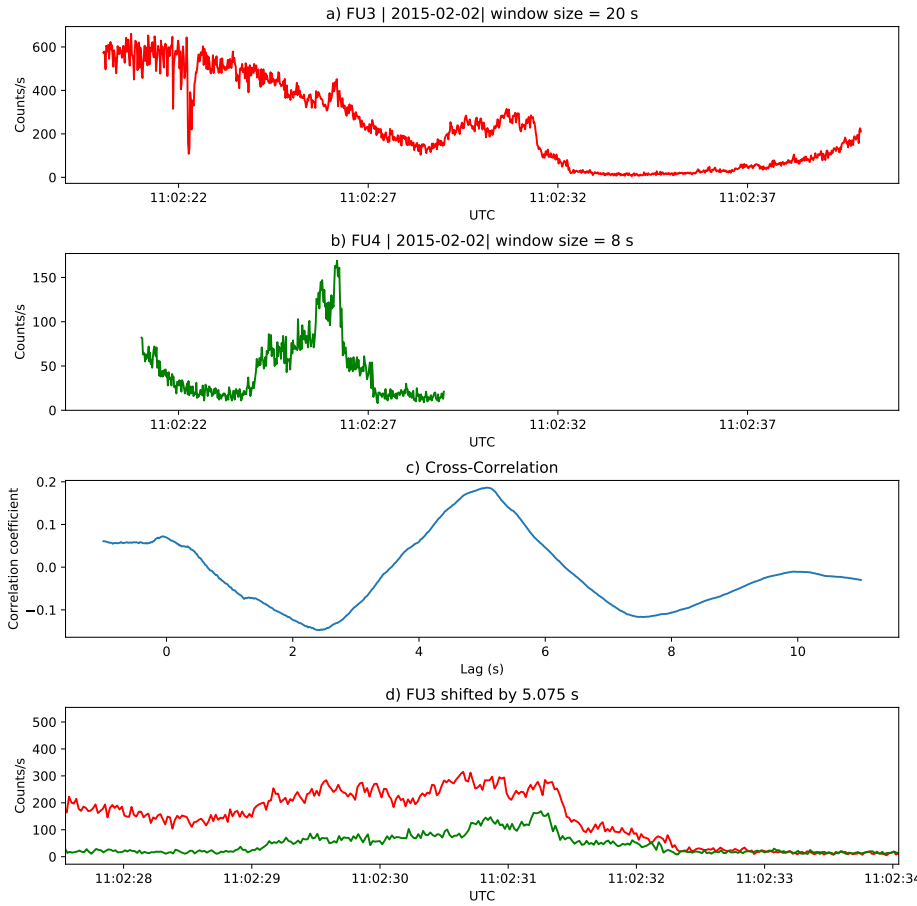


Figure B.6: Same analysis as Fig. B.5 applied to a different stationary spatial feature. The lag derived at this time was 5.01 s.

APPENDIX C

AC6 MICROBURST SIZE MODEL AND MICROBURST-WAVE COMPARISON

This appendix contains texts S1-S3. Text S1 derives the analytic model that transforms a prescribed microburst PDF into a  $\bar{F}$  curve as a function of AC6 separation,  $s$ . Text S2 expands on the two-sized microburst model results presented in Section 5.3 and the range of optimal model parameters assuming continuous microburst PDFs such as the log-normal, Weibull, and Maxwellian. Lastly, text S3 presents the percent of microbursts observed in each separation bin, as a function of separation and compares it to the observed scale size of chorus waves as a function of wave amplitude.

**Text S1: Analytic Derivation of  $\bar{F}(s)$**  Here we derive the integral form of  $\bar{F}(s)$  under the following assumptions:

1. microbursts are circular with radius  $r$
2. microbursts are randomly and uniformly distributed around AC6.

First recall the area  $A(r, s)$ , given in Eq. 4 in the main text and copied here for convenience

$$A(r, s) = 2r^2 \cos^{-1} \left( \frac{s}{2r} \right) - \frac{s}{2} \sqrt{4r^2 - s^2}. \quad (\text{C.1})$$

A circular microburst who's center lies in  $A(r, s)$  will be observed by both AC6 units and is counted in  $\bar{F}(s)$ . Now we derive the integral form of  $\bar{F}(s)$  that accounts for the different spacecraft separations and microburst sizes that are distributed by a hypothesized PDF  $p(r, \theta)$ .

First we will account for the effects of various spacecraft separation, assuming all microbursts are one size. For reference choose of radius,  $r_0$  and spacecraft separation,  $s_0$  such that  $A(r_0, s_0) > 0$  which implies that some number of microbursts,  $n_0$  will be simultaneously observed. Now, if for example the spacecraft separation (or microburst radius) is changed such that the area doubles, the second assumption implies that the number of microbursts observed during the same time interval must double as well. This can be expressed as

$$\frac{n_0}{A(r_0, s_0)} = \frac{n}{A(r, s)} \quad (\text{C.2})$$

and interpreted as the conservation of the microburst area density. By rewriting Eq. C.2 as

$$n(r, s) = \left( \frac{n_0}{A(r_0, s_0)} \right) A(r, s) \quad (\text{C.3})$$

it is more clear that the number of microbursts of size  $r$  observed at separation  $s$  is just  $A(r, s)$  scaled by the reference microburst area density. The cumulative number of microbursts observed above  $s$  is then

$$N(r, s) = \int_s^\infty n(r, s') ds' = \left( \frac{n_0}{A(r_0, s_0)} \right) \int_s^\infty A(r, s') ds'. \quad (\text{C.4})$$

Lastly,  $\bar{F}(s)$  for a single  $r$  is then

$$\bar{F}(s) = \frac{N(s)}{N(0)} = \frac{\int_s^\infty A(r, s') ds'}{\int_0^\infty A(r, s') ds'} \quad (\text{C.5})$$

To incorporate a continuous microburst PDF such as  $p(r) = p_1\delta(r - r_1) + p_2\delta(r - r_2) + \dots$  we sum up the weighted number of microbursts that each size contributes to

$N(s)$  i.e.

$$N(s) = \left( \frac{n_0}{A(r_0, s_0)} \right) \left( \int_s^\infty p_1 A(r_1, s') ds' + \int_s^\infty p_2 A(r_2, s') ds' + \dots \right) \quad (\text{C.6})$$

The last step is to convert the sum of Dirac Delta functions into a continuous PDF  $p(r)$  after which

$$N(s) = \left( \frac{n_0}{A(r_0, s_0)} \right) \int_s^\infty \int_0^\infty A(r, s') p(r) dr ds'. \quad (\text{C.7})$$

With these considerations,  $\bar{F}(s)$  is then given by

$$\bar{F}(s, \theta) = \frac{\int_s^\infty \int_0^\infty A(r, s') p(r, \theta) dr ds'}{\int_0^\infty \int_0^\infty A(r, s') p(r, \theta) dr ds'} \quad (\text{C.8})$$

**Text S2: Most probable parameter values for continuous microburst PDFs**

Besides the one and two-size microburst models described in the main text, continuous PDFs such as the log-normal, Weibull, and Maxwellian were fit and their optimal parameters presented here.

For the Maxwellian PDF, we assumed the following form

$$p(r|a) = \sqrt{\frac{2}{\pi}} \frac{r^2 e^{-r^2/(2a^2)}}{a^3}. \quad (\text{C.9})$$

The range of  $a$  consistent with the observed data was found to be between 0 and 35 km. Next, the log-normal distribution of the following form was used

$$p(r|\mu, \sigma) = \frac{1}{\sigma r \sqrt{2\pi}} e^{\left(-\left(\ln(r) - \ln(\mu)\right)^2 / (2\sigma^2)\right)} \quad (\text{C.10})$$

and the results are summarized in C.1. Lastly the Weibull distribution of the following form was tested

$$p(r|c, r_0, \lambda) = c \left( \frac{r - r_0}{\lambda} \right)^{c-1} \exp \left( - \left( \frac{r - r_0}{\lambda} \right)^c \right). \quad (\text{C.11})$$

for which the model parameters are summarized in Table C.2.

Table C.1: Range of log-normal model parameters consistent with the observed AC6  $\bar{F}(s)$

percentile (%)	$\mu$	$\sigma$
2.5	1.8	0
50	21.8	0.4
97.5	52.0	1.1

Table C.2: Range of Weibull model parameters consistent with the observed AC6  $\bar{F}(s)$

percentile (%)	$c$	$r_0$	$\lambda$
2.5	0.6	1.3	2.7
50	5.5	26.2	32
97.5	19.3	72.5	72.2

**Text S3: Comparison of microburst to whistler mode chorus  $\bar{F}(s)$**   
**TBD**